

Changes in ice flow regime due to proglacial lake formation in an alpine glacier

TSUTAKI Shun

Ph. D. Dissertation

Division of Earth System Science
Graduate School of Environmental Science
Hokkaido University

March 2011

Abstract

This thesis carries out field measurements of glacier flow velocity and subglacial water pressure with 100 m of spatial distribution and shows the change in ice flow regime caused by proglacial lake formation in an alpine glacier. Proglacial lakes are dammed by bedrock bump or debris. Alpine glaciers in the world have been retreating significantly under the influence of recent climate change. In some of these glaciers, new proglacial lakes have formed. If a lake forms at the glacier terminus, three processes occur and might accelerate the glacier retreat: (1) ice flow acceleration due to increase in subglacial water pressure; (2) thinning of ice due to the acceleration of ice flow at the terminus; (3) surface uplift and ice disintegration due to increase in subglacial water pressure and further glacier thinning. By revealing these three processes based on the field observation, it is possible to provide new insights into a evolution of the proglacial lake. However, only a few observational studies have been conducted to glacier flow change immediately after the lake formation over long periods with high spatial resolution. Thus, understanding the mechanisms and quantitative evaluation of such flow change are not sufficient.

Previous studies investigated that melt water activates basal sliding and have discussed the importance of the contribution of a subglacial drainage system for the glacier flow. Temporal and spatial changes in subglacial drainage system have been explained by the observations for subglacial water pressure by using hot water drilling technique and drilled borehole. It is expected that subglacial water pressure at the glacier terminus adjacent to proglacial lake is influenced by lake water. However, only a few measurement for distribution of subglacial water pressure with high spatial resolution have been conducted and we have little understanding of impact of lake water on basal sliding.

The objective of this study is to investigate the changes in ice flow regime at the glacier terminus due to proglacial lake formation. Field measurement were carried out in spatial resolutions of 100 m at Rhonegletscher in the Swiss Alps during the summer seasons of 2007–2009. At this glacier, two proglacial lakes have formed since late 1990s as a result of glacier retreat. The measurements and subsequent data analyses focus on the spatial distribution of horizontal flow velocity, surface vertical movement (uplift) and water level in borehole in each measurement year. A three-dimensional flow model is developed to reproduce observed flow fields and is used to interpret the influence of changes in basal lubrication due to proglacial

ABSTRACT

lake formation on ice flow regime.

Digital Elevation Models (DEMs) for surface and bed elevation were interpolated from GPS survey for glacier surface and borehole drilling. Ice thickness near the terminus is thinning in a rate of -3.44 m a^{-1} from 2008 to 2009. This thinning rate has increased in the 21st century.

Horizontal flow velocity at the glacier terminus increased twofold from 2006 to 2007. Water level in borehole was approximately equal to lake level and it approached 90% of ice thickness in the range of 200 m up-glacier from the terminus, suggesting that a subglacial drainage system in this region was well developed. It is suggested that high water pressure enhanced basal sliding and caused the acceleration of glacier flow. Acceleration of ice flow at the terminus changed the flow regime in the longitudinal direction from compressive to tensile. This change was responsible for a part of the glacier thinning.

A crevasse began to form along Lake A margin toward Lake B. At the south western area from the crevasse, huge surface uplift was observed. Subglacial water pressure exceeded to ice overburden pressure in the lake shore. This area coincided with the region where significant surface upward motion was observed. These observations suggest that if the glacier continues to thin, the entire part of the terminus may get afloat and disintegrate over the next few years.

The observed flow regime was reproduced by introducing pressure load of lake water and locally enhanced basal sliding at the lake shore. It was shown that basal sliding is accelerated significantly by reduction of effective pressure in the range of 200 m from the terminus.

This study revealed changes in ice flow regime before and after the proglacial lake formation from the field measurement with high spatial resolution and presents new insight for prediction of glacier evolution. Furthermore, the results of this study contributes for prediction of glacier lake evolution and for prevention of glacial disaster such as Glacier Lake Outburst Flood (GLOF).

Contents

Abstract	i
List of figures	vi
List of tables	vii
1 General introduction	1
1.1 Proglacial lake in an alpine glacier	1
1.2 Influence of lake formation on the glacier flow field	1
1.3 Hot water drilling	3
1.4 Objectives	4
2 Field measurements	5
2.1 Study site	5
2.2 Methods	10
2.2.1 A hot water drilling system	10
2.2.2 Borehole drilling and ice thickness	10
2.2.3 Ice flow speed	13
2.2.4 Lake level and subglacial water pressure	15
2.2.5 Surface elevation	17
2.2.6 Meteorological observation	17
3 Field data results	19
3.1 Surface and bed geometry	19
3.2 Time series of glacier motion and borehole water level	22
3.3 Glacier flow fields in 2008 and 2009	27
3.4 Borehole water level	30
3.5 Summary	30
4 Field data interpretations	33
4.1 Ice flow acceleration in the terminus	33
4.1.1 Changes in ice flow speed before and after the lake formation	33

CONTENTS

4.1.2	Mechanisms of flow acceleration	35
4.2	Dynamic thinning	36
4.3	Surface uplift	38
4.3.1	Uplift and crevasse formation in the terminus	38
4.3.2	Interpretations of the uplifts	42
4.4	Future evolution of Rhonegletscher	45
4.5	Summary	49
5	Numerical model of Rhonegletscher	51
5.1	Field equations	51
5.1.1	Stokes equations	51
5.1.2	Constitutive equations	52
5.2	Finite element mesh	53
5.3	Boundary conditions	56
5.3.1	Basal sliding	56
5.3.2	2D cross-section flow models	57
5.3.3	Lake water pressure	60
5.4	Sensitivity tests	62
5.4.1	Test 1	62
5.4.2	Test 2	65
5.5	Modeling experiments	67
5.5.1	Experiment A: Non or uniform sliding	67
5.5.2	Experiment B: Locally enhanced sliding	70
5.6	Summary	72
6	Conclusion	73
6.1	Field observation	73
6.2	Numerical modeling	74
6.3	Future prospects of the study	74
Bibliography		77
Appendix		84
A	Performance test of the hot water drilling system	85
A.1	Test setting	85
A.2	Performance test results	85
A.3	Ice block drilling	88
A.4	Borehole drilling in Rhonegletscher	89
Acknowledgements		90

List of figures

2.1	Map of the glacier and the measurement sites	6
2.2	Photographs showing the glacier terminus	7
2.3	Block diagram showing the configuration of the hot water drilling system	8
2.4	The instruments of the hot water drilling system	9
2.5	Locations of surface elevation measurements	11
2.6	The accuracy tests of GPS measurement	15
2.7	Schematic diagram showing stake motion	16
2.8	Schematic diagram of the field measurements	16
3.1	Surface and bed geometry	20
3.2	Differences in the bed elevation between 2009 and 2000	21
3.3	Changes in surface elevation from 2008 to 2009	22
3.4	Time series of data taken in 2007	23
3.5	Time series of data taken in 2008	25
3.6	Time series of data taken in 2009	26
3.7	Horizontal and vertical flow velocities in 2008 and 2009	29
3.8	Borehole water levels in 2008 and 2009	31
4.1	Horizontal flow velocity from 2000 to 2009	34
4.2	Effective pressure at boreholes in 2008 and 2009	35
4.3	Horizontal flow velocity and strain rate	37
4.4	Spatial distribution of horizontal strain rate in 2009	39
4.5	Vertical displacement, borehole water level and flotation level	40
4.6	Spatial distribution of effective pressure in 2008 and 2009	41
4.7	Photographs showing formation of a crevasse	42
4.8	Temporal variation of vertical displacement	43
4.9	Schematic diagrams of uplift mechanisms	44
4.10	Photographs showing disintegration of the terminus	46
4.11	Flow diagram of influence of proglacial lake formation on glacier retreat	47
5.1	Surface nodes used for finite element mesh generation	53

LIST OF FIGURES

5.2	Oblique view of the 3D finite element mesh of Rhonegletscher	55
5.3	A finite element mesh on the upper boundary	56
5.4	Scheme of simple shearing of one element	57
5.5	Plane view of the upper boundary of the model	58
5.6	Computation of flow velocities without basal sliding	59
5.7	Computation of flow velocities with basal sliding	59
5.8	Sketch of the model boundary against to the lake	60
5.9	Model boundaries on which lake water pressure was applied	61
5.10	Vector components of lake pressure load	61
5.11	Computed surface flow vectors without sliding in Test 1	63
5.12	Computed surface flow vectors with basal sliding in Test 1	64
5.13	Computed surface flow vectors with basal sliding in Test 2	66
5.14	Computed flow velocities without sliding	68
5.15	Computed flow velocities with uniform sliding	69
5.16	The best fit of computed velocity with uniform sliding	69
5.17	Defined sliding area	70
5.18	The computed flow vectors with locally enhanced basal sliding	71
A.1	Water jet temperature vs. time	86
A.2	Drilling nozzle and water jet in the ice block	88
A.3	Map of the borehole locations drilled in 2007	89
A.4	Drilling depth as a function of drilling time	91

List of tables

2.1	The locations and lengths of borehole	12
2.2	Dates of GPS measurement at Stake 1–20	14
3.1	Horizontal and vertical velocities	28
5.1	Summary of conducted sensitivity tests in Test 1	62
5.2	Summary of conducted modeling experiment A	67
A.1	Time required for drilling through ice blocks	88
A.2	Depth and mean drilling rate of the boreholes in 2007	90

Chapter 1

General introduction

1.1 Proglacial lake in an alpine glacier

Proglacial lakes are dammed by bedrock bumps pose a potential threat to communities in high mountain regions. These lakes form between the frontal margins of retreating glaciers and bedrock bumps or debris. A number of proglacial lakes formed and expanded during the 20th century as a result of glacier thinning linked to climate change in the world: New Zealand (e.g. Kirkbride and Warren, 1999; Purdie and Fitzharris, 1999; Quincey and Glasser, 2009), Alaska, USA (e.g. Motyka and others, 2002; Boyce and others, 2007), Patagonia (e.g. Warren and Aniya, 1999; Warren and others, 1995; 2001; Rott and others, 1998; Skvarca and others, 2002; 2003).

Funk and Röthlisberger (1989) simulated the retreat rate of the terminus of Unteraargletscher, Switzerland by numerical modelling. The results suggested that the glacier retreats rapidly as soon as a calving process began at the terminus. In Triftgletscher, Switzerland, the glacier has retreated significantly since 1990. The retreat rate increased after 2000 as a result of interaction with a newly formed proglacial lake (Müller, 2004). These studies suggested that lake formation increases the rate of glacier retreat. Similar phenomenon has been reported in Patagonia (e.g. Naruse and Skvarca, 2000; Raymond and others, 2005), Alaska, USA (e.g. Motyka and others, 2002) and New Zealand (e.g. Purdie and Fitzharris, 1999; Quincey and Glasser, 2009). Formation and expansion of proglacial lakes also pose a threat to human activity due to the possibility of flooding caused by large ice avalanches (e.g. Haeberli, 1983; Huggel and others, 2004; Salzmann and others, 2004).

1.2 Influence of lake formation on the glacier flow field

There are two mechanisms of glacier flow, internal ice deformation and basal motion. In a temperate glacier, basal motion takes a dominant role in intra-annual flow variations. Because basal flow velocity fluctuates as a result of the changes in the conditions at the

glacier bed such as, water pressure variations and evolution of the hydraulic drainage system. The relationship between subglacial water pressure and surface flow velocity is studied in several temperate glaciers. Iken and Bindschadler (1986) measured surface velocity with subglacial water pressure at Findelengletscher in Switzerland. They plotted surface flow velocities against subglacial water pressure, and found that the velocity increases as the pressure rises up. In their plot, surface velocity appears to have an asymptote at the water pressure equal to the ice overburden pressure. Jansson (1995) made similar measurements at Storglaciären in Sweden. Measurements at Varigated Glacier in Alaska by Kamb and Engelhardt (1987) were conducted on a surging glacier. These two studies also found surface flow velocity increases under high subglacial water pressure condition as measured in Findelengletscher. The effective pressure is often used instead of subglacial water pressure to discuss the relationship with surface velocity observed in temperate valley glaciers and ice sheets (e.g. Bindschadler, 1983; Sugiyama and Gudmundsson, 2004). The effective pressure is defined as $P_e = P_i - P_w$, where P_i and P_w are the ice overburden and subglacial water pressures, respectively. Formation of a proglacial lake is expected to result in a high water pressure condition and to enhance the basal motion at the glacier terminus. Investigations at fresh-water calving glaciers have shown a linear relationship between ice flow speed and lake water depth (e.g. Funk and Röthlisberger, 1989; Van der Veen, 2002).

Both acceleration of ice flow and calving cause to decrease in ice thickness at the terminus. In Tasman Glacier, Kirkbride and Warren (1999) observed acceleration and rapid thinning followed by an increase in the calving rate. Boyce and others (2007) calculated horizontal strain rates from surface velocities near the glacier terminus. Results showed extending flow field, and magnitude of dynamic thinning corresponded to thinning rates of about 4 cm^{-1} . Here, the term *dynamic thinning* is used to represent effect of ice thinning due to ice flow regime. Assuming that the subglacial water pressure is constant near a lake, the effective pressure decreases as the ice thins. Benn and others (2007) suggested that there are positive feedbacks between glacier thinning and flow acceleration on a lake calving glacier in a phase of retreat. An initial thinning resulting from increased surface melting will lead to flow acceleration and dynamic thinning. Change in ice flow dynamics will lead to further thinning, and so on. This feedback will trigger terminus retreat when increased calving losses outweigh the effects of flow acceleration.

Another important mechanism at the lake front is break-up of glacier terminus caused by the buoyancy force of lake water. It may occur when the subglacial water pressure exceeds the ice overburden pressure. Observation at Triftgletscher, Switzerland by Müller (2004) showed that glacier terminus disintegrated and retreated by approximately 200 m from August 2002 to August 2003 after proglacial lake forming in 2000. Sudden uplift and break-off events have been observed during an outburst flood events, which were caused by collapse of ice-dammed lake (e.g. Roberts and others, 2005; Walder and others, 2005, 2006; Sugiyama and others, 2008b; Riesen and others, 2011).

Field studies on flow speed at the terminus of lake-calving glaciers have been conducted in Patagonia (e.g. Rott and others, 1998; Warren and others, 2001; Skvarca and others, 2003), New Zealand (e.g. Kirkbride and Warren, 1999; Quincey and Glasser, 2009) and the Himalayas (Luckman and others, 2007; Bolch and others, 2008). However, to gain deeper insights into the mechanisms controlling the dynamics of lake-calving glaciers, it is important to carry out high-resolution measurements of surface flow speed and subglacial water pressure in the process of lake formation. The marginal lakes forming in Rhonegletscher, Switzerland provide such an opportunity. These lakes began forming when the glacier retreated behind a bump in the bedrock, and the ice has been thinning at an increasing rate ever since (Sugiyama and others, 2008a). Because the glacier is located near paved roadways, the retreat of the glacier and formation of the lake have drawn not only many glaciologist's but also many tourist's and considerable public attentions.

1.3 Hot water drilling

Subglacial and englacial measurements can provide a wealth of information on glacier sliding (e.g. Fischer and Clarke, 1997; Engelhardt and Kamb, 1998), basal sediments (e.g. Fischer and Clarke, 1994; Tulaczyk and others, 2001), subglacial hydraulic conditions (e.g. Engelhardt and Kamb, 1997; Iken and Truffer, 1997; Fudge and others, 2008), ice temperature (e.g. Lüthi and others, 2002) and internal deformations (e.g. Hooke and others, 1992; Harper and others, 2001). To drill a borehole for such measurements, it is preferable to employ a faster method than mechanical drilling, which is normally used for ice coring.

A hot water drilling system generally consists of water basin, high-pressure water pump, heater, hose and jet nozzle. The nozzle, supported by tripod and pulley, emits a jet of water heated on a glacier surface. Hot water drilling has been used for a wide variety of measurements, both within and underneath glaciers. The features of this method are as follows: (1) a much faster drilling speed than a mechanical drill with drilling rate of $50\text{--}100 \text{ m h}^{-1}$, (2) the ability to drill both temperate and cold ice (e.g. Humphrey and Echelmeyer, 1990), (3) relatively simple construction using commercially available devices, and (4) easy operation.

Hot water drilling systems have been developed and employed at mountain glaciers and ice sheets: South Cascade Glacier in the USA (Taylor, 1984; Fountain, 1994), Findelengletscher in Switzerland (Iken and Truffer, 1997), Storglaciären in Sweden (Hanson and others, 1998), Jakobshavns Isbræ in Greenland (Iken and others, 1993), Ice Stream B (Engelhardt and others, 1990), Amery Ice Shelf (Craven and others, 2004) and Dome C in Antarctica (Koci, 1984). No such system has ever been constructed in Japan, however.

1.4 Objectives

Rhonegletscher is a temperate valley glacier in Swiss Alps. The changes in the terminus position have been recorded in photographs and maps since the 18th century, from which a drastic retreat can be seen over the last 150 years (Sugiyama and others, 2008a). As a result of retreat, a proglacial lake has formed between the glacier terminus and bedrock bump. The lake formation draws glaciological interest because the ice calving process may accelerate glacier retreat as was observed at Triftgletscher, Switzerland (Müller, 2004).

The objective of this study is to investigate the impact of proglacial lake formation on ice flow regime. This objective is achieved by field measurements and numerical investigation.

In the observation part, intensive field measurements are carried out near the terminus of Rhonegletscher during the summer seasons of 2007–2009. Objectives of the measurements are to obtain observational data for investigating the following phenomena expected at the glacier terminus;

1. acceleration of glacier flow after the proglacial lake formation;
2. ice thinning due to extending flow regime (dynamic thinning);
3. surface uplift and terminus disintegration;

We have developed a hot water drilling system for englacial and subglacial measurements, which was able to drill up to 200-m thick temperate ice. The flow speed and vertical ice motion were measured with high spatial resolution in each year and compared with reported data taken before the lake formed. Surface and bed elevations in the region were measured by Global Positioning System (GPS) surveys and by drilling boreholes. The basal water pressure was measured to obtain spatial distribution of subglacial hydraulic condition.

In the modelling part, flow fields in a terminal part of the glacier are computed with a three-dimensional (3D) numerical flow model. The model is used to reproduce the flow fields with the basal motion and lake water pressure, which account for changes in recent flow field of the terminus. Then, the measured flow field variations are simulated with the model in order to test the hypothesis proposed for the field data.

Chapter 2

Field measurements

The first section of this chapter provides a brief introduction of Rhonegletscher, the field study site of this study. A summary of previously conducted important works related to Rhonegletscher is presented. In the second section, the methods of borehole drilling, ice flow velocity and subglacial water pressure measurements are explained.

2.1 Study site

The field measurements were carried out at Rhonegletscher, a temperate valley glacier in the Urner Alps, Switzerland (Fig. 2.1a). It is the source of the Rhone river. The glacier has a wide accumulation basin and a narrow tongue. The glacier is 7.85 km long with an area of 15.9 km² (Bauder and others, 2007; Turi, 2009). It originates at 3600 m a.s.l., and terminates at 2208 m a.s.l.. The orientation of both the accumulation and ablation areas is to the south. The mean equilibrium line altitude (ELA) lies at 3035 m a.s.l. in 1981–82 (Chen and Funk, 1990).

Rhonegletscher has drawn scientist's attention since the 19th century. The Swiss Glacier Commission conducted the first scientific field measurements on Rhonegletscher from 1874 (Carlen, 2005). In this study, a trigonometric marker net was set up to survey and draw of a complete map at 1:25,000 (Mercanton, 1916). Jost (1936) constructed a bedrock geometry map after seismic measurements of the ice thickness in 1931. Digital elevation models (DEMs) of glacier surface were obtained in a 25 m resolution mesh by digitizing maps constructed for the periods 1874–82 and 1928–30. These studies were carried out by Mercanton (1916) and Jost (1936). DEMs were also obtained by maps constructed by photogrammetric analyses of aerial photographs taken in 1959, 1980, 1991 and 2000 (Zahno, 2004; Bauder and others, 2007). Zahno (2004) measured the ice thickness along 12 transverse profiles by radar echo soundings and constructed a bed elevation map by interpolation. In the region 500–800 m from the current terminus, Sugiyama and others (2008a) founded that the ice thickness obtained by borehole drilling in 2007 was up to 100 m thinner than the thickness reported

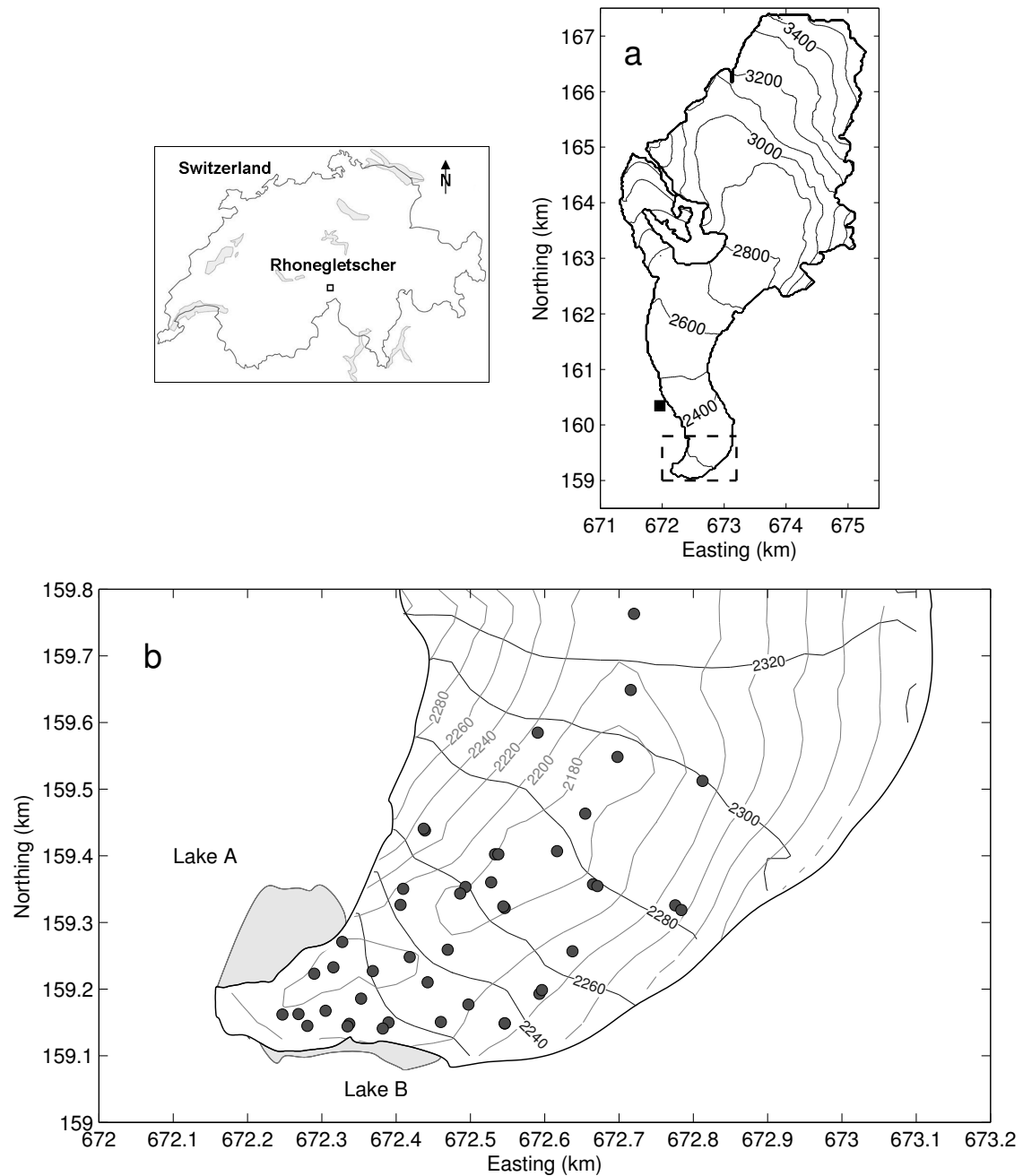


Figure 2.1: (a) Map of Rhonegletscher with surface elevation. The surface elevations are based on DEMs constructed from a photograph in 2000. The black square is the location of the meteorological station. (b) The study area indicated by the box in (a). The black and grey contours indicate surface in 2009 and bedrock elevations with intervals of 20 m, respectively. These contours were obtained by GPS survey and borehole drilling conducted in this study. The circles are locations of boreholes drilled in 2007–09. The two proglacial lakes are indicated by the shaded areas. The coordinates correspond to the official Swiss coordinate system.

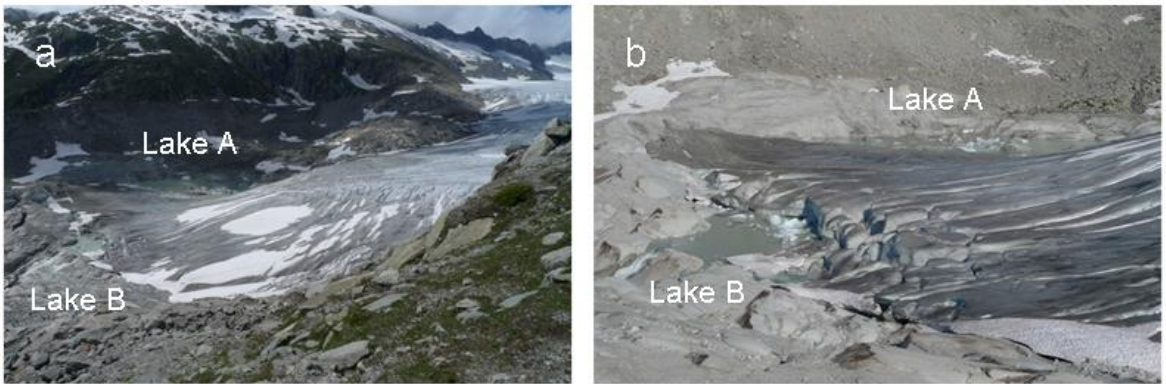


Figure 2.2: Photographs showing (a) the study area and (b) the proglacial lakes viewed from the southeast. The photographs were taken on (a) 6 July 2009 and (b) 16 July 2009.

by Zahno (2004). Sugiyama and others (2008a) also indicated that the bedrock depression exists at about 500 m from the terminus, and the lake depth along the valley centre will reach approximately 50 m.

Rhonegletscher is one of the glaciers with the longest record of terminus fluctuations in the world (Chen and Funk, 1990). The glacier terminus retreated 1700 m from 1878 to 2000 (Sugiyama and others, 2011). The annual mass balance was measured for the periods of 1874–75 and 1885–1910 (Mercanton, 1916). According to these measurements, the volume of the glacier ice reduced by $1.1 \times 10^8 \text{ m}^3$ between the years 1882 and 1912. The spatial distribution of mass balance was examined in more detail by Funk (1985) and Chen and Funk (1990), who investigated mass balance changes during the periods of 1882–83 and 1986–87 by in-situ measurements. Bauder and others (2007) measured the mass balance for the period of 1874–2000 by comparing six DEMs. Huss and others (2008) reconstructed seasonal mass balance for the period of 1865–2007 for four Swiss glaciers, including Rhonegletscher. The cumulative mean specific net balance over the years 1865–2006 is about -43 m w.e.a^{-1} .

The dynamics of Rhonegletscher has been measured since 19th century as well as mass balance measurements. The first measurement of surface flow speed has been carried out by tracking stones distributed on the glacier during the period 1874–1915 (Mercanton, 1916). The flow speed fluctuated little from year to year. The velocity was 230 m a^{-1} in the ice fall located downglacier from the bedrock bump. Nishimura (2008) reanalyzed the map showing the displacement of the stones and calculated the surface flow velocity distribution. Nishimura (2008) also calculated the surface flow fields for the periods 1970–71, 1881–82, 1999–2000 and 2005–06 by analyzing aerial photographs. Decreases in surface flow velocity has accelerated since 1970 over the range of 3.5 km from the current terminus. Turi (2009) made surface flow velocity and vertical displacement measurements by surveying stakes with a theodolite

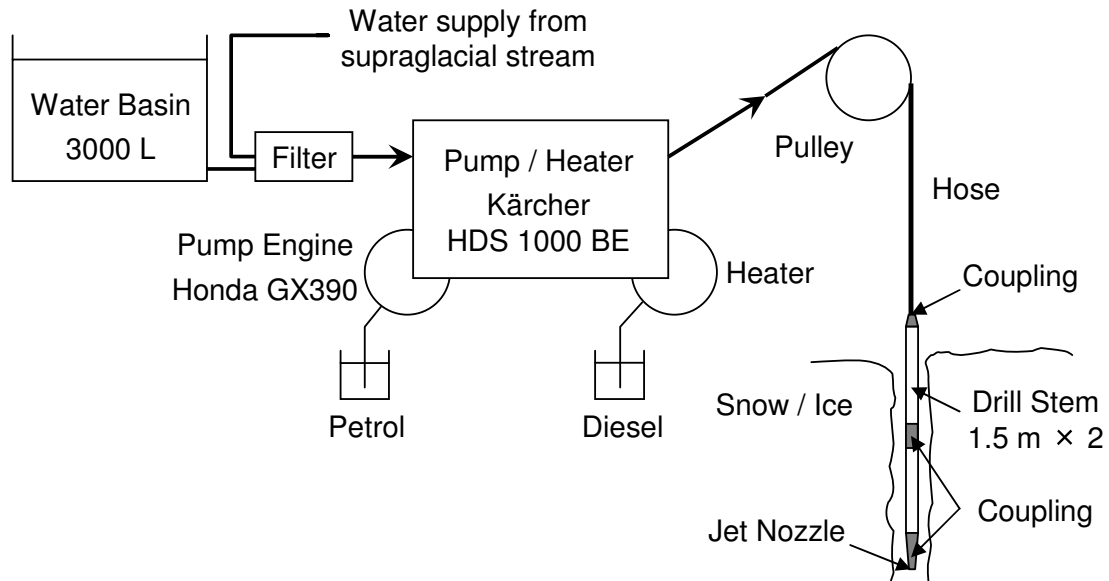


Figure 2.3: Block diagram showing the configuration of the hot water drilling system constructed for this study.

in the summer seasons of 2007 and 2008. A decreasing mean surface flow velocity from the upglacier to the terminus can be noticed over the range of 3.0 km from the current terminus, attributed to the compressive flow regime in the ablation area.

Flowline models are commonly used to simulate the evolution of valley glaciers. One dimensional flow line models have been applied to Rhonegletscher to simulate historical front variations (Stroeven and others, 1989; Sugiyama and others, 2007). Flow line model also has been applied to this glacier to study the sensitivity to climate change (Wallinga and Van de Wal, 1998). Jouvet and others (2009) performed three dimensional numerical simulation of the temporal and spatial changes of the glacier evolution over the period 1874–2007.

One of the recently formed proglacial lakes, referred to as Lake A in this paper, has existed since the late 1990s. It is located at the northwestern margin of the glacier (Figs 2.1b and 2.2). The other lake appeared in 2005 (Lake B) by ponding melt water in the depression between the glacier front and the bedrock bump (Figs 2.1b and 2.2). The surface water level of Lake B is nearly constant because excess water spills over the rock ridge. As shown in Figure 2.2b, ice blocks broke into Lake B during the summer seasons of 2007–2009. All of our field activities were carried out in a region within 800 m from the glacier terminus, in the summer seasons of 2007–2009 (Fig 2.1b).

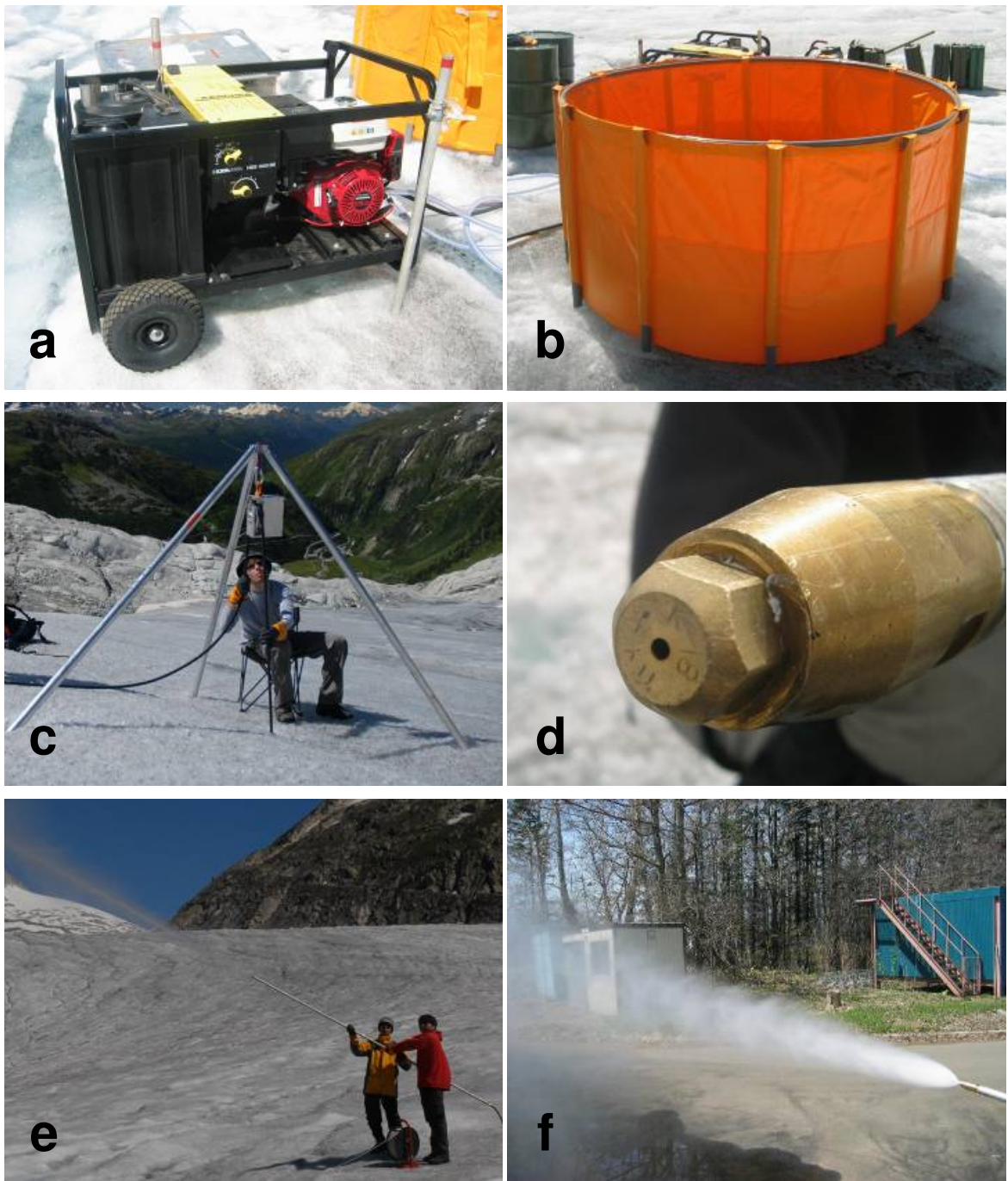


Figure 2.4: The instruments of the hot water drilling system. (a) The high-pressure hot water machine (Kärcher HDS1000BE), (b) the 3000 l water basin, (c) the tripod with its pulley, (d) a jet nozzle mounted at the tip of the drilling stem, (e) a water jet from a 3 m long drilling stem with a straight nozzle, and (f) a water jet from the conic spray nozzle.

2.2 Methods

2.2.1 A hot water drilling system

The configuration of the drilling system used for this study is shown in Figure 2.3. Hot water is generated by a commercially available high-pressure hot water machine, Kärcher HDS1000BE (Fig. 2.4a), which is commonly used for cleaning vehicles and buildings. The same device has been used by a British research team for drilling mountain glaciers (Hubbard and Glasser, 2005). A petrol-driven water pump engine (Honda GX390) and diesel combustion heater are combined to achieve flow rates in a range of 450–900 l h⁻¹, pressures of 6–21 MPa, and temperatures of 30–140°C when they are used with a cleaning nozzle which is specially designed to change the flow rate for a cleaning purpose. The total weight of the machine is 165 kg. A safety device is installed between the pump and the heater, which turns off the heater when the water pressure drops below an operating threshold. The pump draws water from a 3000 l basin with a diameter of 2 m and a weight of 28 kg (National Marine Plastic Inc. Type E) (Fig. 2.4b). On site, it can also draw water from supraglacial streams and ponds. The drilling hoses, which individually are 50–100 m long and have an internal diameter of 8 mm, are connected with couplings to obtain enough length. During drilling, the hose is supported by a pulley hung on a tripod (Fig. 2.4c). The pulley is designed to measure the length of hose by counting rotations. An aluminum made tripod has a length of 2.2 m and a weight of 10 kg, and can be disassembled for transportation. The nozzle with 1.6, 2.0 and 2.5 mm diameters (Katorigumi Seisakusho Inc. Type K-18) produce a narrow and straight jet (Fig. 2.4d). Two 1.5 m long stainless steel pipes with internal and external diameters of 19.6 and 27.2 mm were connected with a brass coupling (Fig. 2.4e). Two pieces of pipes were used in order to have enough length and weight to drill a straight borehole. This drilling stem was constructed at the workshop of the Institute of Low Temperature Science, Hokkaido University. A conic spray nozzle (Type K-20) is used to enlarge the diameter of a borehole after drilling (Fig. 2.4f). The total weight of all equipment (hot water machine, water basin, tripod, pulley and drilling stem) is approximately 220 kg, plus 30 kg per 100 m of hose.

2.2.2 Borehole drilling and ice thickness

In the summer seasons of 2007–2009, 51 boreholes were drilled to the glacier bed within the region 800 m from the terminus (Fig. 2.1b). The pump and heater were always located near GPS1, and the hose was extended to each drilling site (Tsutaki and Sugiyama, 2009). Before drilling, required length of hose was piled up and insulated from ice surface with cotton cloth and wooden poles. The hose extended to the drilling site would melt a groove into the ice during operation, increasing its contact with the ice surface. To minimize heat loss, the hose was often taken out of this groove. We normally pumped water into the hot water machine directly from a supraglacial stream. The basin was used only when the amount of running

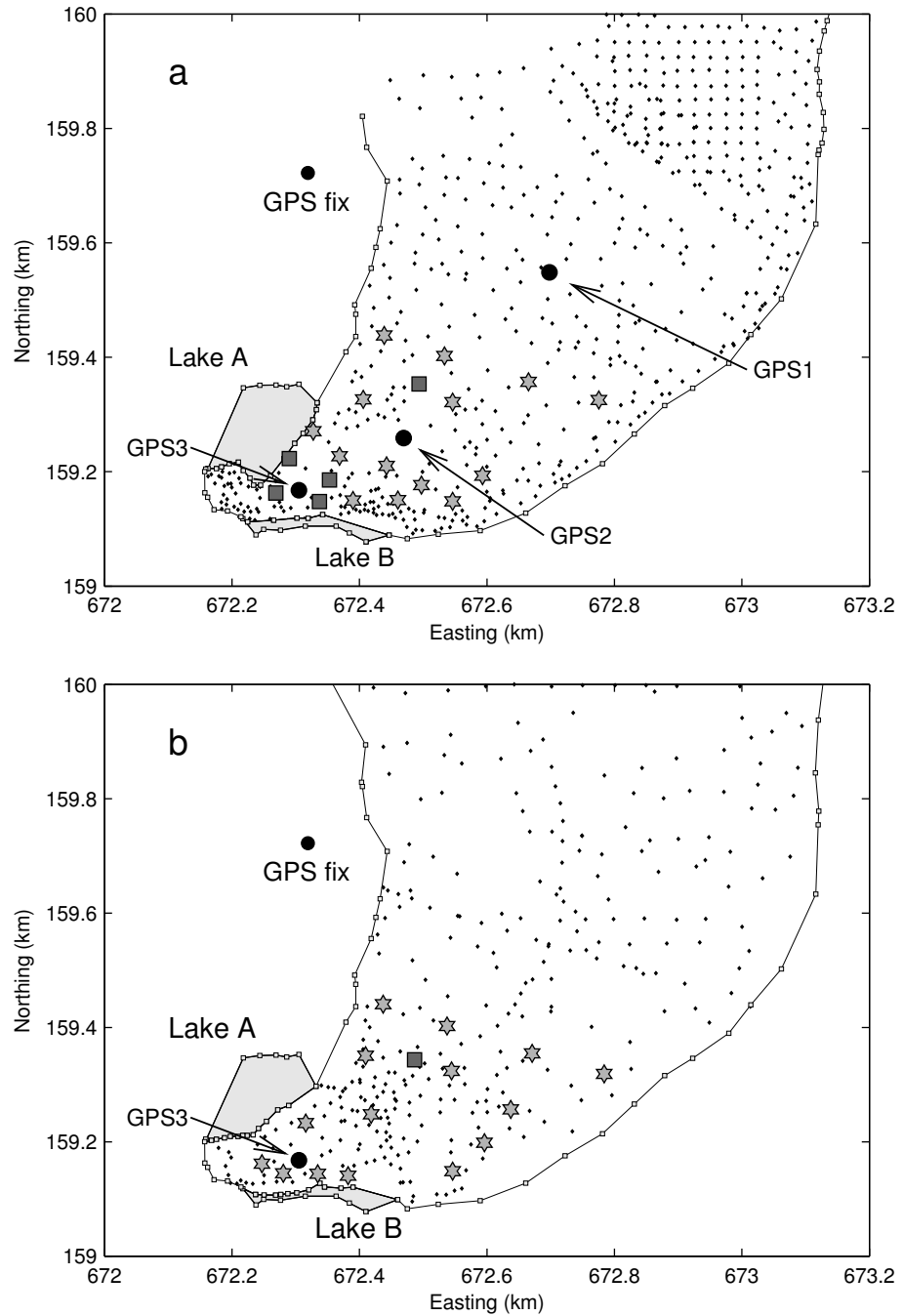


Figure 2.5: Locations of surface elevation, flow speed and water level in borehole measurements in (a) 2008 and (b) 2009. The diamonds and white squares are locations of surface elevation and margin survey. The black circles indicate the locations of continuous measurements of surface flow and water pressure measurements. The hexagrams indicate surface flow and borehole water level measurements with 10–14 day intervals. The shaded squares are the locations of borehole.

Table 2.1: *The location and length of borehole drilled in 2007–09.*

Borehole No.	Date	Easting m	Northing m	Surface elevation m	Length m	measurement
BH701	13 Jul. 2007	672698.03	159548.24	2304.63	138.0	Pressure, GPS1
BH702	14 Jul. 2007	672654.68	159463.21	2294.86	120.0	
BH703	15 Jul. 2007	672616.75	159407.00	2287.72	119.0	
BH704	16 Jul. 2007	672715.89	159648.79	2319.45	124.0	
BH705	17 Jul. 2007	672812.51	159512.29	2309.42	99.0	
BH706	17 Jul. 2007	672590.60	159584.72	2302.64	87.0	
BH707	18 Jul. 2007	672720.24	159762.90	2339.46	135.0	
BH708	17 Jul. 2007	672527.93	159360.07	2275.77	103.0	
BH801	18 Jul. 2008	672533.28	159402.19	2272.54	91.0	Stake 2
BH802	18 Jul. 2008	672306.25	159168.95	2215.26	21.9	
BH803	18 Jul. 2008	672305.15	159167.50	2215.22	18.7	Pressure, GPS3
BH804	19 Jul. 2008	672307.60	159168.53	2215.50	21.9	
BH805	19 Jul. 2008	672308.65	159166.60	2215.73	18.0	
BH806	20 Jul. 2008	672268.66	159162.57	2214.25	33.7	
BH807	20 Jul. 2008	672289.87	159223.04	2213.33	35.0	
BH808	20 Jul. 2008	672368.68	159226.98	2226.22	47.5	Stake 10
BH809	21 Jul. 2008	672327.49	159270.63	2214.04	35.5	Stake 8
BH810	21 Jul. 2008	672352.95	159185.67	2221.07	34.9	
BH811	21 Jul. 2008	672337.08	159147.73	2217.97	27.7	
BH812	21 Jul. 2008	672469.42	159258.93	2251.39	67.5	Pressure, GPS2
BH813	23 Jul. 2008	672593.02	159192.85	2255.75	38.5	Stake 14
BH814	23 Jul. 2008	672497.34	159176.66	2234.42	35.4	Stake 13
BH815	23 Jul. 2008	672460.29	159150.52	2227.27	39.4	Stake 19
BH816	23 Jul. 2008	672442.49	159210.14	2236.78	53.9	Stake 12
BH817	24 Jul. 2008	672389.90	159149.81	2223.28	38.4	Stake 18
BH818	24 Jul. 2008	672546.23	159148.21	2237.50	25.3	Stake 20
BH819	24 Jul. 2008	672665.12	159357.16	2283.89	99.3	Stake 3
BH820	25 Jul. 2008	672775.72	159325.47	2288.87	59.0	Stake 4
BH821	25 Jul. 2008	672438.80	159438.06	2273.54	40.7	Stake 1
BH822	25 Jul. 2008	672406.07	159326.33	2250.69	55.8	Stake 5
BH823	25 Jul. 2008	672493.43	159353.17	2265.62	84.8	
BH824	26 Jul. 2008	672546.16	159321.58	2270.48	92.4	Stake 6
BH901	29 Jun. 2009	672537.54	159402.25	2267.48	91.5	Stake 2
BH902	29 Jun. 2009	672437.17	159440.59	2268.04	34.0	Stake 1
BH903	29 Jun. 2009	672409.58	159350.35	2249.11	51.8	Stake 5
BH904	29 Jun. 2009	672486.35	159343.39	2258.08	86.7	Pressure
BH905	29 Jun. 2009	672544.44	159323.92	2265.10	86.8	Stake 6
BH906	29 Jun. 2009	672670.87	159354.55	2279.26	92.1	Stake 3
BH907	29 Jun. 2009	672783.90	159318.59	2283.53	49.2	Stake 4
BH908	30 Jun. 2009	672637.39	159256.58	2266.30	53.0	Stake 8
BH909	30 Jun. 2009	672596.26	159198.48	2252.67	36.0	Stake 14
BH910	30 Jun. 2009	672546.22	159148.67	2233.13	22.7	Stake 20
BH911	30 Jun. 2009	672382.06	159140.78	2218.25	35.6	Stake 18
BH912	30 Jun. 2009	672311.34	159171.16	2211.94	39.0	Pressure, GPS3
BH913	30 Jun. 2009	672334.68	159144.06	2213.75	30.0	Stake 17
BH914	30 Jun. 2009	672315.61	159232.67	2211.07	33.0	Stake 9
BH915	30 Jun. 2009	672247.12	159161.87	2211.04	27.3	Stake 15
BH916	30 Jun. 2009	672280.69	159144.72	2211.03	20.0	Stake 16
BH917	30 Jun. 2009	672418.37	159248.08	2235.76	55.2	Stake 11

water was not sufficient for drilling. At times the heater would automatically shut down due to the accumulation of black sediment from the glacier in a filter installed at the water intake (Fig. 2.3). The drilling was carried out using either the 2.0 or 2.5 mm jet nozzle. For some boreholes, the 2.0 mm conic spray nozzle was also used to enlarge the borehole. The length of the hose in a borehole was recorded during drilling every 5–15 minutes to measure the drilling speed. During the drilling, operator kept the nozzle slightly above the borehole bottom to drill a straight borehole. Drilling continued until the nozzle reached the glacier bed, a moment which could be recognized by the change in hose tension. The borehole depth was determined by the length of the hose used for drilling. Borehole drilling in 2007 and 2008 were conducted with our hot water drilling system. In 2009, we loaned similar type of hot water drilling system by Section of Glaciology, VAW, ETH Zurich.

The accuracy of the thickness is 1–2 m because of stretching of the hose during the drilling. The ice thickness was also measured with a measuring tape lowered into some of the boreholes with a weight on its end. The accuracy of this measurement is 20 mm. Bedrock elevation was calculated from the ice thickness and the surface elevation measured by the kinematic GPS survey. We constructed a bedrock elevation map with 25 m resolution by interpolating the bed elevations obtained at the drilling sites (Fig. 2.1b).

2.2.3 Ice flow speed

We measured the surface motion of the glacier by surveying 23 stakes (aluminum poles 4.0–6.0 m long) installed in the ice at the locations indicated in Figure 2.5a and b. These stakes were named as Stake 1–20 and GPS1–3 (Table 2.1). We used dual-frequency GPS receivers and antennae (Leica System 1200) to measure the three-dimensional (3-D) positions of the stakes. One antenna was fixed to solid rock on the western bank of the glacier as a reference station (Fig. 2.5). Another antenna was mounted on the stakes and operated for 1 hour with 3 hour intervals at GPS1–3 and for 20–30 minutes every 10–14 days at Stake 1–20. These data were processed in a static mode by GPS software (Leica Geo Office) to compute the 3-D position of each stake. The displacement of a stake divided by the elapsed time of the two measurements gives the ice flow velocity. The GPS measurements at GPS1–3 were conducted from 14 July to 6 September in 2007, from 18 July to 7 September in 2008 and from 27 June to 6 September in 2009. The measurements at Stake 1–20 were carried out in some periods as listed in Table 2.2.

The distance between the rover and reference receivers was 208–634 m in the horizontal and 2–122 m in the vertical direction, and this relatively short distance was crucial to obtain the necessary accuracy of the GPS measurement. The accuracy was evaluated after the field season by using the same survey method with two fixed receivers standing apart 82 m horizontally and 12 m vertically. Continuous test measurements for 6 days gave standard deviations of 1.6 mm and 4.1 mm in horizontal and vertical directions, respectively (Fig. 2.6a).

Measurement errors due to the tilting of the stake by ice melt or wind are about 10–20 mm. This error is less than 3% of the total stake displacement over each survey interval in the three seasons.

Surface flow velocity at GPS1–3 was calculated every three hours in horizontal direction by smoothing the horizontal displacement of the stake using *Gaussian smoothing* routine with a bandwidth of 4 hours. The data gaps due to the interruption of continuous survey were removed from the data set.

For the correct measurement of the vertical velocity component, it was important to fix the stakes into the ice during the measurements. Our measurements provide the displacement of a particle of ice near the glacier surface. Surface ablation does not influence on measured vertical displacement in this study because the displacement means the movement of such particles in this study (Sugiyama and Gudmundsson, 2004). Figure 2.7 shows the components of measured flow velocity in the ablation area of the glacier. Here, the x -axis has been taken as horizontal and positive in the downglacier direction. The z -axis has been taken as positive upward. The horizontal component of the flow velocity u over a time period from t_0 to t_1 arises with the glacier surface slope α because the stake has moved downslope. The measured surface elevation change w can be described as:

$$w = -ut \tan \alpha + w^*, \quad (2.1)$$

where the quantity w^* is the vertical component of flow velocities. In the ablation area, w^* is positive. Owing to the relative magnitude of the two terms on the right-hand side of the equation (see Fig. 2.7), the right-hand side is negative. The right-hand side is so-called the *emergence velocity* (Hooke, 2005). In the ablation area, the emergence velocity indicates the upward of ice relative to the glacier surface at a point fixed in space. In this study, the vertical velocity w^* is calculated and described in Section 3.3.3.

Table 2.2: Dates of differential GPS measurement at Stake 1–20.

Measurement	Date 2008	Date 2009
1	24 Jul. – 1 Aug.	26–29 Jun.
2	3–9 Aug.	3 Jul.
3	26–30 Aug.	16 Jul.
4	5–6 Sep.	6 Aug.
5		11–12 Aug.
6		19 Aug.
7		30–31 Aug.
8		5 Sep.

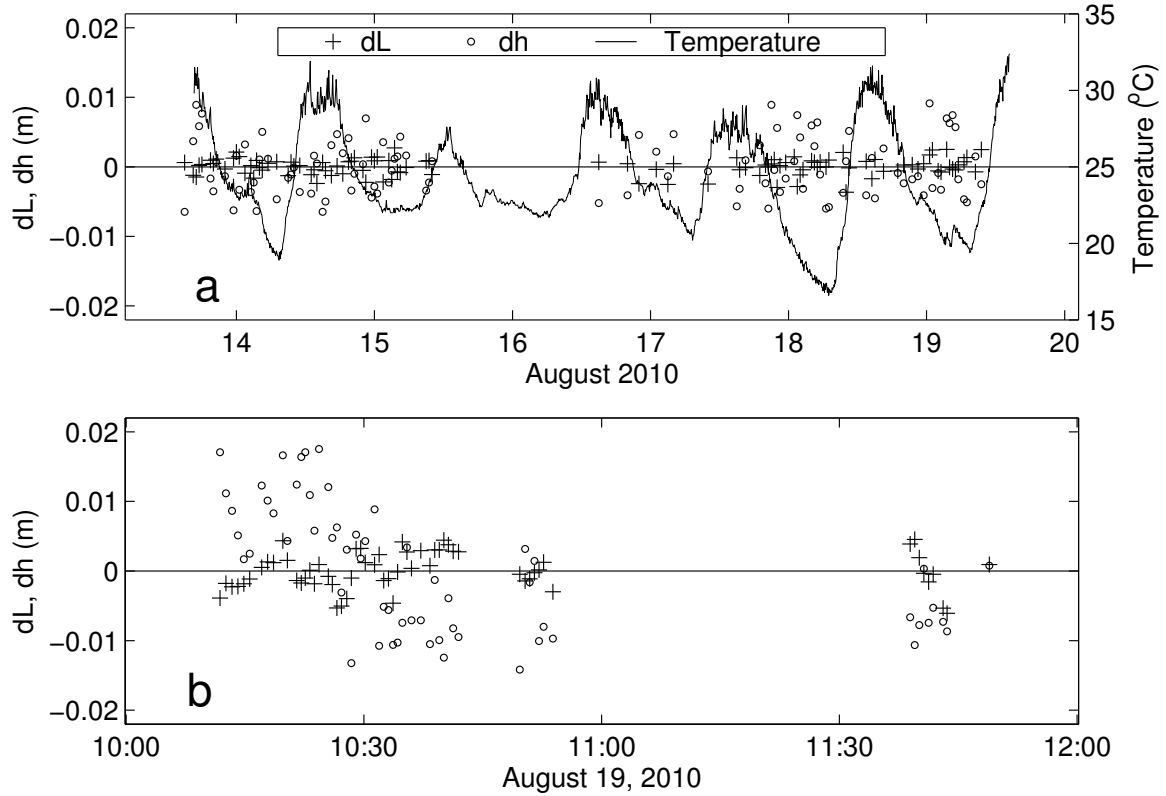


Figure 2.6: The accuracy tests of GPS measurement with (a) static and (b) kinematic mode.

2.2.4 Lake level and subglacial water pressure

The surface elevation of the two proglacial lakes was measured by using the some GPS static survey as described in Section 2.2.2. As depicted in Figure 2.8, the antenna was fixed at the lake shore. The measurements were taken on 29 August 2008 and 2 September 2009.

Vibrating-wire pressure sensors (Geokon Model 4500) were installed at the bottom of boreholes at GPS1 from 14 July 2007 to 6 September 2009, at GPS2 from 22 July to 7 September 2008 and at GPS3 from 18 July 2008 to 5 September 2009 to measure the subglacial water pressure (Figs. 2.5 and 2.8). The pressure was recorded every 10 minutes using a data logger (Campbell Scientific CR-1000). The measured subglacial water pressure was converted to water levels in boreholes. The accuracy of the pressure measurement was equivalent to a water level of 0.2 m. In other boreholes, which were not equipped with the sensor, we measured water levels with a measuring tape equipped with a float sensor (Figs 2.5 and 2.8). The measurement was conducted every 10–14 days with an accuracy of 0.1 m.

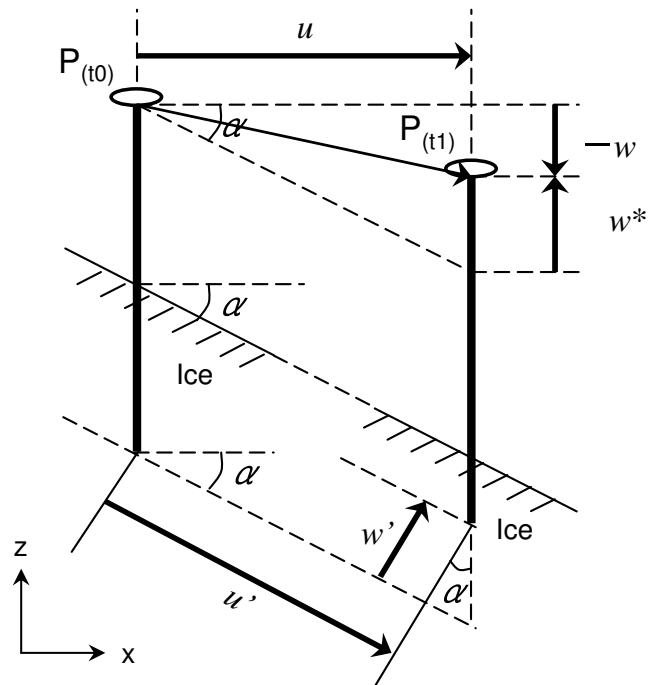


Figure 2.7: Schematic diagram showing stake motion over a time period from t_0 to t_1 . $P_{(t_0)}$ and $P_{(t_1)}$ represent the positions of the stake at times t_0 and t_1 . The horizontal component of the surface flow velocity is u and u' . The measured surface elevation change is w . The vertical component of flow velocity is w^* and w' .

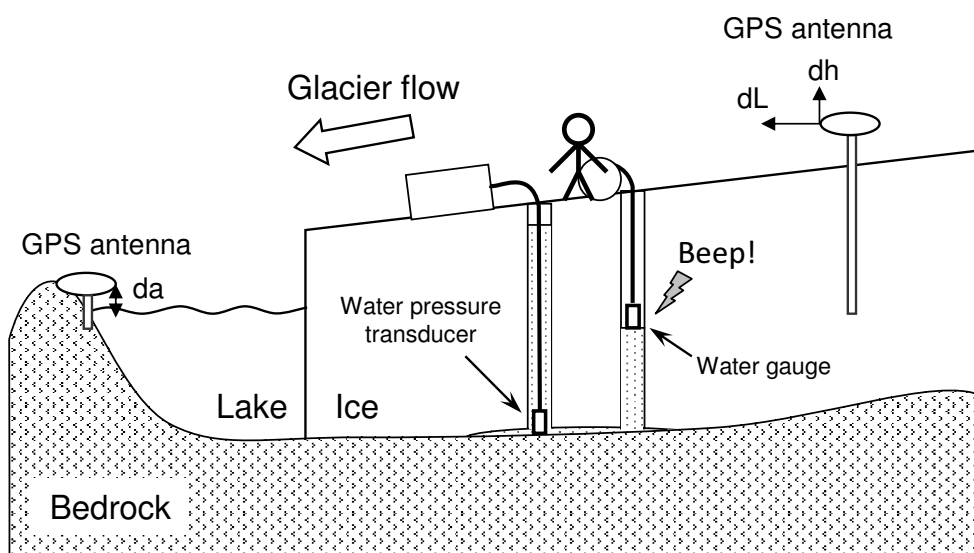


Figure 2.8: Schematic diagram of the field measurements.

2.2.5 Surface elevation

The glacier surface elevation was surveyed on 27 and 31 July 2008 and on 12 and 29 July 2009. We used the same GPS devices, this time operating in kinematic mode, to measure at more than 200 locations in the study area (Fig. 2.5a and b). According to accuracy tests for 1.5 hours by using the same measurement settings described in previous paragraph, the standard deviations were 3.3 mm in the horizontal and 9.1 mm in the vertical directions, respectively (Fig. 2.6b). Errors due to the ice surface roughness are about 100 mm. We used the same technique to survey the glacier and lake margins on 26 July, 27 July and 7 August in 2008, and on 12 July and 29 July in 2009.

2.2.6 Meteorological observation

A meteorological station was established on the western side of the glacier at an altitude of 2531 m a.s.l (Fig. 2.1a). Air temperature and precipitation were measured at intervals of 5 minutes from 14 July to 7 September 2007, 17 July to 7 September 2008 and 28 June to 6 September 2009. A multi-weather sensor (Vaisala WXT510) was used for the air temperature and precipitation measurements. Data gaps occurred because of the failure of power supply (battery drain), software problems (unknown reasons) and breakage of the sensor (thunderbolt).

Chapter 3

Field data results

In this chapter, results of the field measurements carried out in the summer seasons of 2007–2009 are presented. The presented data include (1) glacier surface and bedrock geometry obtained from GPS survey and borehole drilling, (2) temporal change in surface vertical movement, horizontal flow velocity, borehole water level, air temperature and precipitation, (3) spatial distributions of horizontal and vertical velocities, and water level in borehole.

3.1 Surface and bed geometry

The length of the boreholes drilled in 2007–2009 are listed in Table 2.1. The total drilling depths in 2007, 2008 and 2009 were 925 m, 1118 m and 1042 m, respectively. Figure 3.1a and b show the oblique perspective figure of Digital Elevation Models (DEMs) for glacier surface and bed geometry for 2009, respectively. From these DEMs, surface and bed elevation contour lines were drawn as Figure 2.1b. Surface elevation in the study region ranged from 2208 to 2336 m a.s.l., and the bedrock geometry in the upper part of the study region shows a parabolic curve. In figure 2.1b, the maximum ice thickness in the region was about 130 m near GPS1. A depression in the bedrock 30–40 m deep exists at 400–700 m from the terminus beneath GPS1 and GPS2. In regions where the surface elevation is below 2250 m, the ice thickness is less than 70 m. The glacier margins bordering Lake A and Lake B were about 26 m and 14 m thick, respectively.

Figure 3.2 shows the difference in bedrock elevation obtained in this study from that reported by the ice radar survey in 2003 (Zahno, 2004). The bed elevation was 2188 m a.s.l. at GPS3, which was 37 m lower than that calculated from the bedrock map in 2003. The discrepancy decreases upglacier and they agree with each other within 10 m near GPS2. In contrast, at GPS1, the bed elevation from this study was 2167 m a.s.l., which was 27 m higher than that from the ice radar data. Accordingly, the ice radar data underestimate the bed elevation in the upper reaches and overestimate in the current glacier tongue area. In previous study, Sugiyama and others (2008) also pointed out the underestimation of the bed elevation in

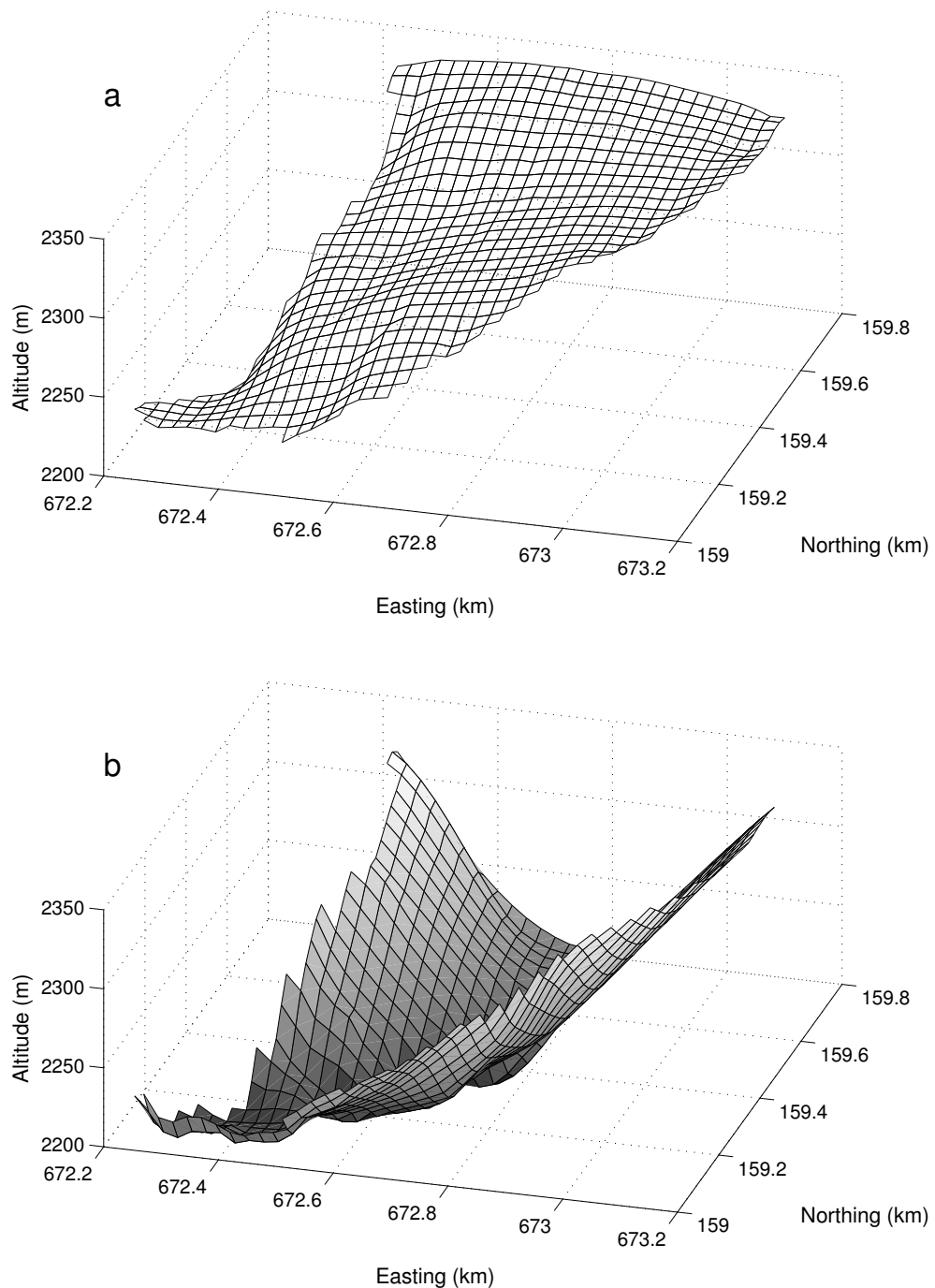


Figure 3.1: Oblique perspective figure of (a) glacier surface in 2009 and (b) bed geometry. One mesh size is 25-m square. The surface elevations are based on DEMs constructed from our GPS kinematic survey in 2009, and the bed elevations are based on boreholes drilled in 2007–2009.

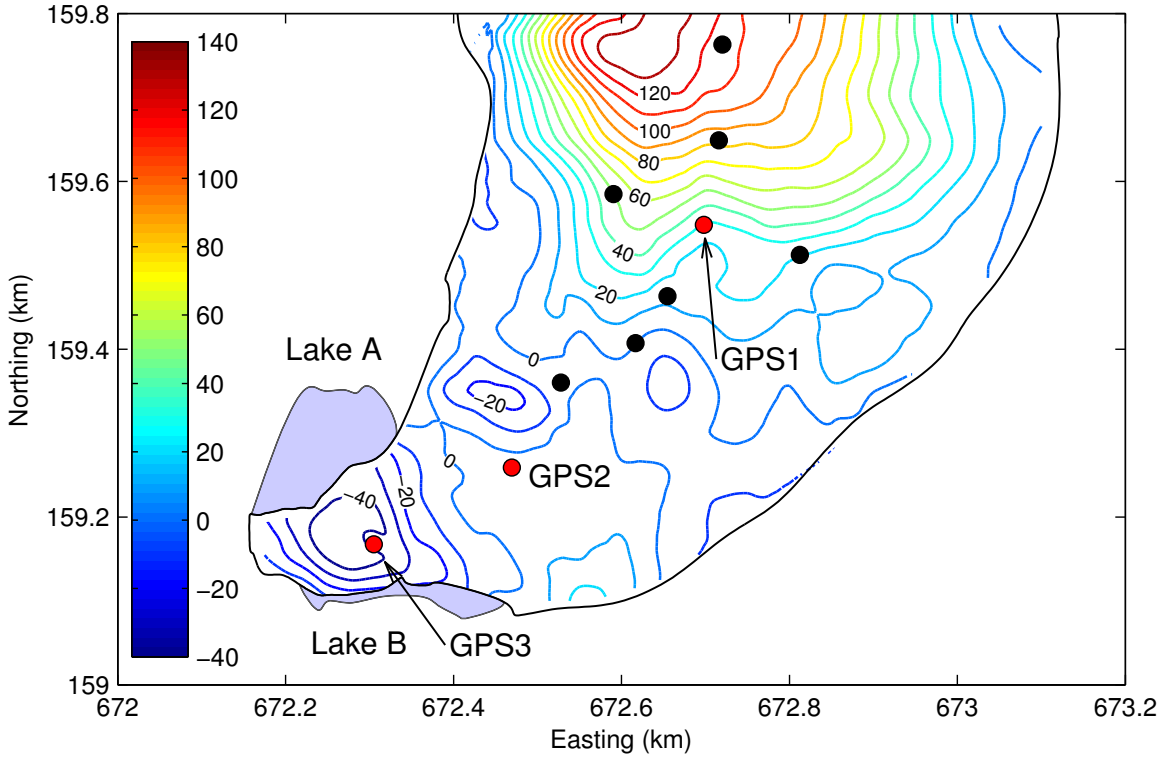


Figure 3.2: Differences in the bed elevation obtained in this study from bed elevation expected from the ice radar data in 2000. The intervals of contour lines is 10 m. Circles indicate the location of GPS1–3 (red) and boreholes drilled in 2007 (black), respectively.

a range of 500–800 m from the terminus obtained from the ice radar data by comparison with the borehole drilling in 2007. As described below, this study provides more accurate bed elevation than previously reported data set. This information is crucial to predict the collapse of the glacier terminus into the lake and the future development of the lake as discussed later in this thesis.

Figure 3.3 shows the change in the surface elevation from 31 July 2008 to 29 July 2009. The elevation lowered by 1–6 m in the study area over the year. The maximum change of -6 m a^{-1} was observed about 100 m north of GPS2. In the terminal area, the magnitude of the elevation change is minimum, which is less than -2 m a^{-1} . The mean thickening rates at surface elevations of 2200–2250 m and 2250–2350 m are -2.15 and -3.44 m a^{-1} , respectively. According to the ice thickness change obtained by comparing DEMs, the rates of thickness change at the elevation of 2250–2350 m for the periods 1874–1929, 1929–1959, 1959–1980, 1980–1991 and 1991–2000 are -0.49 , -0.92 , -0.12 , -0.92 and -1.87 m a^{-1} , respectively (Zahno, 2004). Sugiyama and others (2008a) reported that the rate at 2250–2350 m had

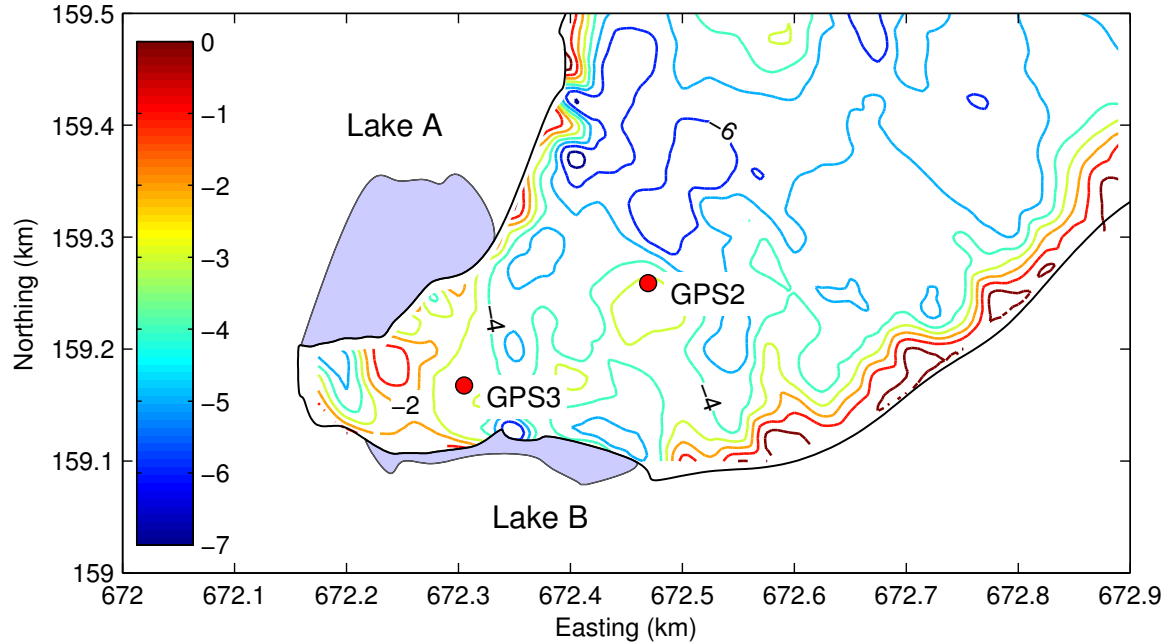


Figure 3.3: Changes in the surface elevation from 31 July 2008 to 29 July 2009, as measured by the GPS kinematic survey. The interval of contour lines is 1 m.

increased to a value of -2.75 m a^{-1} from 2000 to 2007. Accordingly, as a result of this study, the rate of surface elevation change has accelerated over the past two decades.

3.2 Time series of glacier motion and borehole water level

Continuous GPS survey and borehole water level measurements were carried out in the summer seasons of 2007–2009. In this section, short-term fluctuations in the vertical displacement, horizontal flow velocity and borehole water level obtained at GPS1–3 are presented.

2007 (from 14 July to 6 September)

A series of data taken from 14 July to 6 September, 2007 is shown in Figure 3.3. In the beginning of the observation in 2007, the weather was fine with minimum temperature of over 15°C . On 30 and 31 July, weather turned to cold with occasional snowfall. After 9 August, the cold and warm weather came alternately for about a week.

The vertical displacement at GPS1 and GPS3 showed the downward movement over the entire measurement period (Fig. 3.4a). The horizontal flow velocity in the both sites varied diurnally over the entire period (Fig. 3.4b). The flow velocity in GPS1 was higher than the

3.2. TIME SERIES OF GLACIER MOTION AND BOREHOLE WATER LEVEL

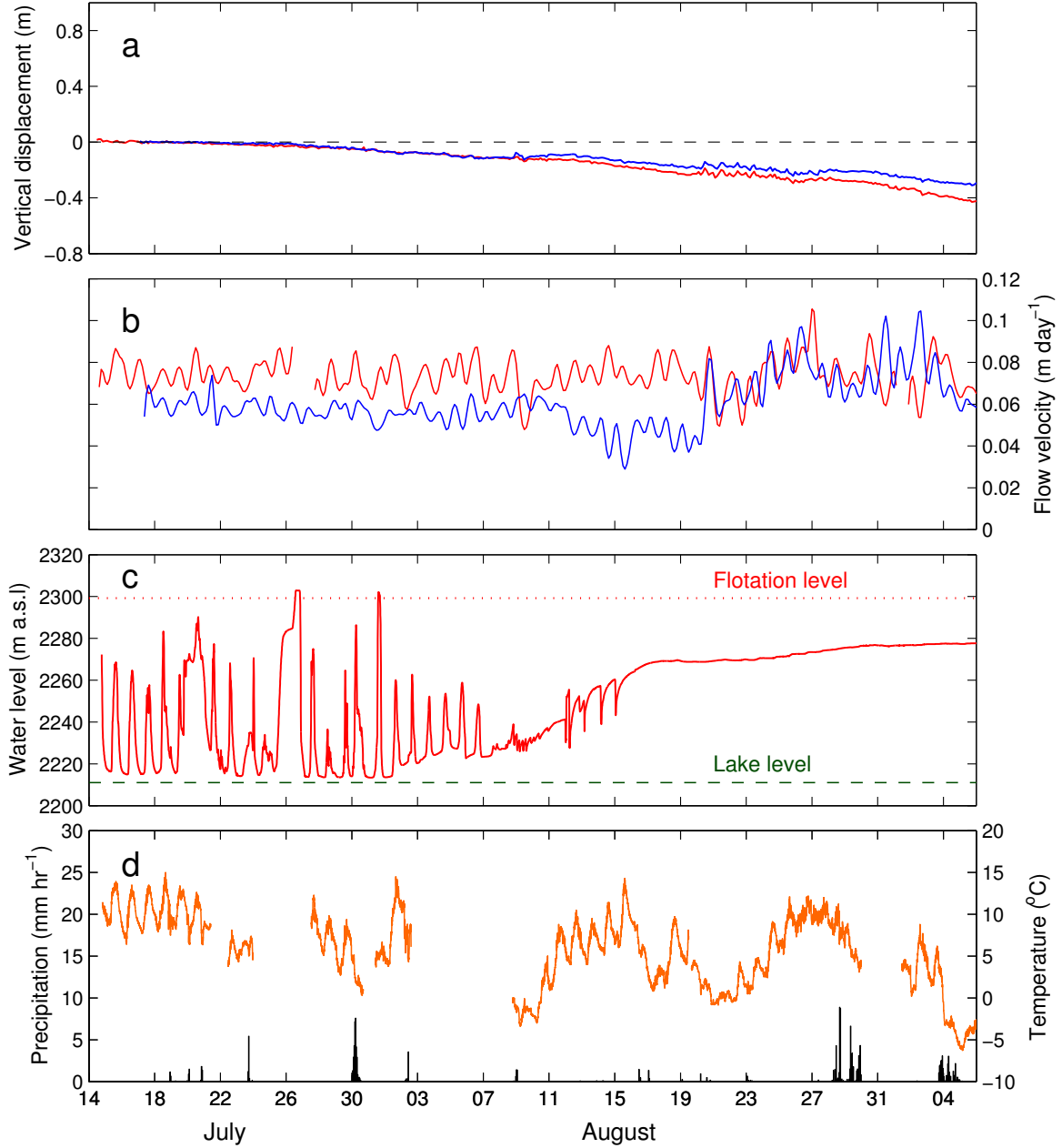


Figure 3.4: Time series of data taken in summer season of 2007. (a) Vertical displacement of the stake at GPS1 (red) and GPS3 (blue) from its original position on 14 July 2007. Dashed line indicates original elevation level on 14 July. (b) Horizontal flow velocity. (c) Water level in GPS1. Dashed line indicates mean lake level. Dotted line is flotation level of ice thickness. (d) Air temperature (orange line) and hourly precipitation.

velocity in GPS3 from 14 July to 20 August. The velocity in GPS3 approached that in GPS1 when weather was cold with maximum temperature of 10 °C on 22 August (Figs. 3.4b and d). The mean velocity at GPS1 for the entire measurement period was 26.46 m a^{-1} . The mean velocity at GPS3 before 22 August was 21.75 m a^{-1} and increased to 25.77 m a^{-1} after 22 August. During the period from 14 July to 6 August, the water level at GPS1 showed diurnal variations (Fig. 3.4c). In contrast to the variable peak water levels, the daily minima were nearly constant until 1 August. The minimum levels were 5–10 m higher than the surface level of the lakes. After 2 August, the water level gradually rose up and the magnitude of diurnal variation decreased. It implies that the connection of the borehole to the basal drainage system was abandoned. This kind of distinct change in water level was also observed in Bench Glacier, Alaska (Fudge and others, 2008).

2008 (from 19 July to 6 September)

The warm weather continued from beginning of observation period to early August. The weather turned from warm to cold on 22 July, 9 and 16 August (Fig. 3.5d). On 22 July, 9 and 16 August, heavy thunderstorms were observed. The observation was interrupted on 15 August, because some of the instruments were damaged by the thunderstorm.

Clear diurnal fluctuations in the horizontal flow velocity were observed in GPS1–3 (Fig. 3.5b). The magnitude of the flow velocity at GPS3 was comparable to those at GPS1 and GPS2. The mean velocities over the entire measurement period in GPS1–3 are 26.94, 28.00 and 25.73 m a^{-1} , respectively. The amplitude of diurnal variations in velocity was smaller at GPS3 than GPS1. The daily maximum velocity at GPS2 was larger than at GPS1 and GPS3. The vertical movement of the glacier surface at GPS1 and GPS2 were downward at rates of -3 and -13 mm d^{-1} , respectively (Fig. 3.5a). In contrast to these stakes, the surface moved upward at GPS3 by up to 150 mm from 10 to 14 August. Then, the movement was downward until 26 August. Surface at GPS3 uplifted again at a rate of 30 mm d^{-1} from 26 August. The period of this uplift event corresponded to the reduction of the amplitude of horizontal flow velocity in GPS3. Borehole water levels at GPS2 and GPS3 showed diurnal fluctuations over the entire observation period. The amplitude of those fluctuations was less than 0.5 m. Water levels in both measurement sites were nearly equal to the mean lake level (Fig. 3.5c). It implies that the subglacial water pressure in the regions of GPS1 and GPS2 was directly controlled by the lake water.

2009 (from 1 July to 5 September)

In the beginning of observation period of 2009, the study site was still covered with snow up to 0.4 m thick. the snow disappeared by late July. On 17 and 18 July, temperature dropped to 7 °C and peak precipitation reached 9 mm h^{-1} . On 2 August, the cold weather came again with heavy rain or snowstorm and the precipitation was up to 30 mm h^{-1} (Fig. 3.6d).

3.2. TIME SERIES OF GLACIER MOTION AND BOREHOLE WATER LEVEL

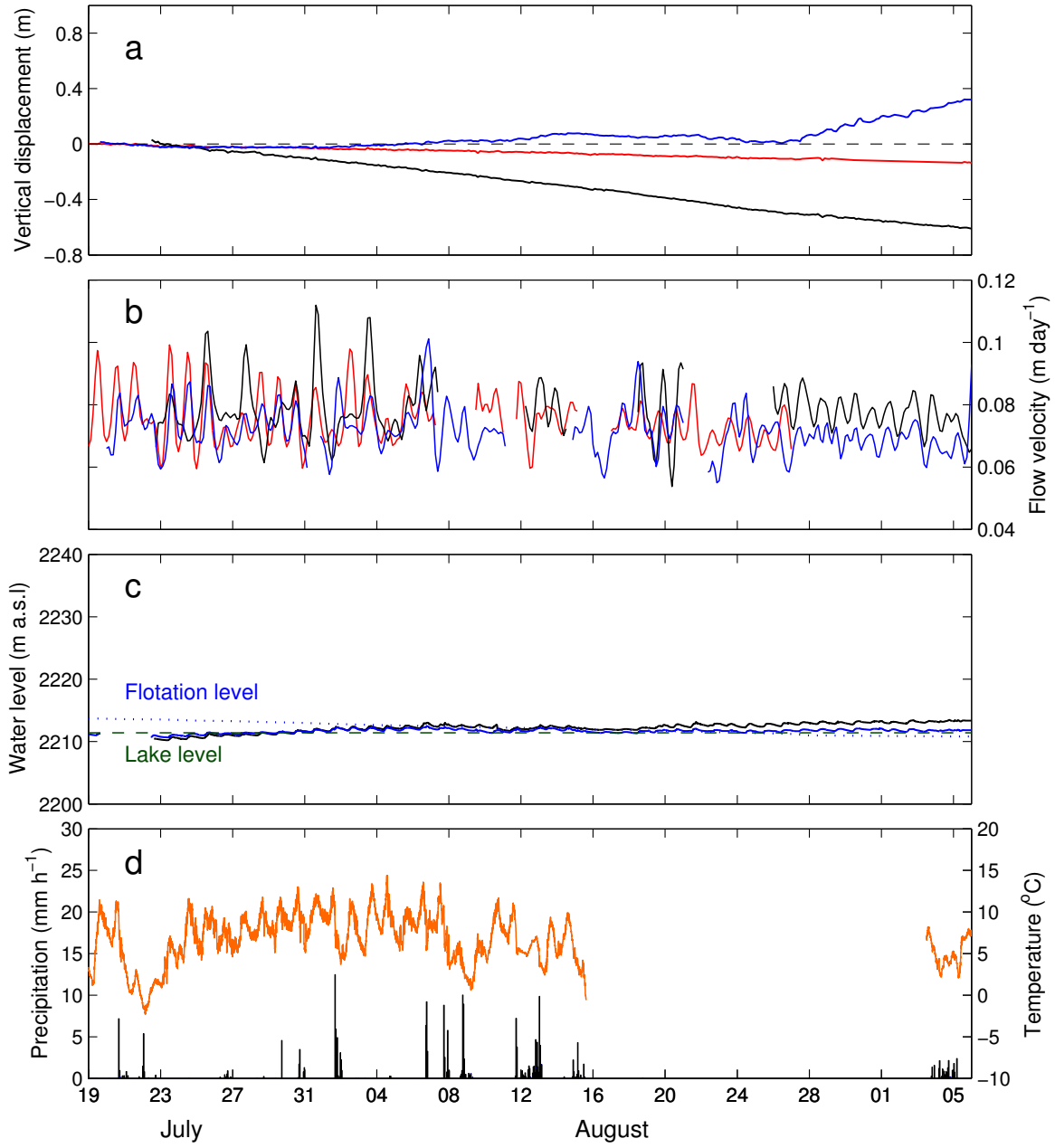


Figure 3.5: Time series of data taken in summer season of 2008. (a) Vertical displacement of the stake at GPS1 (red), GPS2 (black) and GPS3 (blue) from its original position on 19 July 2008. Dashed line indicates original elevation level on 19 July. (b) Horizontal flow velocity. (c) Water level in GPS2 (black) and GPS3 (blue). Dashed line indicates mean lake level. Dotted line is flotation level of ice thickness. (d) Air temperature (orange line) and hourly precipitation.

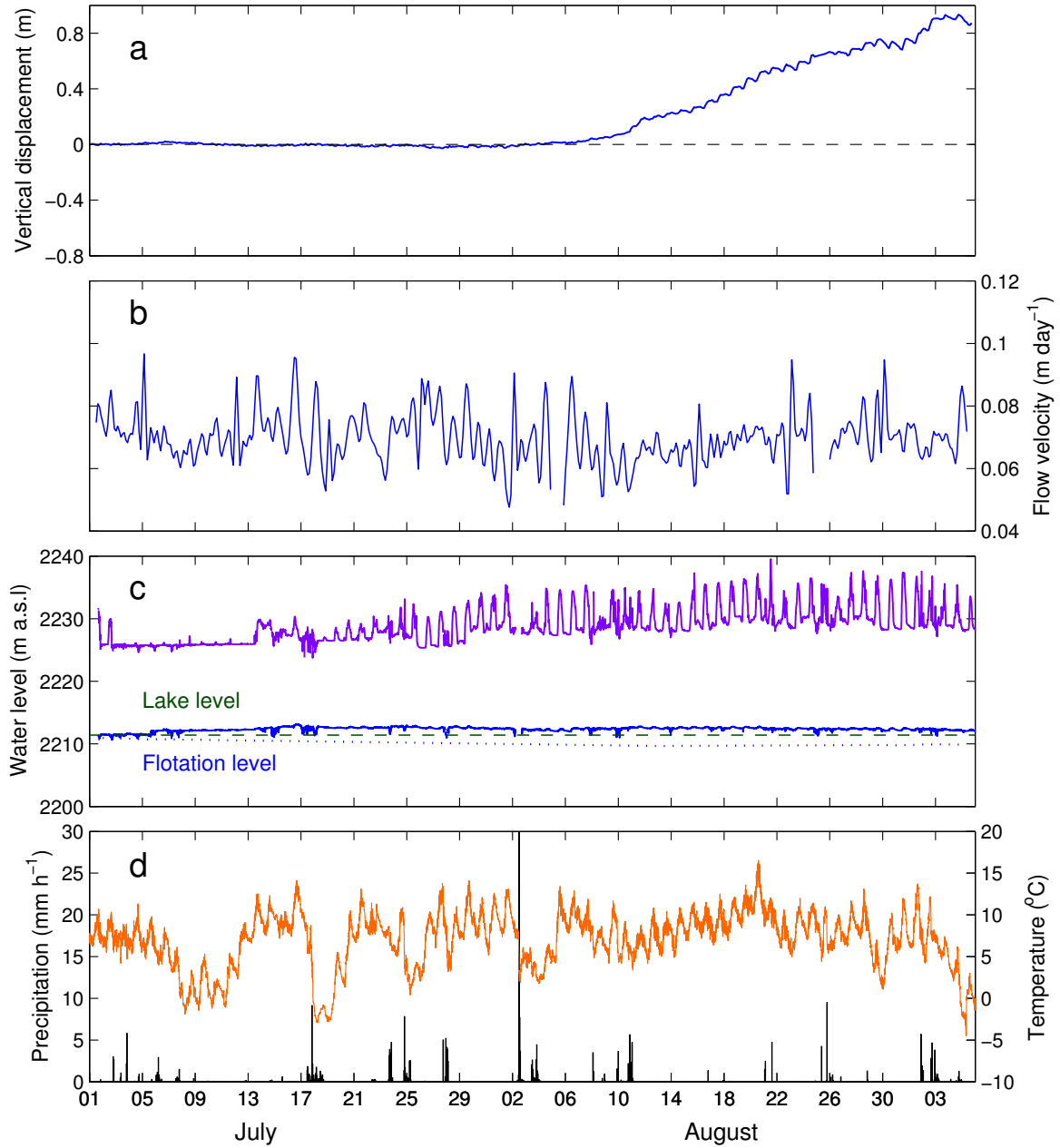


Figure 3.6: Time series of data taken in summer season of 2009. (a) Vertical displacement of the stake at GPS3 from its original position on 1 July 2009. Dashed line indicates original elevation level on 1 July. (b) Horizontal flow velocity. (c) Water level in GPS3 (blue) and BH904 (purple). Dashed line indicates mean lake level. Dotted line is flotation level of ice thickness. (d) Air temperature (orange line) and hourly precipitation.

The horizontal flow velocity at GPS3 varied diurnally until early August (Fig. 3.6b). From 11 August, the amplitude of the diurnal fluctuations decreased. The glacier surface level changed little from early July to early August (Fig. 3.6a). The rate of the vertical displacement increased and the amplitude of the diurnal fluctuations reduced at about 11 August. The glacier uplift continued until 5 September at a rate of 30 mm d^{-1} , and the vertical movement turned to downward on 6 September. During the period of upward motion, the vertical displacement showed small diurnal fluctuations. Borehole water level at GPS3 varied diurnally, as observed in 2008. The water level in BH904, located about 300 m upglacier from GPS3 (dark gray square in Fig. 2.5b) showed little variation from 3 to 14 July. Then, diurnal fluctuations were observed from middle July. It implies that the connection of basal drainage system was developed at this time of the season. The daily minimum level was nearly constant, which was 15–20 m higher than the mean lake level.

3.3 Glacier flow fields in 2008 and 2009

The surface flow velocity fields in the summers of 2008 and 2009 are shown in Figure 3.7a and Table 3.1. In 2008, the greatest velocity was 35.92 m a^{-1} at Stake 15 which was located very close to the terminus. The velocity was generally larger near the terminus than in the upper reaches. For example, the velocities at Stakes 10 (26.38 m a^{-1}) and 13 (25.13 m a^{-1}) were 6% greater than those of Stakes 2 (24.92 m a^{-1}) and 3 (23.81 m a^{-1}). From Stake 10 to Stake 15, the velocity increases by 36% over a distance of 150 m. In 2009, the velocity at Stake 15 was 46% less than in 2008. The upper reaches also decelerated: the velocities of Stakes 1–4 reduced by 18% in average. Despite this trend, the ice at the lake front still flowed rapidly in 2009. The velocities at Stakes 16 (21.52 m a^{-1}), 17 (23.79 m a^{-1}) and 18 (21.23 m a^{-1}) are large compared to those observed at the termini of other valley glaciers of similar size (e.g. Hooke and others, 1989; Iken and Truffer, 1997; Luckman and others, 2007).

Very large upward motion was observed at the stakes located near the lake front. The vertical velocities at Stakes 9, 15 and 16 were more than 20 m a^{-1} in 2009 (Fig. 3.7b and 3.1). The data at Stake 15 show that the ice moved upwards at a similar rate in 2008. The vertical velocity at GPS3 increased from 4.61 m a^{-1} in 2008 to 6.48 m a^{-1} in 2009. The ice motion was downwards at all other stakes in the studied region.

Table 3.1: Horizontal (u_h) and vertical (u_z) velocities measured in summer seasons of 2008 (18 July–7 September) and 2009 (27 June–6 September).

Stake No.	2008		2009	
	u_h m a ⁻¹	u_z m a ⁻¹	u_h m a ⁻¹	u_z m a ⁻¹
GPS2	29.62	2.72	—	—
GPS3	25.93	4.61	25.60	6.48
Stake 1	24.82	0.78	18.71	-0.79
Stake 2	24.92	1.23	20.92	-0.41
Stake 3	23.81	-0.02	19.94	0.87
Stake 4	15.69	-1.45	13.91	-1.18
Stake 5	27.45	-0.45	24.20	-3.83
Stake 6	27.59	0.67	24.34	0.99
Stake 7	22.54	-0.28	16.68	-2.22
Stake 8	24.65	7.67	—	—
Stake 9	—	—	17.45	28.13
Stake 10	26.38	-1.43	—	—
Stake 11	—	—	22.90	-4.23
Stake 12	28.55	-0.89	—	—
Stake 13	25.13	0.04	—	—
Stake 14	22.84	0.63	17.47	-2.66
Stake 15	35.92	25.10	19.44	20.82
Stake 16	—	—	21.52	21.27
Stake 17	—	—	23.79	1.21
Stake 18	23.99	7.19	21.23	1.59
Stake 19	23.03	0.94	—	—
Stake 20	18.21	-0.80	19.13	-1.03

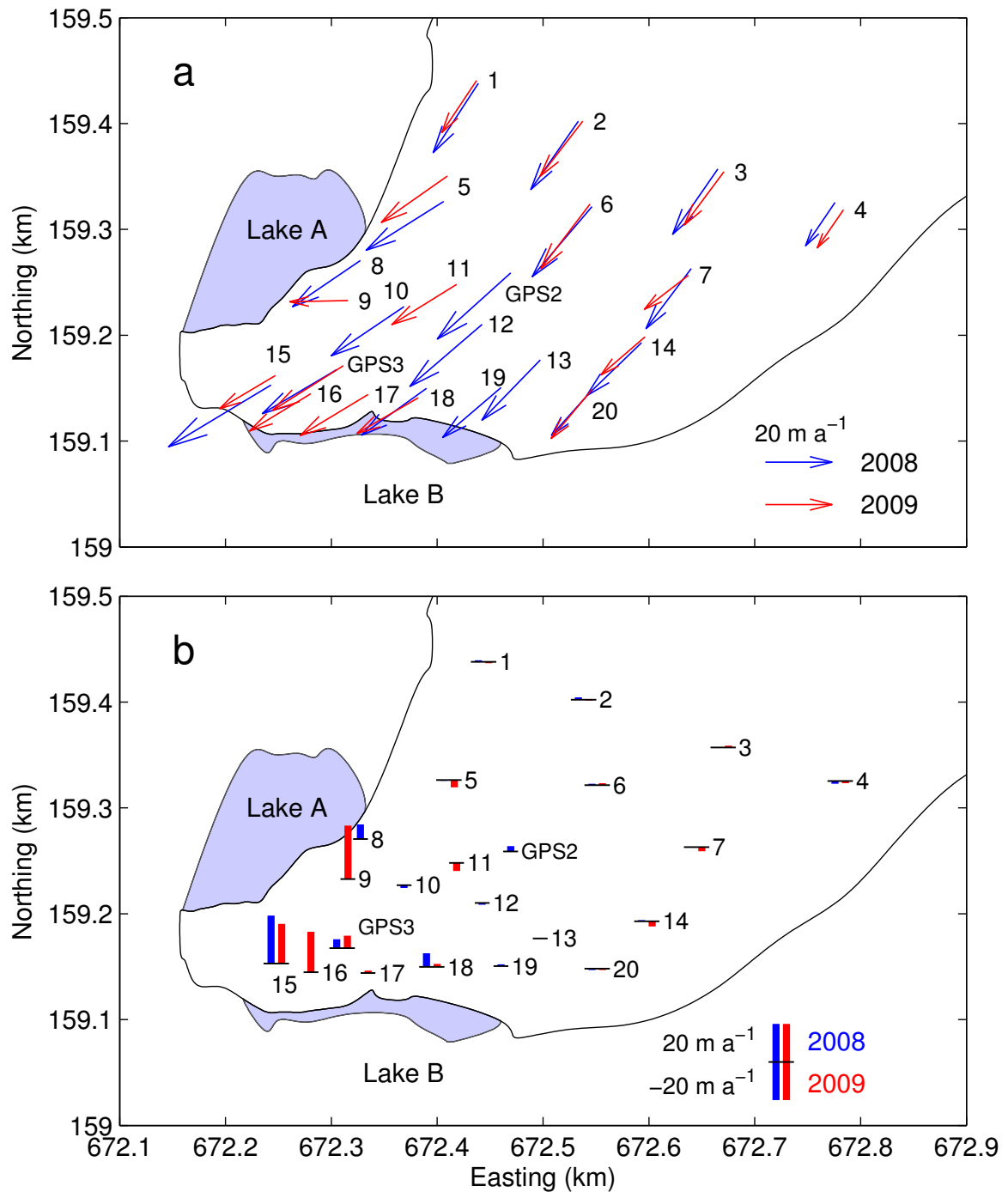


Figure 3.7: (a) Horizontal flow vectors measured in 2008 (blue) and 2009 (red). (b) Vertical flow velocities measured in 2008 (blue) and 2009 (red).

3.4 Borehole water level

The mean water levels during the measurement periods in 2008 and 2009 are depicted along the longitudinal profile of the glacier bed in Figure 3.8b. In the upper reaches, at BH801, 806, 807, 808 and 920, subglacial water pressure varies significantly. In contrast, at BH801 and 819, water levels were at or near the ice surface with little or no variation during the entire measurement period. Borehole water levels were nearly equal to the lake level within 5 m over the range of 300 m from the glacier terminus. According to the bed geometry obtained in this study, the bed elevations are below the lake level at boreholes located in the terminal area (Fig. 3.8a). At BH813 and 909, in the eastern side of the glacier, water had completely drained from the borehole and the tip of float sensor had hit on solid rock at the bottom of the borehole. The bottom of these boreholes are located slightly above the lake level.

3.5 Summary

GPS survey and borehole water level measurements were carried out with a high spatial resolution during the ablation seasons of 2007–2009 in Rhonegletscher. Important observations in the field measurements are summarized below.

1. Surface and bedrock DEMs are constructed by GPS survey and borehole drilling. Obtained bedrock elevation is up to 40 m lower at the terminus and 120 m higher at the upglacier than those from the previously reported ice-radar data (Zahno, 2004). Mean surface lowering rate from 2008 to 2009 is -2.15 m a^{-1} in 2200–2250 m and -3.44 m a^{-1} in 2250–2350 m, respectively.
2. Horizontal flow velocity was greater than 20 m a^{-1} at Stakes 8, 9, 15, 16, 17 and 18 and GPS3 near the glacier terminus. These flow velocities were similar to the velocity at Stakes 1–7, located in the upper reaches of the study area. In the vicinity of the lake, at Stakes 9, 15 and 16, the ice surface moved upward at a rate greater than 20 m a^{-1} in 2008 and 2009.
3. Mean borehole water levels were nearly equal to the lake level within 5 m over the range of 300 m from the glacier terminus. In the upper reaches, at BH801, 806, 807, 808 and 920, subglacial water pressure varies significantly during the ablation season. At BH813 and 909, in the eastern side of the glacier, water had completely drained from the borehole.

The surface velocity and borehole water level were observed with a high spatial resolution. The rate of ice thinning has increased over the past 20 years. To investigate the processes and mechanisms of rapid glacier retreat caused by lake formation, these observed data are examined and discussed in the next chapter.

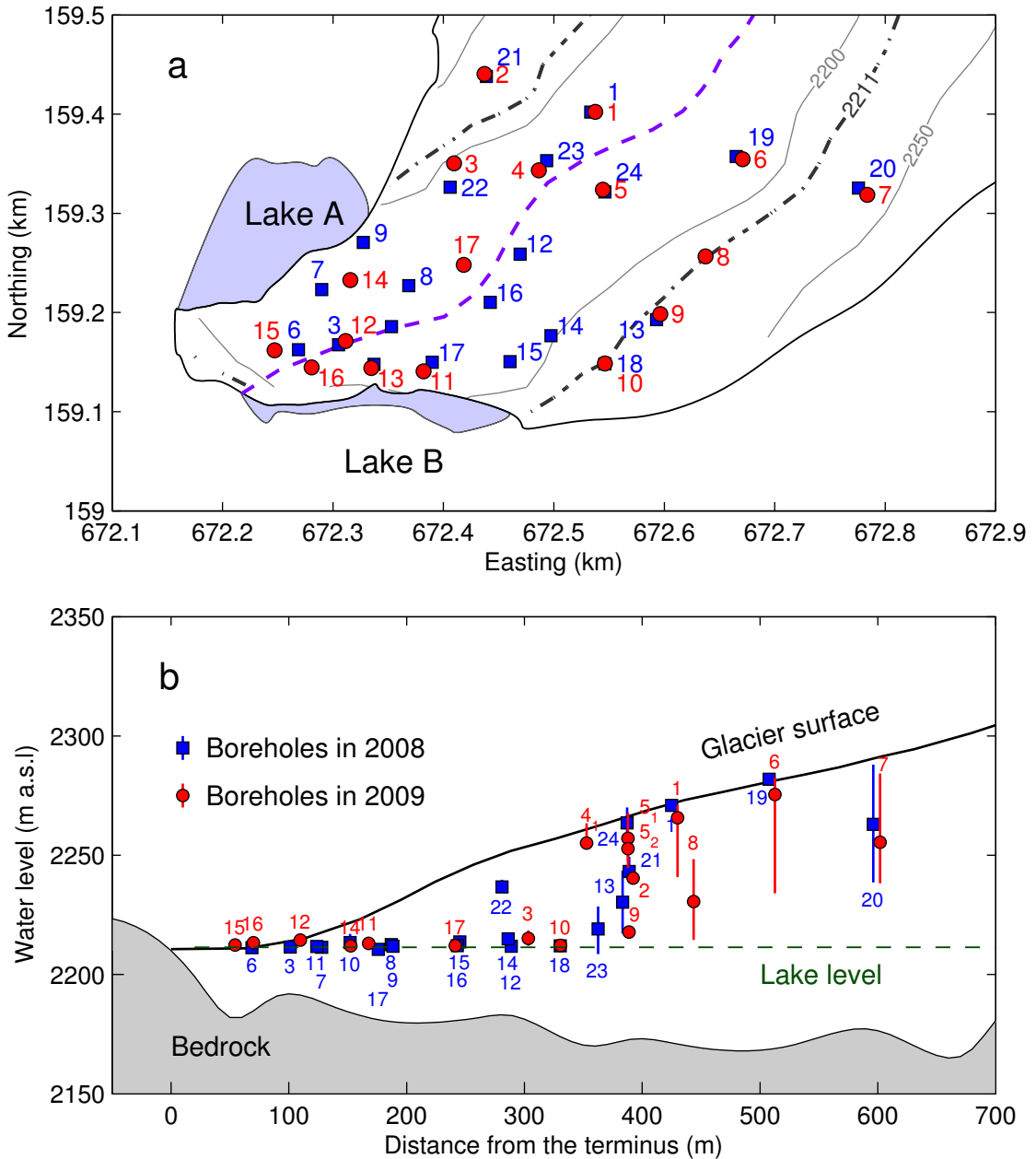


Figure 3.8: (a) The Locations of boreholes used for water level measurement in 2008 (blue, square) and 2009 (red, circle). The contours indicate bedrock elevation with intervals of 50 m. Along the dotted line, the bed elevation is equal to the lake level. (b) Mean water levels measured in the boreholes in 2008 (blue, square) and 2009 (red, circle). The markers are indicated using the distance from the boreholes to the glacier terminus as the abscissa. The vertical lines indicate the range of water level during the measurement periods. The dashed line is the lake level. The shaded area indicate the bedrock along the dashed purple line depicted in (a).

Chapter 4

Field data interpretations

Observed horizontal flow field and surface upward movement are analyzed in detail and interpreted in this chapter. Horizontal flow velocity is compared with that observed before the formation of Lake B. Horizontal strain rate is derived from the spatial distribution of horizontal flow velocity to interpret dynamic thinning of ice thickness. Spatial distribution of the effective pressure was calculated by using DEMs of surface and bed to test the floating condition near the lake.

4.1 Ice flow acceleration in the terminus

4.1.1 Changes in ice flow speed before and after the lake formation

We investigate the influence of the lake formation on the ice flow speed by comparing our observations at GPS1 and GPS3 from 2007 to 2009 with those reported in previous studies. Horizontal flow velocities before the formation of Lake B were measured by analysis of aerial photographs by Nishimura (2008). Photographs taken in 9 September 1999, 23 August 2000, 15 September 2005 and 5 September 2006 were used for the analysis. The annual horizontal flow speed was measured at the grid points of 100 m mesh during the periods of 1999–2000 and 2005–2006. Estimated error of the measured flow velocity is 4 m a^{-1} . To compare the two data, the flow velocity measured using aerial photographs was interpolated to the coordinates of GPS1 and GPS3. Note that our measurements were made in summer, while the reported data represent annual velocities. Annual velocity was estimated from the summer velocity as described below. In this study, annual flow velocities at Stakes 2 and 3 were measured from 7 September 2008 to 26 June 2009. Measured annual velocities were 14.19 m a^{-1} at Stake 2 and 13.06 m a^{-1} at Stake 3. The annual velocity at Stake 2 was 57% of the summer velocity in 2008 and 68% of that in 2009. At Stake 3, the annual velocity was 55% of the summer velocity in 2008 and 66% of that in 2009. Assuming the same relationship at GPS1 and GPS3, annual velocity was estimated as 16.64 and 13.64 m a^{-1} in 2007–2008 and 16.93 and 16.68 m a^{-1} in 2008–2009. Time series of annual flow velocities are shown in Figure 4.1.

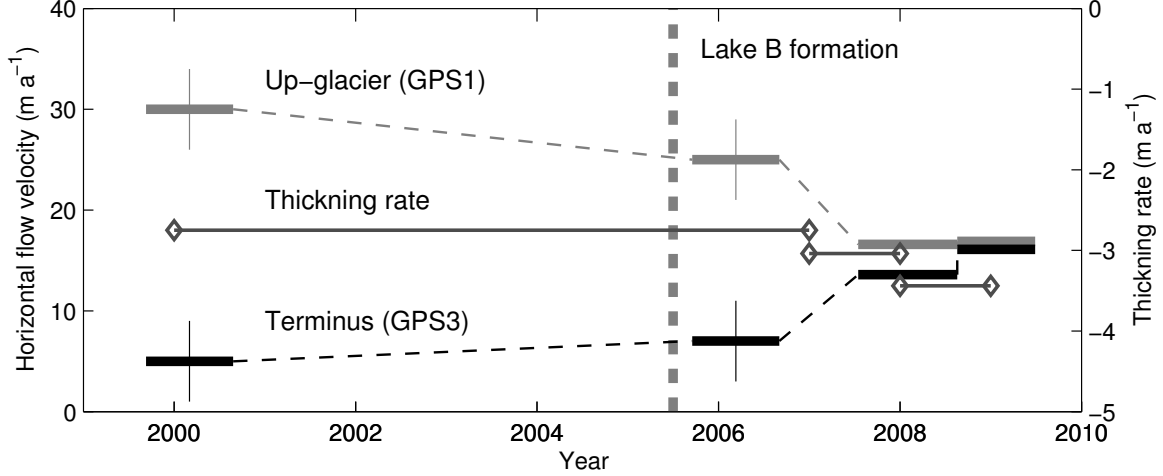


Figure 4.1: Horizontal flow velocities at GPS1 and GPS3 from 2000 to 2009. Thin and black lines indicate the velocities at GPS1 and GPS3, respectively. Thin line with open diamond indicates the thickening rate. Vertical dashed line indicates the time of Lake B formation. The flow velocity of 2000 and 2006 were obtained by the interpolation of flow velocity calculated by aerial photographs (Nishimura, 2008).

From 1999–2000 to 2005–2006, before and after Lake B forming, the flow velocity at GPS3 increased by 40% and decreased by 17% at GPS1. The velocities at both measurement sites had changed significantly from 2005–2006 to 2007–2008. The velocity increased by 100% at GPS3 and decreased by 33% at GPS1. After the speed up, the ice flow velocity at the terminal part of Rhonegletscher is significantly faster than that observed in similar temperate alpine glaciers without proglacial lakes (e.g. Hooke and others, 1989; Iken and Truffer, 1997; Luckman and others, 2007). From 2007–2008 to 2008–2009, The velocities at GPS1 and GPS3 increased by 2% and 18%, which became relatively steady. The velocity at GPS3 closed to that at GPS1 is also shown in Figure 3.5b.

Decreases in the surface flow velocity at GPS1 is probably due to the thinning of the ice. The surface velocity u_s in an uniformly inclined infinitely wide glacier is expressed as:

$$u_s = u_b + \frac{2A}{n+1}(\rho_i g \sin \alpha)^n H^{n+1}, \quad (4.1)$$

where u_b is the sliding velocity, ρ_i is the density of ice, α is surface slope and g is the gravitational acceleration (e.g. Nye, 1952; Hooke, 2005). A is the rate factor. The power index is often taken as $n = 3$. Equation (4.1) indicates that the surface velocity is proportional to the 3rd power of the surface slope and to the 4th power of the ice thickness. The mean changing rate of the ice thickness at elevations of 2250–2350 m during the periods 2007–2008 and 2008–2009 are depicted in Figure 4.1. Sugiyama and others (2008a) reported that the

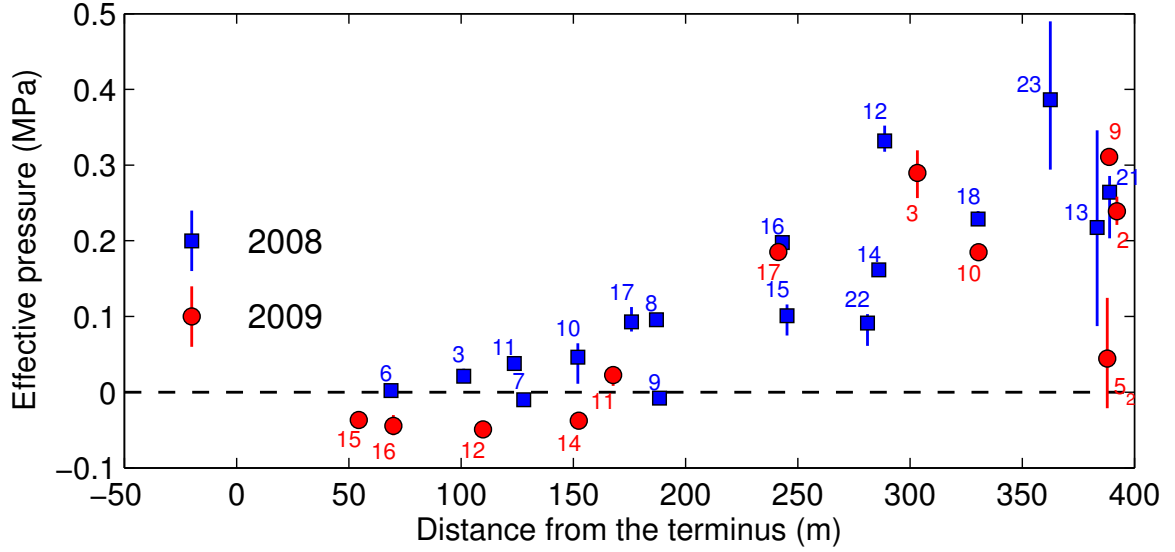


Figure 4.2: Mean effective pressure calculated from each borehole depth and water level drilled in 2008 (blue, square) and 2009 (red, circle). The vertical lines indicate the range of effective pressure during the measurement periods. Numbers of borehole are listed in Table 2.1.

rate had increased from -1.87 m a^{-1} in 1991–2000 to -2.75 m a^{-1} in 2007. This study shows the rate for the same elevation range as -3.04 m a^{-1} in 2007–2008 and -3.44 m a^{-1} in 2008–2009. This result indicates that the glacier is thinning at a progressively increasing rate in the 21st century. Assuming that the basal sliding is 0 m a^{-1} and surface slope is constant in time, surface velocity at GPS1 estimated from Equation (4.1) as 29.7 , 19.0 and 13.7 m a^{-1} in 2000, 2006 and 2009, respectively. Ice flow decelerated in the upper reaches probably because the ice deformation rate decreased as the ice thinned.

4.1.2 Mechanisms of flow acceleration

The subglacial water pressure in the range of 300 m from the terminus was directly controlled by the lake water (Fig. 3.8). Water cavity formation and its sustainability are controlled by water pressure. Once a water cavity is formed, water pressure is considered to push the ice sole forward with hydraulic-jack effect (Röthlisberger, 1981). It is suggested that a subglacial drainage system in the terminal part of glacier has been developed during the entire ablation season. Water level of Lake A was about 1.7 m below the ice surface in 2008. If we consider the ice thickness at this location, 102% of the ice overburden pressure was cancelled by the lake water pressure. It is likely that the formation of the lake increased subglacial water pressure at the glacier terminus. The spatial distribution of effective pressure P_e is calculated as:

$$P_e = \rho_i g(z_s - z_b) - \rho_w g(z_w - z_b), \quad (4.2)$$

where $\rho_i = 910 \text{ kg m}^{-3}$ and $\rho_w = 1000 \text{ kg m}^{-3}$ are ice and water densities, respectively, and $g = 9.81 \text{ m s}^{-2}$ is the gravitational acceleration. Glacier surface, bed elevation and lake level are represented as z_s , z_b and z_w , respectively. Figure 4.2 shows the effective pressure plotted against the locations of borehole along the longitudinal profile of the glacier. The effective pressure was obtained from water pressure measured in the periods from 24 July to 6 September 2008 and from 26 June to 5 September 2009. The overburden pressure was calculated from the local ice thickness determined from the hot water drilling (Table 2.1). A scatter plot of the data from the two observation periods shows that effective pressure approaches zero at the borehole near the terminus. At BH807, 809, 912, 914, 915 and 916, subglacial water pressure exceeded ice overburden pressure.

The acceleration from 2005–2006 to 2007–2008 at GPS3 occurred within a period of 2–3 years after the first recognition of Lake B in 2005. It is implied that high water pressure enhanced basal motion. The relationship between subglacial water pressure and surface flow velocity has been studied theoretically and by field measurement with high temporal resolution (e.g. Weertman, 1957; Iken, 1981; Iken and Bindschadler, 1986; Sugiyama and Gudmundsson, 2004). According to these works, the high subglacial water pressure reduces the friction at the ice-bed boundary. This is because water submerges small obstacles on the bed. The surface velocity increases exponentially when the subglacial water pressure attains ice overburden pressure (e.g. Iken and Bindschadler, 1986; Kamb and Engelhardt, 1987; Sugiyama and Gudmundsson, 2004). Ice flow mechanisms at the terminus in the lake terminating glacier have been discussed in previous studies. Motyka and others (2002) calculated the flow velocity at the terminus of Mendenhall Glacier in Alaska, using a simple flow law of ice. They noted that the deformational flow can only account for about 5 m a^{-1} of the surface velocity, and the rest (87 m a^{-1}) is due to basal motion. In Rhonegletscher, assuming the ice thickness at GPS3 in 2008 as 20 m, surface flow speed estimated from Equation (4.1) is only several millimeters per year. Thus, nearly 100% of the surface flow observed in this study was caused by basal ice motion.

An additional effect on glacier flow velocity is the separation of glacier terminus in front of Lake B from the bedrock bump (Fig. 2.2b). Meier and Post (1987) studied rapid velocity increases at the terminus of Columbia Glacier in Alaska. They concluded that the speedup was caused partly by the release of back pressure (longitudinal normal stress) due to the seasonal calving retreat of the terminus. Naruse and Skvarca (2000) suggested that rapid glacier retreat observed in Glaciar Upsala, Southern Patagonia should be affected by the bed topography in terms of normal stress.

4.2 Dynamic thinning

The velocities near Lake A and Lake B are comparable with those in the upper reaches (Fig. 3.7a). In this respect, the flow regime of Rhonegletscher is similar to the observation

by Moteika and others (2002) at Mendenhall Glacier. They calculated strain rates from triangular net measurement of horizontal flow velocity near the glacier terminus. Results showed 0.25 and 0.16 a^{-1} of tensile strain rates, which were oriented in the direction of glacier flow. Figure 4.3a shows the plot of horizontal flow velocity at GPS1–3 measured in 1999–2000, 2005–06, 2007–08 and 2008–09 against the locations of GPS measurement along the longitudinal profile. The velocity in the upper reaches (GPS1) was higher than that near the terminus (GPS3) in 1999–2000 and 2005–06 before the formation of Lake B. After the lake formation, the velocity at GPS3 was nearly equal to that at GPS1.

Here, we define a coordinate system with the x -axis along the flow direction pointing up-glacier, the y -axis across of the glacier pointing East, and the z -axis vertical upward. Figure 4.3b shows horizontal strain rates $\dot{\varepsilon}_x$ calculated as:

$$\dot{\varepsilon}_x = \frac{u_{x2} - u_{x1}}{x_2 - x_1}, \quad (4.3)$$

where u_{x1} and u_{x2} are flow velocities measured at x_1 and x_2 , which are the coordinates of GPS position. Result shows tensile strain rates in 1999–2000 before the formation of Lake B: -0.079 a^{-1} between GPS2 and 3, and -0.029 a^{-1} between GPS1 and GPS2, respectively. In 2005–06, the strain rate is -0.079 a^{-1} at GPS2–3 and -0.009 a^{-1} at GPS1–2. The strain

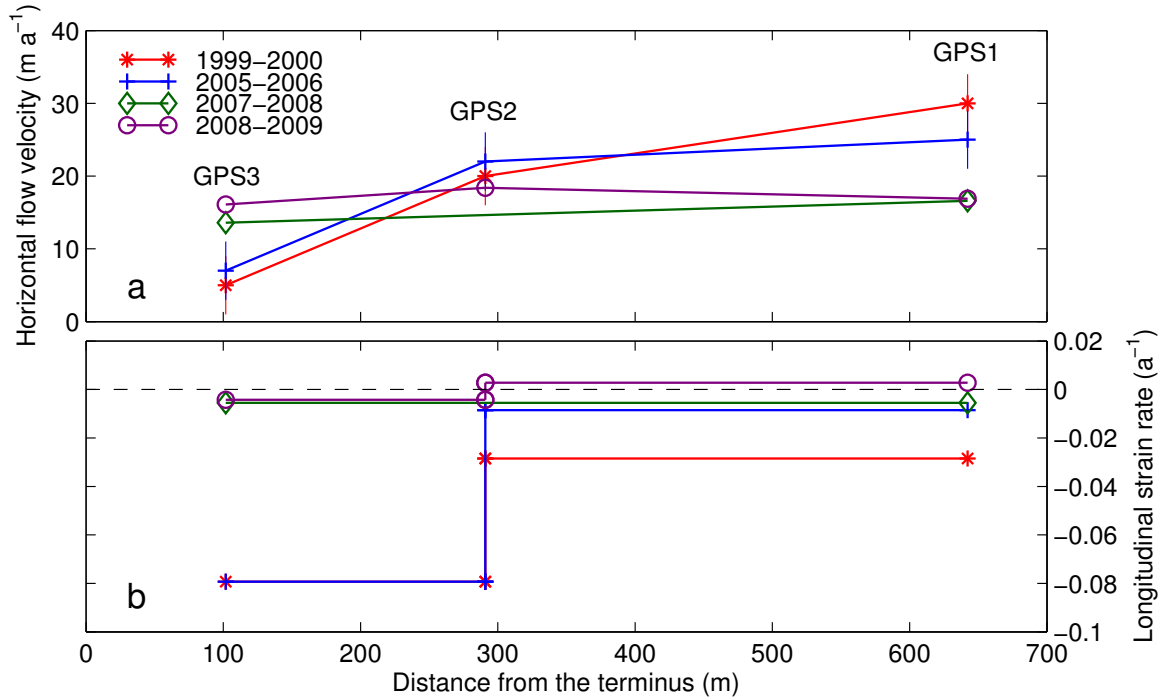


Figure 4.3: (a) Horizontal flow velocity and (b) strain rate in 1999–2000 (red), 2005–2006 (blue), 2006–2007 (green) and 2007–2008 (purple).

rate is significantly more tensile near the glacier terminus in 2007–08 after the formation of the lake. The strain rate between GPS2 and 3 was -0.004 a^{-1} . In valley glaciers, the transverse strain rate $\dot{\varepsilon}_y$ is usually sufficiently smaller than the longitudinal strain rate $\dot{\varepsilon}_x$. If we neglect the transverse strain rate, the vertical strain rate $\dot{\varepsilon}_z$ is obtained as $\dot{\varepsilon}_z = -\dot{\varepsilon}_x$ (Fujii and others, 1997). The vertical strain rates measured at GPS3 from 24 July 2008 to 17 July 2009 shows that $\dot{\varepsilon}_z$ was negative over the entire measurement period (Yoshizawa, 2010). This result indicates that the horizontal flow regime near the terminus would cause thinning of ice thickness.

To discuss the observed increase in the ice flow speed, the spatial distribution of surface strain rate is calculated from horizontal velocities measured between 3 July and 5 September 2009 (Fig. 4.4). The GPS network was tessellated into individual triangles. Two dimensional surface strain on the glacier was analyzed with the method described by Brunner and others (1981). The spatial strain distribution shows a clear tensile strain regime along the flow direction in the entire of measurement area. The highest strain rate (0.32 a^{-1}) was observed at the triangle constructed from GPS3–9–15. Similarly high strain rate was observed at the triangles of 9–11–18 and GPS3–9–18 (0.31 a^{-1}). The strain rates at GPS3–9–15 and GPS3–9–18 oriented approximately west–east, across the glacier flow. Ice is compressed in the area between these triangles. According to these results, tensile flow regime has affected to decrease in ice thickness after the proglacial lake formation. Similar tensile strain regime near the terminus has been observed previously before a significant calving event in Mendenhall Glacier and Columbia Glacier (Venteris and others, 1997; Boyce and others, 2007). The important aspect of the temporal and spatial variations in horizontal strain regime is that both ice dynamics and ablation were affecting the change in the ice thickness. During the last decade, the increase in the thinning rate is influenced by these factors.

4.3 Surface uplift

4.3.1 Uplift and crevasse formation in the terminus

Continuous GPS measurements at GPS3 show upward movement of glacier surface in August of 2008 and 2009 (Figs 3.5a and 3.6a). The uplift might have been caused by subglacial water pressure elevated above the flotation level. To test this hypothesis, we compare the borehole water level with the flotation level of ice thickness h_f calculated as:

$$h_f = z_b + H \frac{\rho_i}{\rho_w}, \quad (4.4)$$

where z_b is the bed elevation, H is the ice thickness, and ρ_w and ρ_i are densities of water and ice, respectively. Temporal changes in the ice thickness due to surface melt and vertical strain were corrected. Water level in borehole showed diurnal fluctuations within 0.5 m during the entire periods in 2008 and 2009 (Fig. 4.5a and c). A clear relationship between

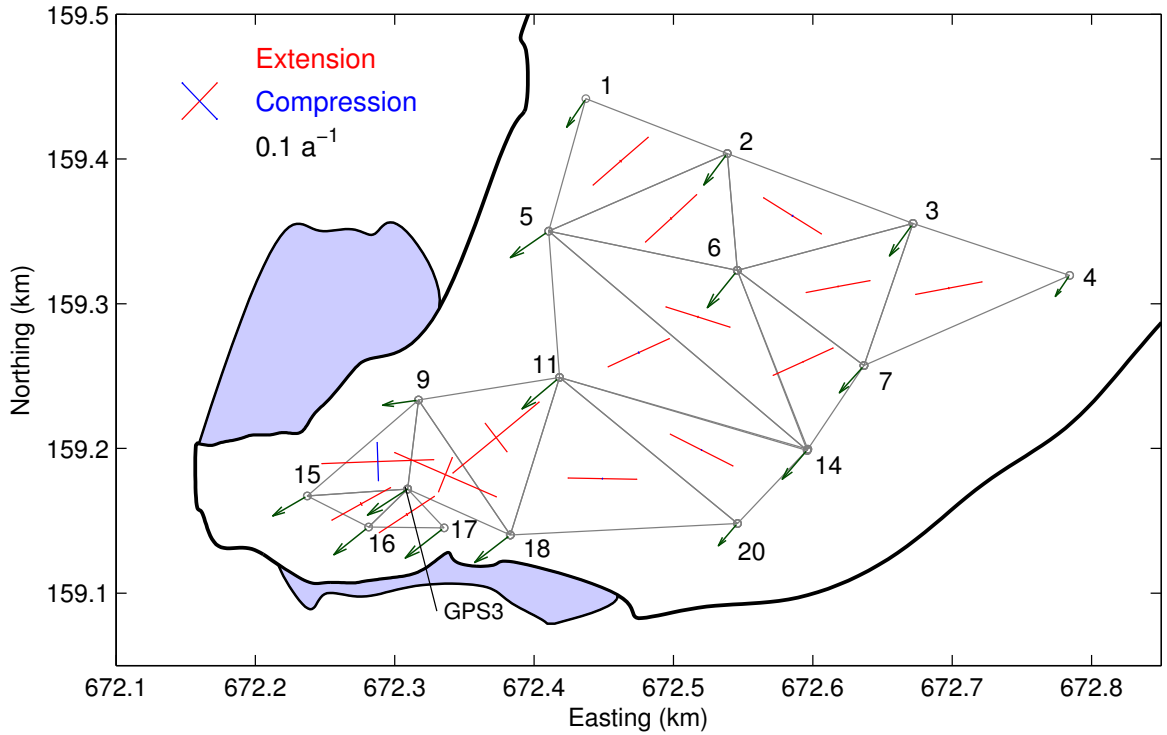


Figure 4.4: Spatial distribution of horizontal strain rate, calculated from measured velocities for the time period 3 July–5 September 2009 (Fig. 3.7a). Red and blue bars indicate extending and compressive flow regime, respectively. Vectors indicate horizontal flow velocities.

vertical displacement and subglacial water pressure was not found in this study, though this relation has been observed at the terminus of Mendenhall Glacier in Alaska (Boyce and others, 2007) and during a lake outburst flood event from ice-dammed lake at Kennicott Glacier in Alaska (Walder and others 2005; 2006). As a result of ice thinning due to surface melt and compressive vertical strain, the water level exceeded the flotation level about two days before the uplift in 27 August 2008 (Fig. 4.5b). The uplift in 2009 occurred more than a month after the flotation condition was satisfied (Fig. 4.5d). Mean rate of upward movement is approximately 3 cm d^{-1} in both years.

The uplift of ice surface was also observed at Stakes 9, 15, 16 (Fig. 3.7b). As shown in Figures 4.2, 4.5b and d, subglacial water pressure near the terminus has exceeded the ice overburden pressure since the ablation season of 2008. To examine whether the conditions for floating are met in the entire part of Rhonegletscher tongue, the effective pressure distribution is computed from Equation 4.2. Hydraulic head within the glacier was assumed to be equal to the lake level, which is constant in time ($z_w = 2211.4 \text{ m}$). The ice surface z_s and bed elevations z_b are given by the DEMs in 2009 constructed in this study (Fig. 3.2a and b). In

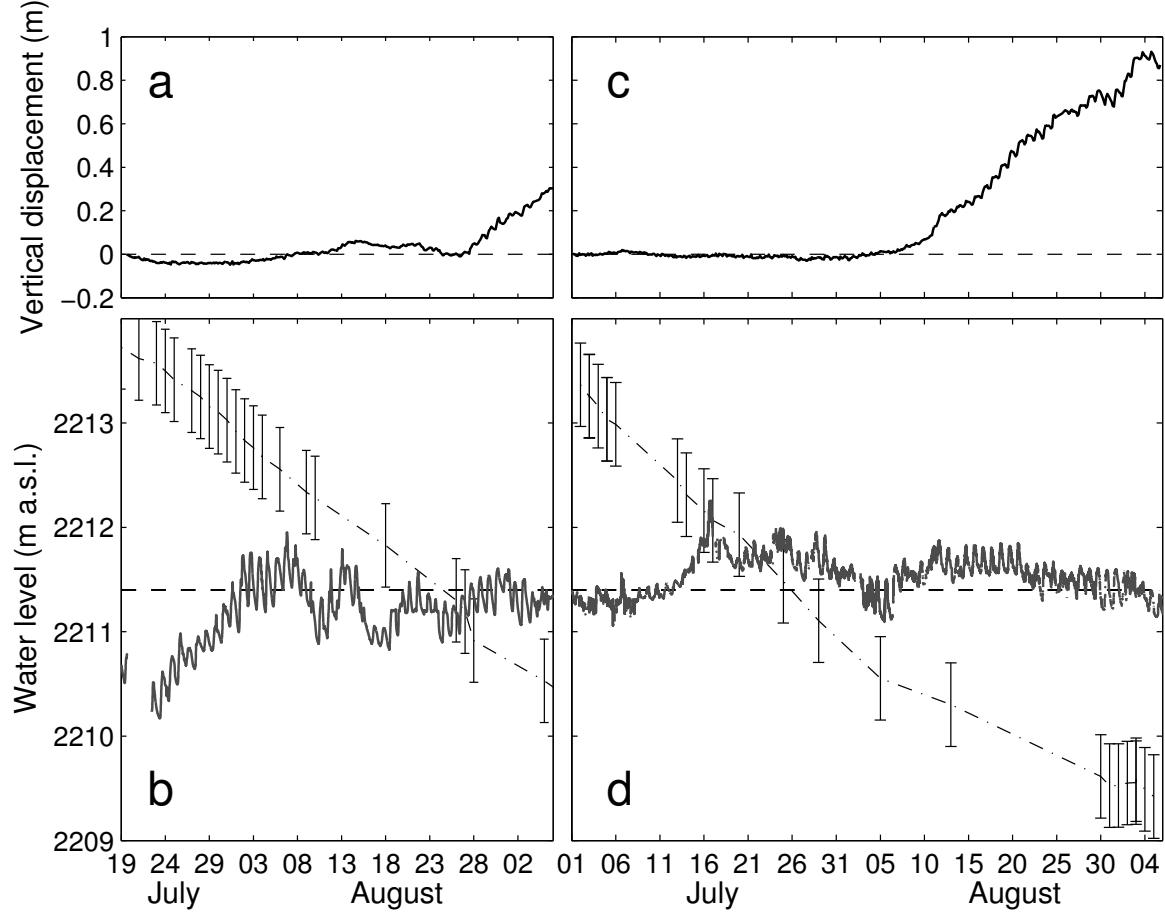


Figure 4.5: (a) Vertical displacement of glacier surface, and (b) borehole water level and flotation level at GPS3 in 2008. (c) Vertical displacement, and (d) borehole water level and flotation level at same borehole in 2009. Error bars in flotation level are 0.3 m. The dashed line in (b) and (d) indicates mean lake level (2211.4 m).

2008, the effective pressure reached zero at the shore of Lake A and in an area including Stake 15 (Fig. 4.6a). Effective pressure was relatively high near GPS3, indicates that the glacier is thinner in that area, and thus the flotation level is higher than other locations. Region which reached flotation extended farther to the southeast in 2009 as a result of glacier thinning (Fig. 4.6b). In the upper reaches, the effective pressure is smaller than that near the lake. Assuming that the thickening rate is constant in time (-3.44 m a^{-1}), the effective pressure will reach zero at the entire area of the glacier terminus after two or three years.

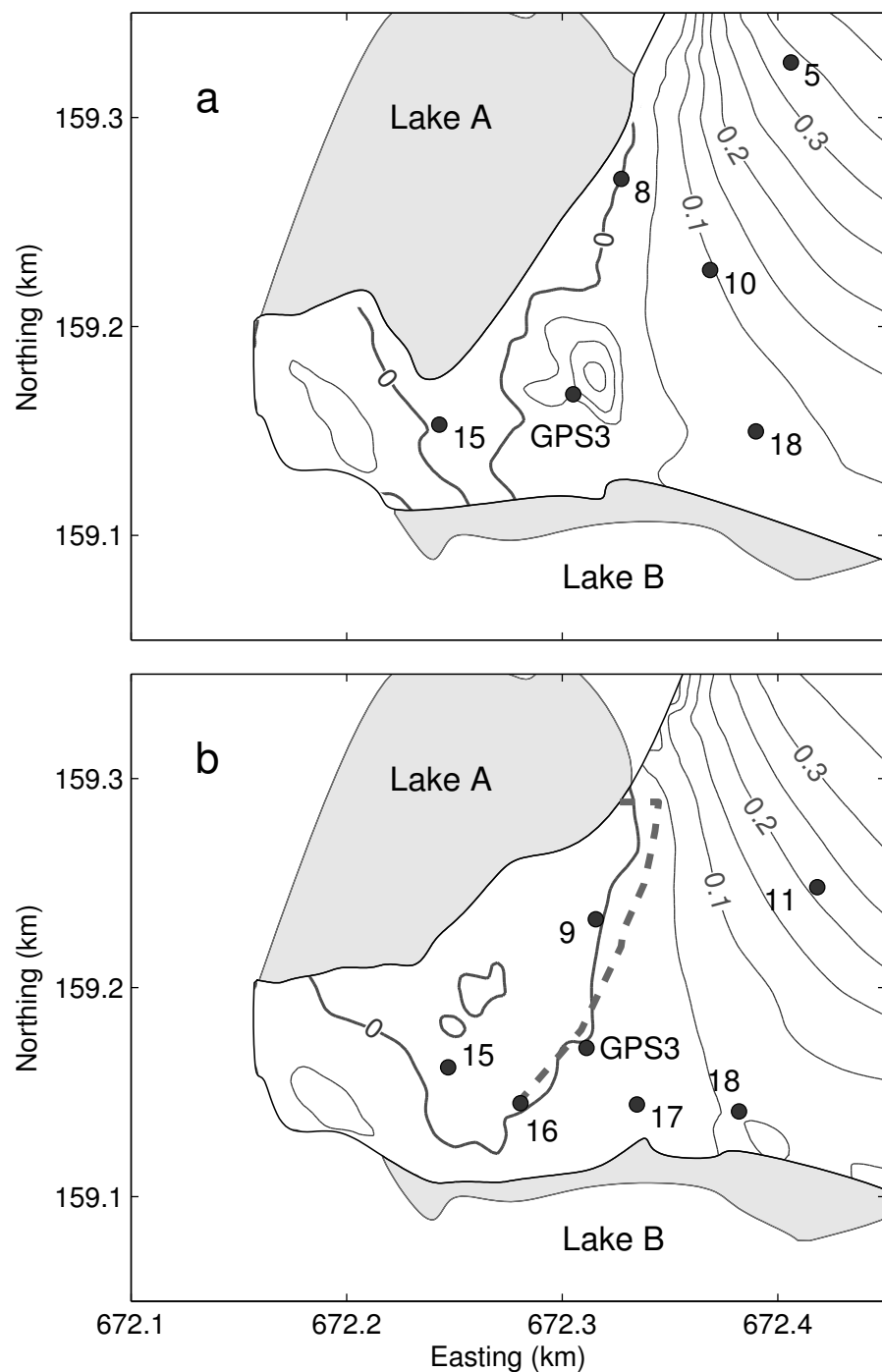


Figure 4.6: The effective pressure in MPa (a) 27–31 July 2008 and (b) 29 July 2009. The contour intervals are 0.05 MPa. The ice overburden pressure was calculated from the surface and bed DEMs constructed in this study. The dashed line in (b) indicates the crevasse described in the text and depicted in Figure 4.7.

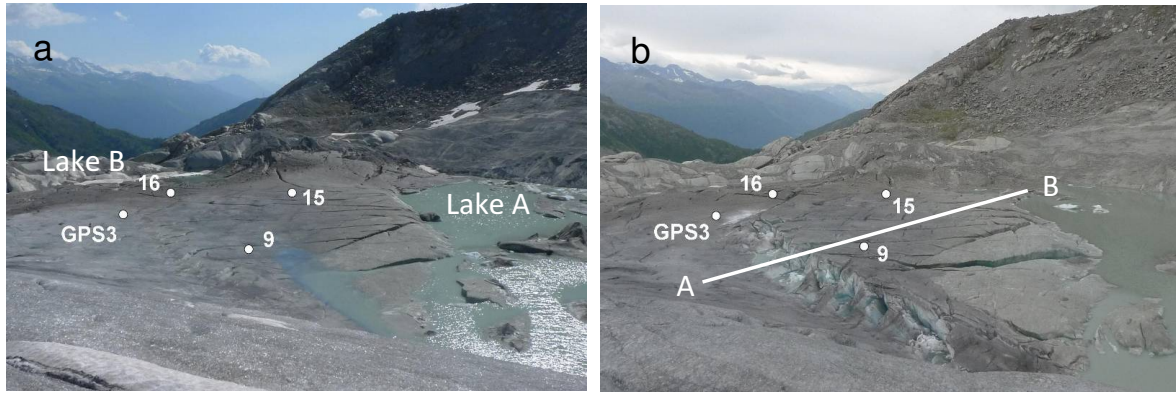


Figure 4.7: Photographs showing the terminus of Rhonegletscher on (a) 29 July 2009 and (b) 3 September 2009. The approximate locations of survey stakes are indicated. Bar depicted between points A and B indicates longitudinal profile shown in Figure 4.9.

4.3.2 Interpretations of the uplifts

As a result of reduction in effective pressure near the lake, a large crevasse began to form along the northern margin of Lake A between Stake 9 and GPS3 and towards Stake 16 (dotted line in Figure 4.6b) in late July 2009; see Figure 4.7a for a photograph of this crevasse. The north-western side of the crevasse had gradually risen relative to the south-eastern side by the beginning of September (Fig. 4.7b). This uplifted area corresponds to the region where the effective pressure was vanishing in 2009. Stakes 9, 15 and 16 located on the ice that moved upwards. GPS3 was on the other side, but only a few meters from the crevasse. Figure 4.8 shows the time series of vertical displacement of ice surface at these four measurement points. To interpret the surface uplift and the crevasse formation, vertical displacement in the three periods (1–16 July, 17 July–19 August and 20 August–5 September) is discussed. Schematic diagrams show mechanisms related with the crevasse formation and uplift in each period (Fig. 4.9).

Upward movement of glacier surface was observed at Stake 9 and 15 when the field measurements were launched on 1 July, suggesting that the ice floated and moved upward (Fig. 4.9a). Predominant uplift (0.1 m^{-1}) occurred at Stake 15, which is the stake nearest the terminus. In this period, the glacier tongue was subjected to a buoyancy force, which was greater than the ice overburden load. Nye (1976) examined the water flow within and under the ice during a glacier outburst flood (*jökulhlaups*) from ice dam in Grímsvötn, Iceland. According to his prediction, when the lake water head reaches the flotation level, a wedge of water would penetrate beneath the ice dam and incrementally jack the ice off its bed. This scenario is the so-called *cantilever effect*. He argued that the ice dam would be subjected to a force which will

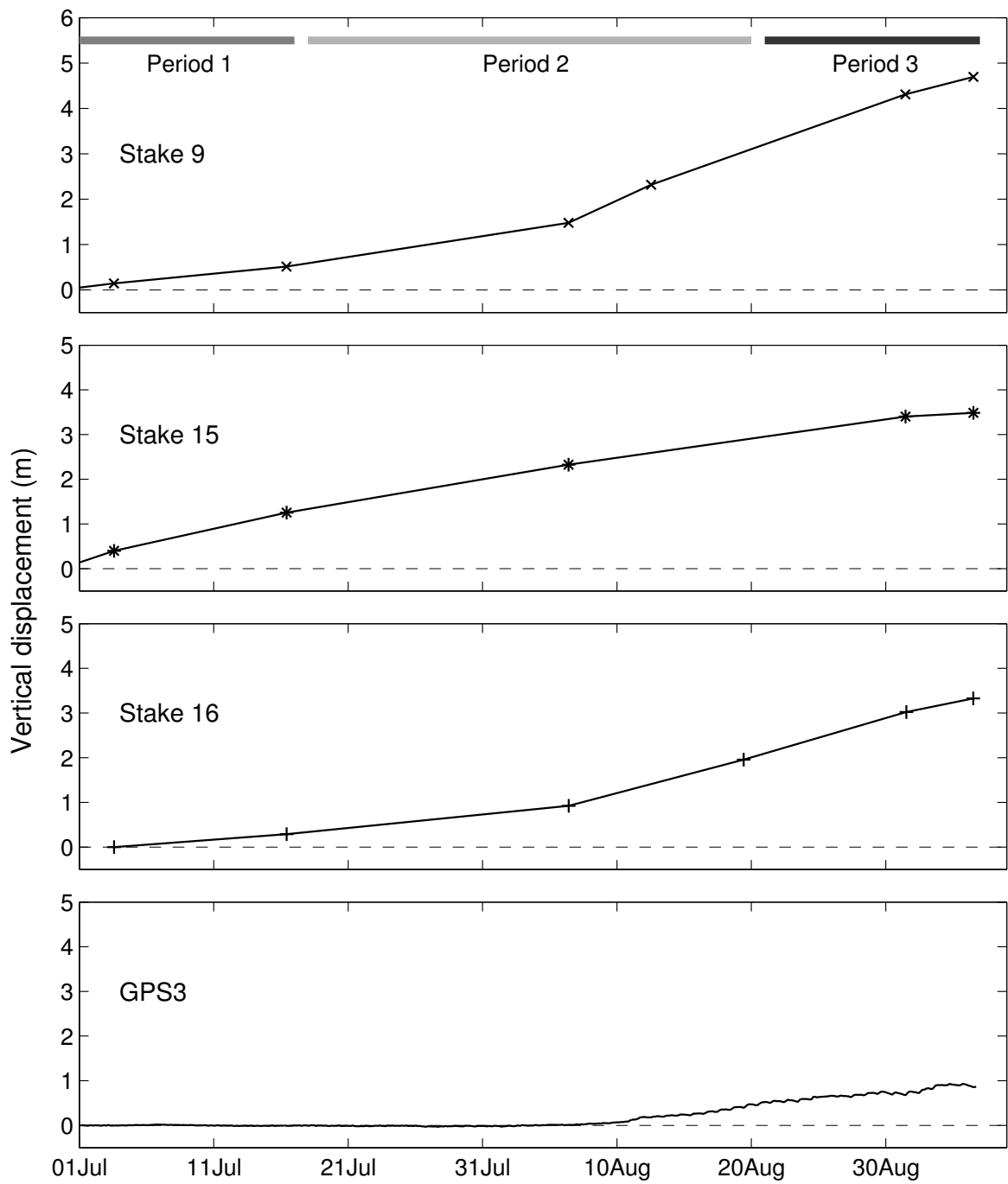


Figure 4.8: Vertical displacement of glacier surface at (a) Stake 9, (b) Stake 15, (c) Stake 16 and (d) GPS3. The horizontal bars indicate the different mechanisms for crevasse formation and uplift depicted in Figure 4.9.

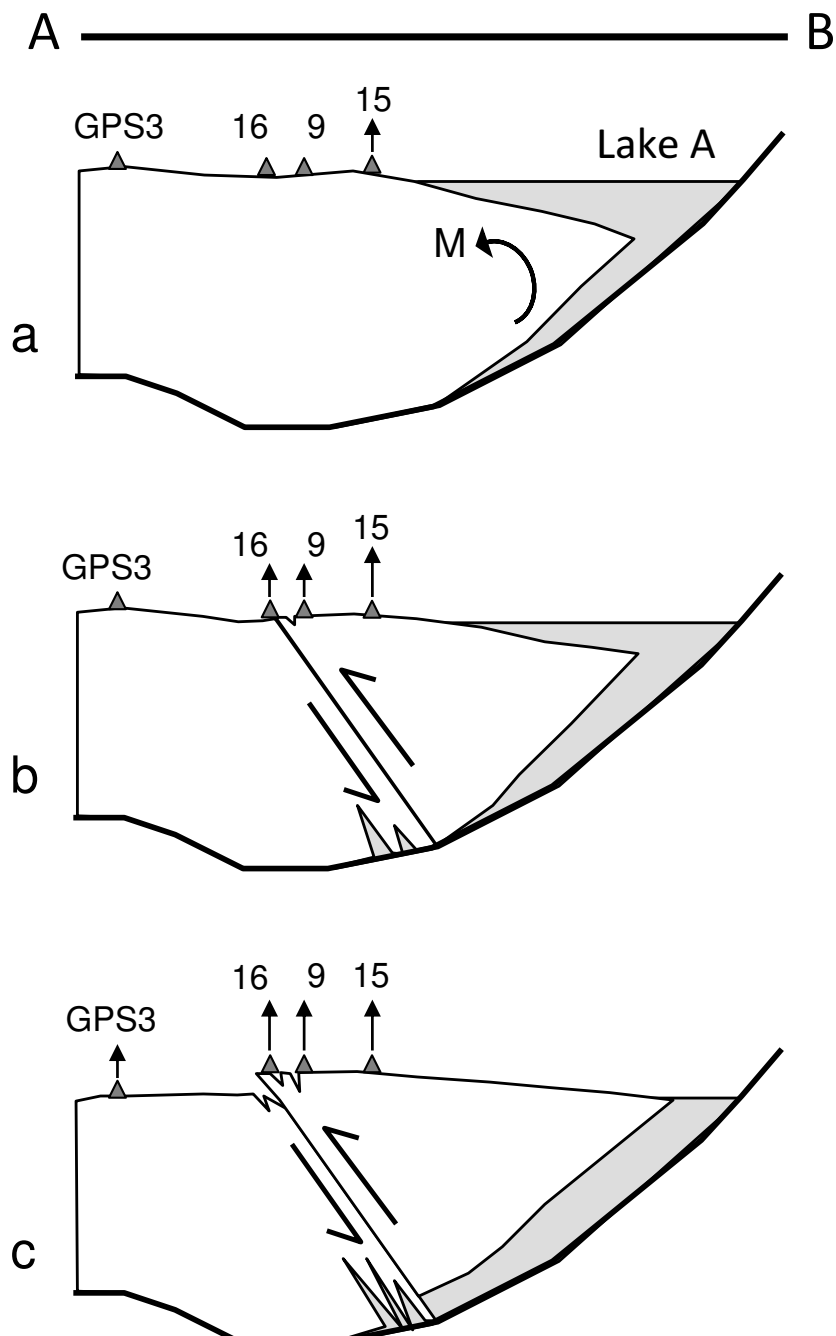


Figure 4.9: Schematic diagrams showing the mechanisms of crevasse formation and surface uplift. The diagrams correspond to the periods for (a) 1–16 July (Period 1 in Figure 4.8), (b) 17 July–19 August (Period 2) and 20 August–5 September (Period 3). The glacier cross section is taken along the line AB in Figure 4.7b.

bend the glacier margin upwards because isostatic adjustment is not instantaneous. Walder and others (2005 and 2006) observed similar uplift event during jökulhlaups from Ice-dammed Hidden Creek Lake, Kennicott Glacier. Warren and others (2001) studied such uplift by field measurements in Glaciar Nef, Chilean Patagonia and interpreted the observation using a buoyant calving model. They suggested that buoyant forces impose a bending moment M (depicted in Figure 4.9a) and tensile stress on the marginal ice, resulting in formation of a crevasse and calving. Before the crevasse formed, tensile stress field occurred at the bottom of glacier due to the bending moment.

According to visual and photograph observation, the crevasse began to form between 29 July and 5 August. This is when vertical displacement increased significantly at Stakes 9 and 16 located along the crevasse (Fig. 4.8). Mean uplift rate at Stakes 9 and 16 are 0.05 and 0.03 m d^{-1} before 6 August, and 0.14 and 0.08 m d^{-1} afterwards. In contrast, increasing rate of displacement at Stake 15 became gradually small. It suggests that the north-western side of the crevasse had gradually risen relative to the south-eastern side. According to the observed stake movement and crevasse patterns, the crevasse formation can be explained by fault formation cutting through the entire ice thickness (Fig. 4.9b). Gagnon and Gammon (1995) experimentally determined tensile strength of ice as about 1 MPa at the pressure-melting point. Vaughan (1993) calculated lower limit of the tensile strength to form a crevasse (about $0.1\text{--}0.2\text{ MPa}$) from the occurrence of crevasse on temperate glaciers. If tensile stress exceeds $0.1\text{--}0.2\text{ MPa}$, the crevasse would begin to form at the glacier bed. To predict a timing of crevasse formation, further discussion is needed with a buoyant calving model.

In the third period, the rates of upward motion at Stakes 9 and 16 are similar, 0.08 and 0.06 m d^{-1} , respectively (Fig. 4.8). At Stake 15, the rate of vertical movement became steady, which is 0.02 m d^{-1} . This value is nearly equal to that observed at GPS3. Total amount of vertical displacement during entire of measurement period is 4.69 m (Stake 9), 3.48 m (Stake 15), 3.32 m (Stake 16) and 0.93 m (GPS3). The glacier surface was 3.8 m higher in the northwestern side of the crevasse than the southwestern side (Fig. 4.9c).

4.4 Future evolution of Rhonegletscher

The formation of crevasse and huge uplift were observed in the field measurements during the ablation season of 2009. It is expected that the upward movement of glacier would be observed in a larger area if ice thinning continues in the future. Our field measurements were completed in early September 2009. After the measurements, the study site has been observed by operating an automatic digital camera one a day by Section of Glaciology, VAW, ETH Zurich (<http://people.ee.ethz.ch/~glacier/acam.html>). Figure 4.10 shows the photographs of Rhonegletscher tongue taken on 11 October 2009 and 11 October 2010. In October 2009, the position of glacier terminus was nearly equal to that observed in late July by GPS survey (Fig. 4.10a). However, the terminus disintegrated and the marginal ice detached from the



Figure 4.10: Photographs showing the terminus of Rhonegletscher on (a) 11 October 2009 and (b) 11 October 2010. Dashed line indicates the approximate area where the effective pressure was less than zero in 2009 as shown in Figure 4.6b. These photographs were taken by Section of Glaciology, VAW, ETH Zurich (<http://people.ee.ethz.ch/glacier/acam.html>).

glacier body in October 2010 (Fig. 4.10b). The disintegrated area corresponds roughly to the uplifted region in 2009. Accordingly, the rapid terminus retreat occurred only 5 years after the formation of the proglacial lake, as observed in Triftgletscher, Switzerland (Müller, 2004).

Figure 4.11 shows processes of rapid glacier retreat after the formation of proglacial lake revealed by this study. Lake formation in the terminus triggers increase in subglacial water pressure. On the other hand, ice overburden pressure decrease as the ice thins as a result of surface ablation. These two processes reduces the effective pressure, which causes the acceleration of ice flow at the terminus. Speed up of glacier terminus changes in horizontal flow regime from compression to extension. Tensile strain regime causes the thinning of ice. Benn and others (2007) suggested positive feedbacks between longitudinal stretching and ice thinning: longitudinal stretching leads to ice thinning and decrease in effective pressure, which will lead to further flow acceleration and longitudinal stretching. It is suggested that these positive feedbacks was activated and the ice thinning accelerated in the terminal part of Rhonegletscher after the formation of Lake B. When subglacial water pressure exceeds the ice overburden pressure, surface uplift and the formation of crevasses occurred, resulting in the integration of the glacier terminus as observed in 2010. According to the change in spatial distribution of effective pressure, the eastern side of glacier terminus in front of Lake A may float and disintegrate over the next few years if the glacier continues to thin.

The bed elevation map obtained in this study provides important information for predicting future expansion of the proglacial lake. We predict that the lake will expand nearly 1 km

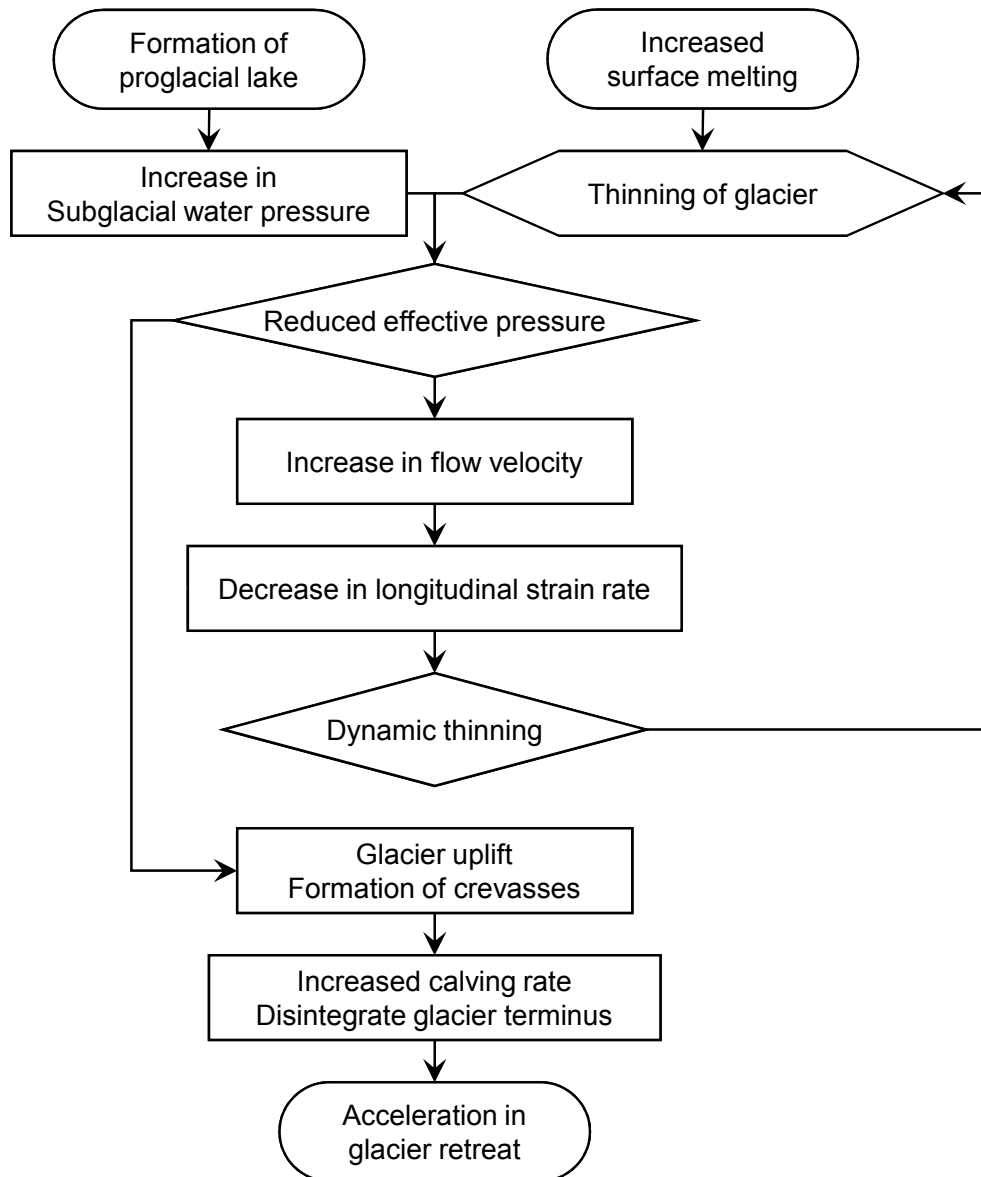


Figure 4.11: Flow diagram of influence of proglacial lake formation on glacier retreat.

from the current terminus to the area bounded by the dotted line in Figure 3.8a as the glacier retreats. The maximum depth of the lake upon reaching this size will be approximately 50 m. At a constant thinning rate of -3.4 m a^{-1} , the lake will continue to expand approximately 600 m up-glacier and reach the location of GPS1 in 2034. The future evolution of Rhonegletscher has been predicted by numerical modeling based on the ice-radar data (Sugiyama and others, 2007). Because the bedrock depression reported in the ice-radar data does not exist, ice flux into the terminal part is less than expected. Thus, the retreat rate of the glacier would be greater than this previous prediction. Sugiyama and others (2008a) suggested that the lake will expand to the location of GPS1 in 2040, which was based on the thinning rate of -2.8 m a^{-1} . This prediction is 6 years later than that in this study. Accordingly, increase in thinning rate due to extending flow regime and increase in summer ablation will cause more rapid glacier retreat than expected by previous studies. Mass-balance changes in Swiss glaciers are probably related to the increase in the thinning rate. Huss and others (2008) computed the seasonal mass balance of four glaciers, including Rhonegletscher, for the period 1865–2006. According to their results, the rate of mass loss progressively increased after a short period of mass gain from 1974 to 1981. The period 1998–2006 was characterized by strongly negative mass balance due to high summer ablation in all four glaciers. To carry out more accurate prediction for glacier retreat, numerical investigations using a glacier evolution model incorporating DEMs of surface and bedrock, and processes of acceleration and disintegration of glacier terminus revealed in this study are required.

Proglacial lakes in many alpine glaciers pose a sudden outburst of the lake water, the so-called Glacial Lake Outburst Flood (GLOF) in Himalaya (e.g. Bolch and others, 2008; Fujita and others, 2009), Switzerland (e.g. Huggel and others, 2003; 2004) and other countries (e.g. Clague and Evans, 2000). In Rhonegletscher, GLOF is not likely as it is dammed by the bedrock bump. However, one of the possibilities of GLOF is due to ice avalanches. Ice avalanches are caused by frontal ice brocks failure, ice slab failure and ice-bedrock failure (Richardson and Reynolds, 2000). Waves generated by ice avalanches can overtop the damming bump, and cause a significant hazard in areas where human activities impinge upon the upper glaciated valley catchments. Changes in effective pressure at the western side of upglacier area between Stakes 5 and 10 is more steady than that at the terminus (Fig. 4.6a and b). It is implied that the glacier terminus at this area would be remain over the next few years. The surface slope at this area is relatively steep (9°). Because of the steep slope, a crevasse has formed from the western margin toward the center part (Fig. 4.10). If the marginal part of the ice detaches from this crevasse and fall into the lake, large waves toward the damming bump, resulting in occurrence of outburst floods.

4.5 Summary

Comparisons of our data to the study analyzed the velocity in 1999–2000 and 2005–2006 (Nishimura, 2008) revealed change in the flow velocities after the lake formation. The flow velocity approximately tripled from 2006 to 2007 at the glacier terminus. The effective pressure reached zero at the glacier terminus in 2008 and 2009. Additionally, horizontal velocities were greater than 20 m a^{-1} in the region where the ice thickness was only about 20 m. Thus, most of the flow at the terminus was due to basal ice motion. Flow velocity decreased after the lake formation in upper reaches. This velocity change is due to the thinning of ice.

The longitudinal strain rate revealed the ice flow regime under the influence of proglacial lake formation. The longitudinal strain rate at the glacier terminus changed from compressive to tensile after the lake formation. Calculated spatial distribution of horizontal strain rate shows that the horizontal flow regime near the terminus was tensile in the longitudinal direction. This finding suggests that increase in ice thinning observed in the last decade has been caused by both the extending flow regime and negative mass balance.

A huge uplift at the terminus was observed when the borehole water level exceeded the flotation level of ice thickness as a result of ice thinning. Analysis of the effective pressure confirms that water pressure exceeded the ice overburden pressure along the shore of Lake A in 2008. The region of excess water pressure extends even farther in the terminal area in 2009 as a result of ice thinning. The uplift is related to the formation of a crevasse. The temporal variations in vertical stake movements around the crevasse revealed the mechanisms of crevasse formation. Before the crevasse formed, surface uplift at the shore of Lake A occurred because a water wedge penetrated beneath the ice dam. The glacier margin decoupled from the bed by this process. The crevasse has formed due to movement along steeply dipping faults that dips towards the lake and cut through the entire ice thickness.

After the huge uplift and the formation of crevasse were occurred, disintegration of glacier terminus was observed in uplifted area. The entire glacier terminus will float and disintegrate over the next few years. The processes of glacier retreat caused by proglacial lake formation were observed particularly in this study. At the elevation range of 2250–2350 m, the glacier is thinning at a progressively increasing rate. Assuming that the thinning rate of -3.4 m a^{-1} observed in 2008–2009 is sustained, the glacier will retreat approximately 600 m and the lake will expand to its maximum size by 2034. The possibility of GLOF in Rhonegletscher is not likely as it is dammed by the bedrock bump. However, ice avalanches generate large waves and pose outburst floods after the glacier terminus will retreat up to steep part located upglacier from the western side of lake A.

Chapter 5

Numerical model of Rhonegletscher

In this chapter, a three-dimensional (3D) glacier flow model is developed to evaluate the effect of proglacial lake formation on the flow field. The model computes flow speed, stress and strain fields under prescribed basal sliding conditions. In the first section, equations to be solved in the model, mesh generation, boundary conditions and model calibration are described. In the second part, conducted experiments and results are presented.

5.1 Field equations

5.1.1 Stokes equations

The numerical flow model developed in this study is based on Stokes equations under steady state condition. The total mass of a material body is the integral of the density over its volume. For an incompressible medium, such as ice, the density ρ remains constant during motion. The equation of mass conservation can be written as

$$\nabla \cdot \mathbf{v} = v_{i,i} = 0, \quad (5.1)$$

where $v_{i,i}$ are the derivatives of each component of the velocity in its direction (Helbing, 2006). Momentum balance equation is,

$$\sigma_{ij,i} + \rho b_i = 0, \quad (5.2)$$

where $\mathbf{b} = (b_1, b_2, b_3)$ is the gravitational force vector and

$$\sigma = \begin{pmatrix} \sigma_{11} & \sigma_{12} & \sigma_{13} \\ \sigma_{21} & \sigma_{22} & \sigma_{23} \\ \sigma_{31} & \sigma_{32} & \sigma_{33} \end{pmatrix} \quad (5.3)$$

is the stress tensor. From the balance of the angular momentum, which equals the rate of change of the angular momentum with the vector sum of all moments of external forces, follows that the stress tensor σ is symmetric (Hutter, 1983)

$$\sigma_{ij} = \sigma_{ji}. \quad (5.4)$$

5.1.2 Constitutive equations

Solutions of Equation (5.1) and (5.2) require a constitutive equation which prescribes the relationship between velocity changes (deformation) and resulting stresses. In the case of an incompressible isotropic material, the strain rates $\dot{\varepsilon}_{ij}$ are related to the deviatoric stresses $\sigma_{ij}^{(d)}$ with some scalar function f

$$\dot{\varepsilon}_{ij} = f\sigma_{ij}^{(d)} \quad (5.5)$$

the strain rates describe the spatial changes in the velocity field and are defined as

$$\dot{\varepsilon}_{ij}^{(d)} = \frac{1}{2}(v_{i,j} + v_{j,i}). \quad (5.6)$$

Established through numerous experiments (e.g. Glen, 1955) and widely tested in flow modeling studies (e.g. Pattyn, 2003), the constitutive equation of ice seems to be well approximated by

$$f = A(T')\tau^{n-1}, \quad (5.7)$$

where T' is a temperature relative to pressure melting, and τ is the effective stress defined as

$$\tau = \sqrt{\frac{1}{2}\sigma_{ij}^{(d)}\sigma_{ji}^{(d)}}. \quad (5.8)$$

The constitutive relation of ice is given by Equations (5.5) and (5.8) and is defined as

$$\dot{\varepsilon}_{ij} = A(T')\tau^{n-1}\sigma_{ij}^{(d)}. \quad (5.9)$$

The rate factor A and the flow-law exponent n are material parameters. The homological temperature T' of temperate ice constantly equals zero, because the ice is always at the pressure melting point. Thus, Equation (5.9) can be modified as

$$\dot{\varepsilon}_{ij} = A\tau^{n-1}\sigma_{ij}^{(d)}. \quad (5.10)$$

and so called Glen's flow law (Glen, 1952, 1955; Nye, 1953). The value of $n = 3$ is commonly accepted, and the rate factor is assumed to be constant for the temperate ice condition. When the flow model is calculated by implementation of Equation (5.10) into MSC.MARC, the analysis type of *rigid plastic flow* is used. Each component of the deviatoric stress tensor is assumed to be proportional to the corresponding component of the strain rate tensor and a viscosity η of ice. This relationship is defined as

$$\sigma_{ij}^{(d)} = 2\eta\dot{\varepsilon}_{ij}. \quad (5.11)$$

5.2 Finite element mesh

To calculate Equations (5.1), (5.2) and (5.10), we used a commercial finite element software package MSC.MARC. MSC.MARC has been used for some flow models of temperate valley glacier in Switzerland. Gudmundsson (1999) constructed the three-dimensional flow model of the confluence area of Unteraargletscher based on the observational data for surface velocity and ice deformation (Gudmundsson, 1997; Gudmundsson and others, 1997). Helbing (2006) discussed flow laws by using the observational data and numerical model of Unteraargletscher. Riesen and others (2010) discussed the influence of a glacier-dammed marginal lake drainage on glacier dynamics in Gornergletscher. Raymond and Gudmundsson (2005) applied the model to ice sheet and discussed the influence of basal disturbances on the steady state surface topography and on surface velocities. In this study, 3D finite element mesh of Rhonegletscher tongue has been constructed.

The finite element mesh was constructed from following inputs:

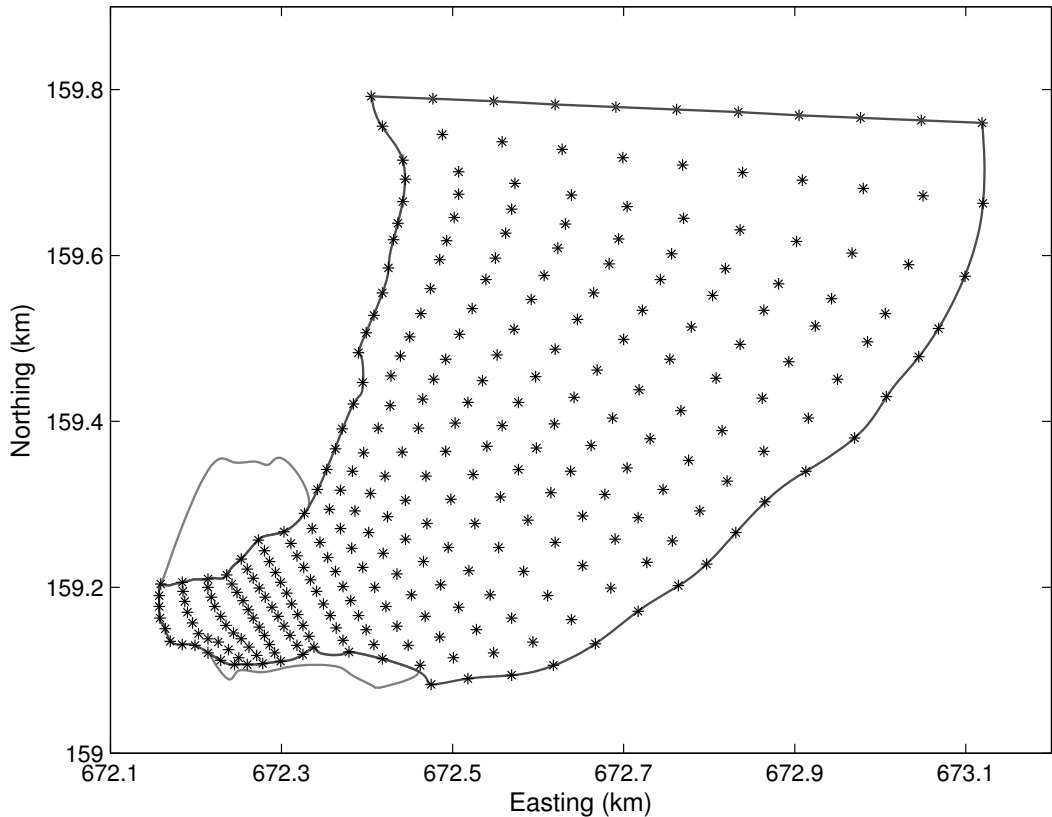


Figure 5.1: Surface nodes used for finite element mesh generation.

1. Digital glacier surface elevation model
2. Bed elevation model
3. Coordinates of glacier margin
4. Coordinates of mesh node on the surface

DEMs of surface and bed were constructed by field measurements described in Section 3.2. Note that the elevation model and glacier margin in 2009 was used. In Figure 5.1, nodes of the constructed mesh on the surface are depicted. The spacing between the nodes depends on the glacier width. From the terminus to the upper boundary cross section, 26 longitudinal profiles approximately normal to the centre flow line have been positioned. Therefore, there are 286 nodes on the upper surface of the model. The vertical nodal positions z_i were determined as

$$z_i = z_b + a_i(z_s - z_b) \quad (5.12)$$

where $a_i \in [0, 0.04, 0.16, 0.36, 0.64, 1]$ and z_s , z_b are surface and bed elevation, respectively. Equation (5.12) produced 5 layers (6 nodes) of hexahedral, eight-node brick elements from the surface to the ice-bedrock interface. The regarding vertical node columns in the margin have a height of five meters. An additional nodal layer one meter below the ice boundary provided the sixth element layer, which needed for introducing basal sliding (see Section 5.3.1). The final mesh consists of 1500 elements and 2002 nodes (Fig. 5.2).

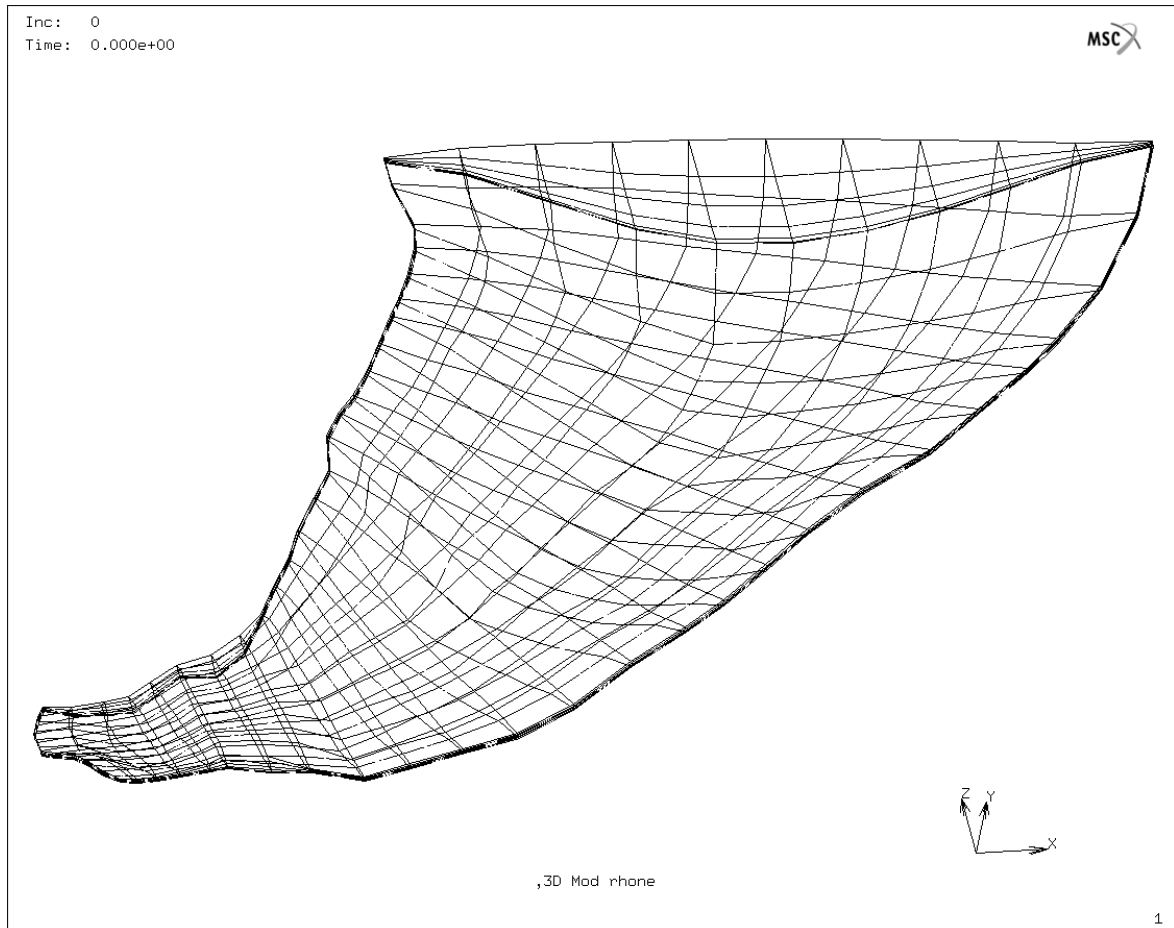


Figure 5.2: Oblique view of the three-dimensional finite element mesh of Rhonegletscher tongue. Only lines connectivity nodes on the node surface are drawn. The glacier terminus is situated at the lower left and the up-glacier cross section is in the upper right.

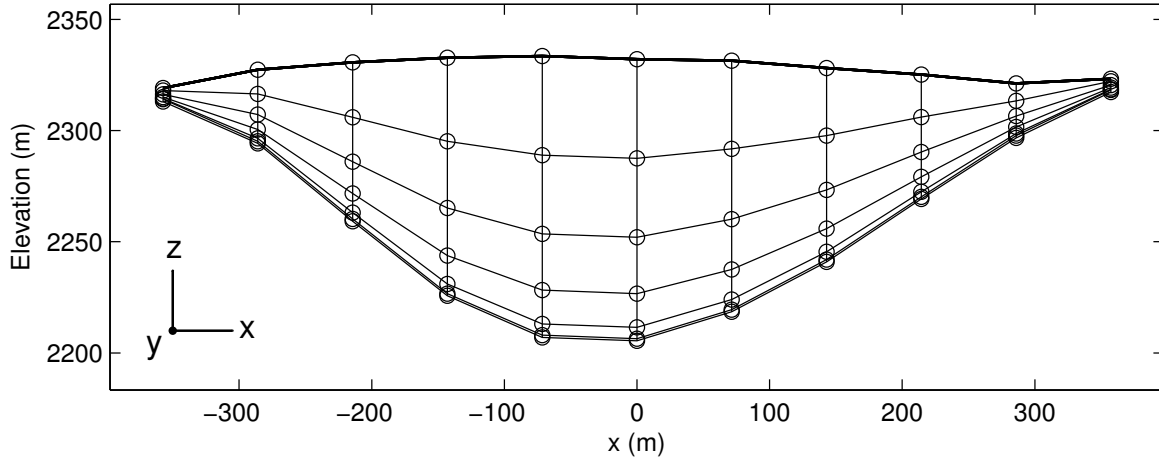


Figure 5.3: A finite element mesh on the upper boundary of the model.

5.3 Boundary conditions

The model has four surfaces on which appropriate boundary conditions have to be given:

- Glacier surface
- Bed and margin
- Transverse cross-section of up-glacier boundary

For the glacier surface, no accumulation or ablation is considered. The model calculations are snapshots of a velocity distribution and the evolution of glacier surface will not be considered.

To the bottom layer of nodes corresponding to the bedrock surface, non-displacement condition is applied. Along the eastern and western margin except for the boundary to the lake, a fixed boundary condition is given as well.

5.3.1 Basal sliding

The basal motion of the glacier was simulated by introducing a thin deformable sub-basal layer into the finite element model (Fig. 5.4). As the bottom of the elements is fixed, the sub-basal layer deforms by basal shear stress. The strain rate for the element is

$$\dot{\varepsilon}_{xz} = \frac{1}{2} \frac{\partial u}{\partial z} \quad (5.13)$$

From Equations (5.11) and (5.13), we can express the strain rate in terms of basal shear stress τ_b ,

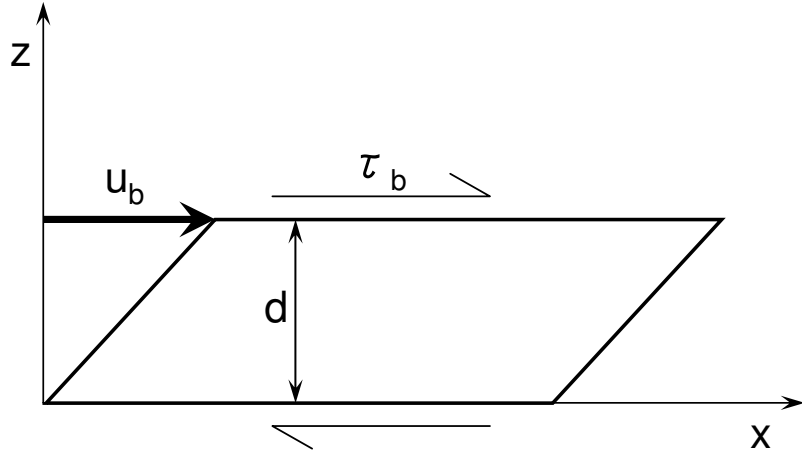


Figure 5.4: Scheme of simple shearing of one element. The upper side of the element corresponds to the ice-bed interface with basal sliding by u_b . The element thickness d and the shear stress τ_b (deviatoric stress component $\sigma_{xz}^{(d)}$) are depicted.

$$\frac{1}{2} \frac{\partial u}{\partial z} = \frac{1}{2\eta} \tau_b \quad (5.14)$$

Integration of Equation (5.14) gives the basal sliding velocity u_b

$$u_b = \frac{\Delta z}{\eta} \tau_b = \frac{d}{\eta} \tau_b \equiv C \tau_b \quad (5.15)$$

where d is the element thickness, η is a viscosity of the sub-basal layer. Basal flow velocity is introduced by prescribing the basal flow coefficient C . In MSC.MARC, the value of C could be given to each element, which allows spatial variability in the basal slipperiness.

5.3.2 2D cross-section flow models

In our model, we focus on the terminal part of Rhonegletscher. We have to describe realistic conditions on the open transverse section of up-glacier. To the open glacier cross-section, nodal velocity distributions were applied, which were derived separately from a two-dimensional (2D) cross-section flow model. Figure 5.3 depicts upper boundary cross section. The input parameters for 2D flow model are surface slope α , rate factor A and the coefficient C for the basal sliding law. We define the value of α by estimating a mean surface slope between BH707 and BH704 near the cross-section, yielding a value of $\alpha = 9.94^\circ$ (Fig. 5.5). The value of $A = 75 \text{ MPa}^{-3} \text{ a}^{-1}$ was used. This value was proposed for temperate glaciers based on a three-dimensional numerical modeling and field data in Unteraargletscher (Gudmundsson, 1999). The basal sliding coefficient C at the upper boundary was given so that the 2D flow model reproduces the summer flow velocity measured at stake 0608 by VAW, ETH Zurich (Turi, 2009) (Fig. 5.4).

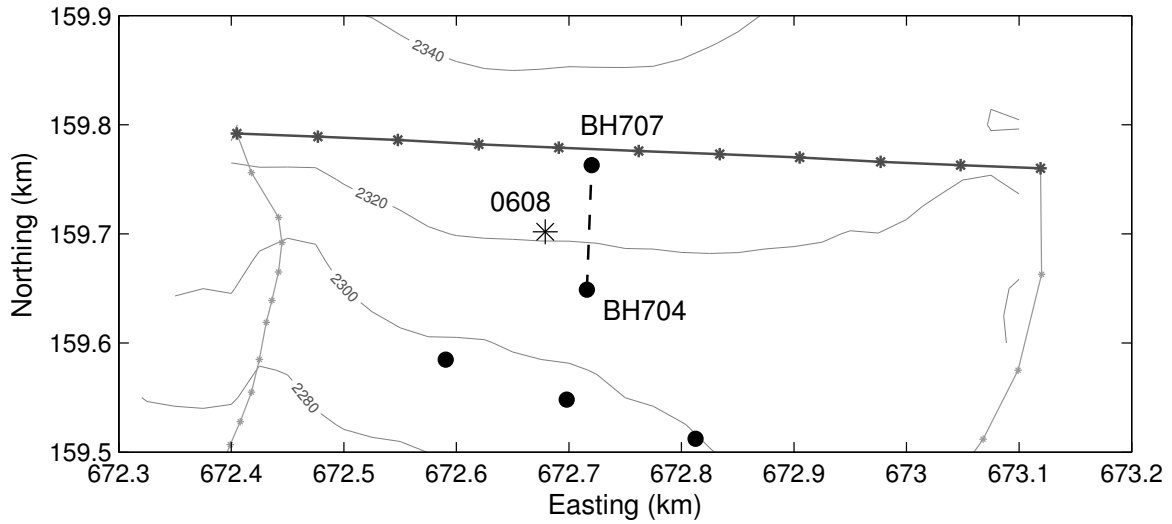


Figure 5.5: Plane view of theodolite stake position [0608] and the upper boundary of the model. The slope at the boundary was calculated from the surveys at two boreholes, BH704 and BH707.

First, the basal sliding coefficient was set to zero (no sliding). Figure 5.6 shows the result. The computed surface flow velocities are too small compared to the measured summer flow velocity at the stake position. Second, the basal sliding coefficient was set to reproduce the measured summer flow velocity. The result is depicted in Figure 5.7. The result shows the basal sliding is about 74% of total flow speed. For computation of the three-dimensional model, calculated flow velocity with basal sliding will be used.

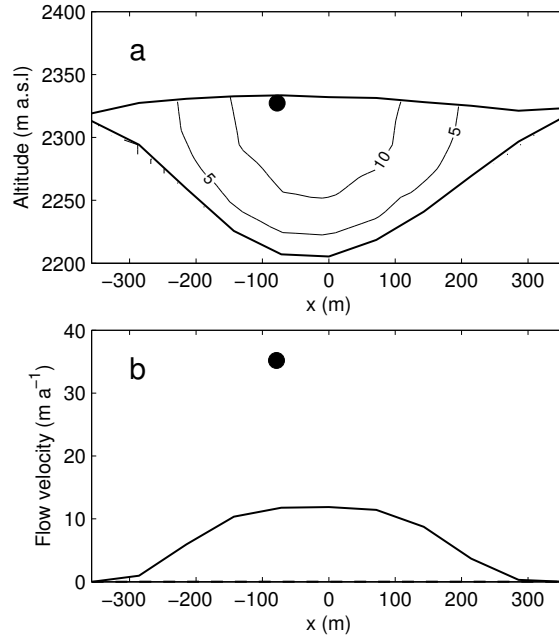


Figure 5.6: Computation of flow velocities in the upper boundary for $A = 75 \text{ MPa}^{-1} \text{ a}^{-1}$ and $C = 0$ with fixed slope of $\tan \alpha = 0.1752$. (a) Contour plots indicate the calculated flow velocities. Black dot indicates measured summer flow velocity. (b) Computed surface flow velocity (solid) and basal velocity profiles (dash).

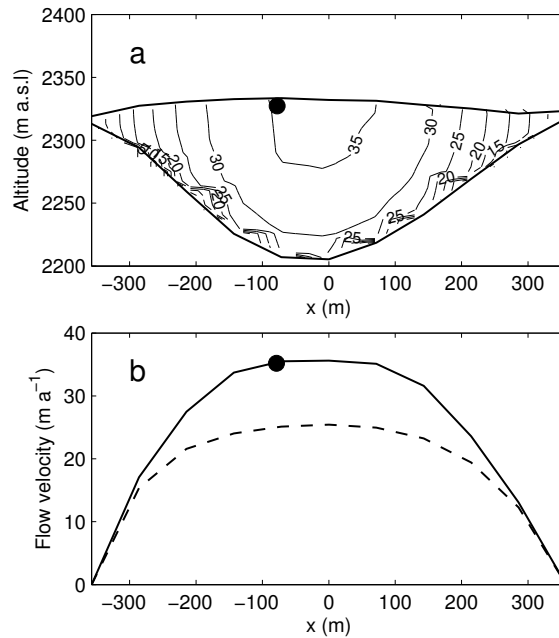


Figure 5.7: Computation of flow velocities in the upper boundary for basal sliding ($C = 97$). (a) Contour plots indicate the calculated flow velocities. Black dot indicates measured summer flow velocity. (b) Profiles of computed surface flow velocity (solid) and basal velocities (dash).

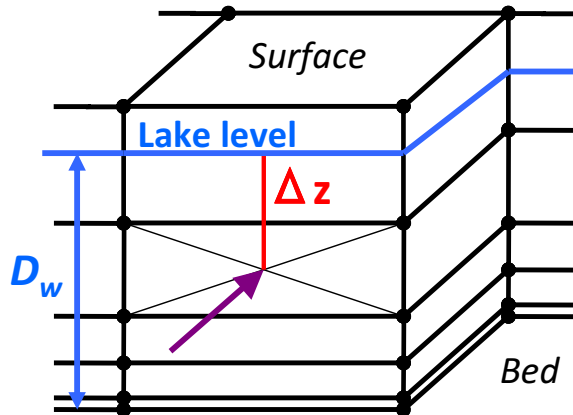


Figure 5.8: Sketch of the model boundary against to the lake. Water pressure is calculated according to the mean elevation of side surface of element (Δz) and then loaded to the element.

5.3.3 Lake water pressure

Riesen and others (2010) considered the influence of lake water pressure on the ice dynamics. They introduced the lake presence as pressure loads onto the elements being underwater. In our study, lake water contacts side surface of elements. In Figure 5.8, a schematic diagram of the boundary of ice and lake water is given. A subroutine calculates the mean water pressure on the side of the elements whose mean elevation is below the lake water. Elements in contact with the lake water has to be defined in advance. Figure 5.9a shows the elements on which lake-water pressure was applied. The lake pressure was uniformly applied on the surface of the element. The pressure load was resolved in x and y directions to introduce it into MARC (Fig. 5.10).

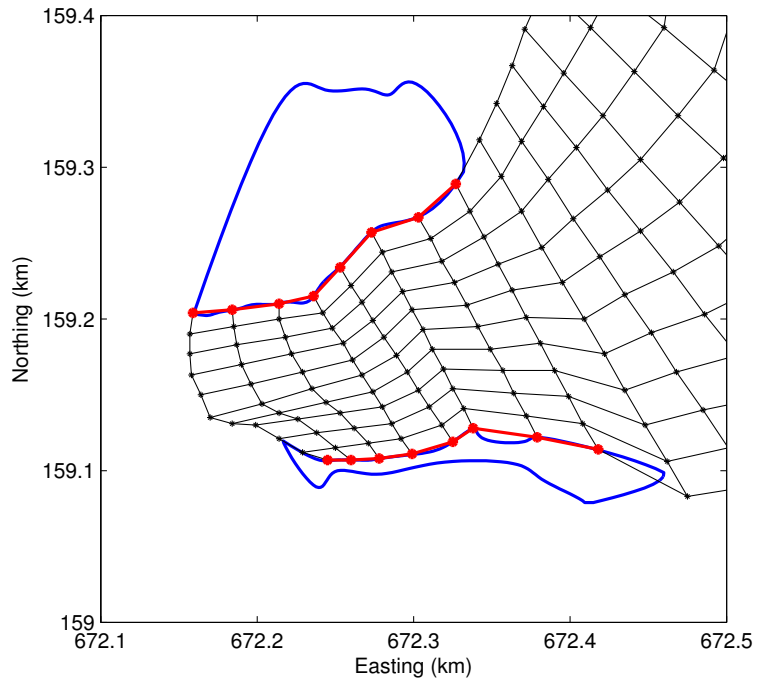


Figure 5.9: Model boundaries on which lake water pressure was applied (red). Blue line indicates the lake margins.

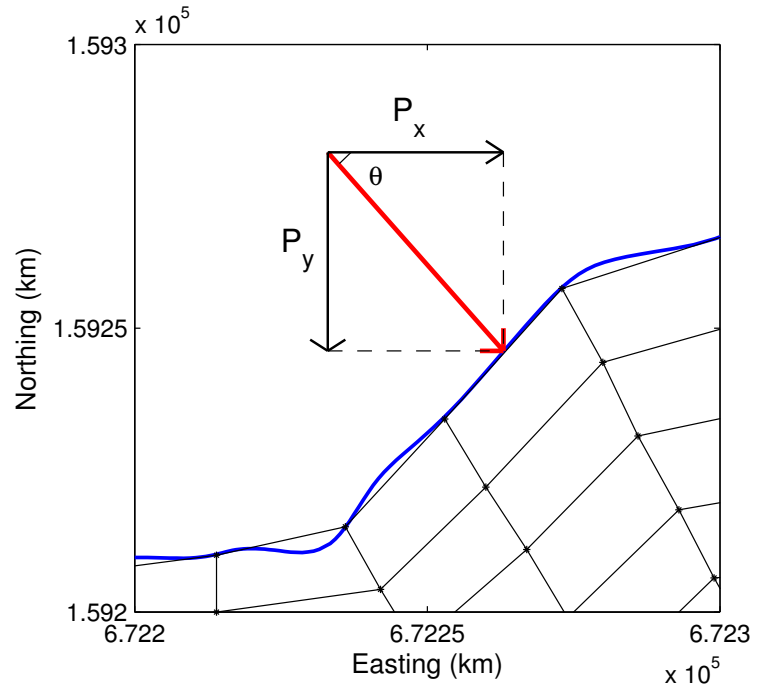


Figure 5.10: Vector components of lake pressure load. P_x and P_y indicate x and y components of the load. Blue line indicates the lake margins.

5.4 Sensitivity tests

To test the sensitivity of applied boundary conditions to the three-dimensional model, easy sensitivity tests were done.

5.4.1 Test 1

In the Test 1, different experiments have been conducted to investigate the sensitivity of the model on the upglacier boundary condition listed in Table 5.1.

1. Comparison of the surface flow fields calculated by 3D flow model with a non-sliding condition for application of 80, 100 and 120% of the upper boundary flow velocities.
2. Comparison of the flow fields with a uniform sliding condition for 80, 100 and 120% of calculated velocities by 2D flow model.

The velocity fields for non-sliding condition was computed with MSC.MARC. This sensitivity test was applied the velocities for upper boundary cross-section calculated from 2D flow model. The 3D model runs for 80, 100 and 120% of calibrated initial velocities u_i for upper boundary condition (Experiments 1–3 in Table 5.1). The calculated flow fields for three initial boundary conditions were plotted at upper boundary cross-section and at the interpolated five transverse cross-sections (Fig. 5.11a). Figure 5.11b shows the interpolated velocities for the locations of GPS measurement in 2009.

The sensitivity test for a uniform sliding condition was conducted. The initial condition of the velocity at the upper boundary cross-section was applied as well as in Test 1 (Experiments 4–6 in Table 5.1). The results are plotted in Figure 5.12.

Table 5.1: *Summary of conducted sensitivity tests in Test 1.*

Experiment No.	C ($m\ a^{-1} MPa^{-1}$)	Upper boundary condition
Experiment 1	= 0	$u_i \times 0.8$
Experiment 2	= 0	$u_i \times 1.0$
Experiment 3	= 0	$u_i \times 1.2$
Experiment 4	$\neq 0$	$u_i \times 0.8$
Experiment 5	$\neq 0$	$u_i \times 1.0$
Experiment 6	$\neq 0$	$u_i \times 1.2$

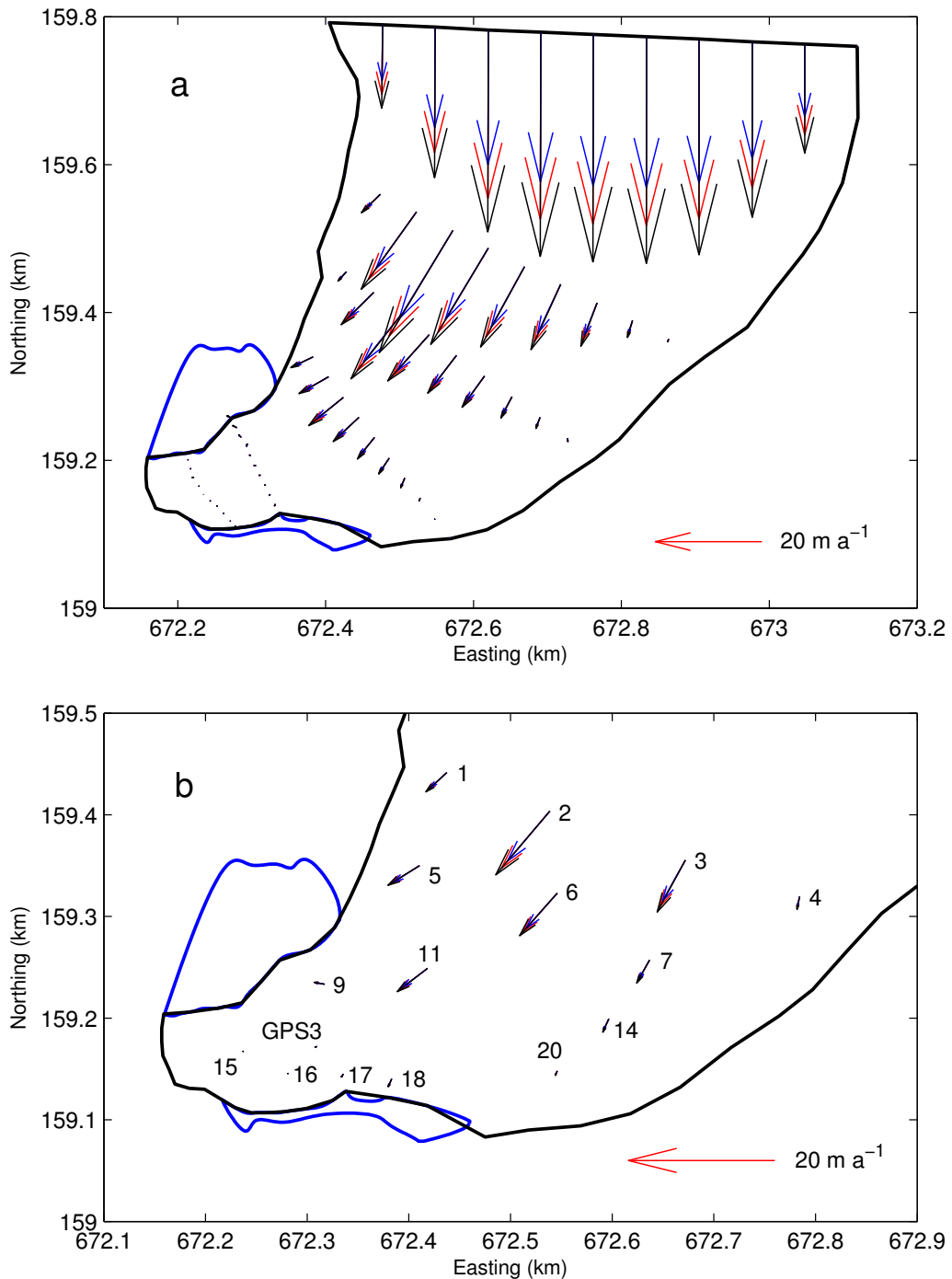


Figure 5.11: Computed surface flow vectors without sliding in Test 1. (a) Surface velocities: Red vectors mark 100% of initial applied velocities (Experiment 2), whereas blue and black vectors correspond to Experiments 1 and 3, respectively. (b) Interpolated surface velocities at the locations of GPS measurement in 2009.

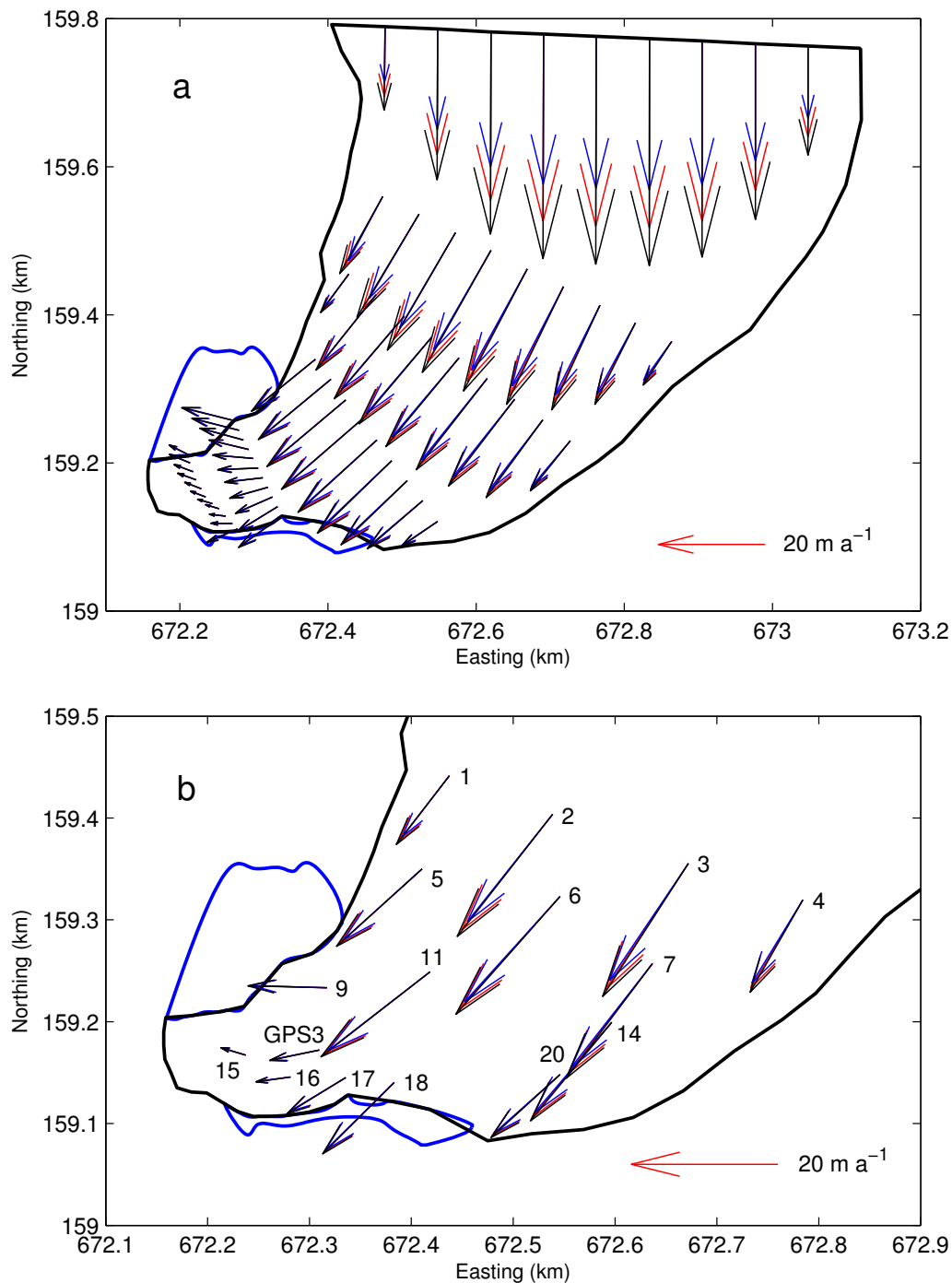


Figure 5.12: Computed surface flow vectors with basal sliding in Test 2. (a) Surface velocities: Red vectors mark 100% of initial applied velocities (Experiment 5), whereas blue and black vectors correspond to Experiments 1 and 3, respectively. (b) Interpolated surface velocities at the locations of GPS measurement in 2009.

Test results

In the non-sliding conditions, the difference in velocities for each experiments is able to see clearly on the boundary faces. As for the upper boundary cross-section, the results shows the exact same flow regime, only the magnitude of flow vectors is affected. This is actually true for all vectors, regardless of position on the nodal points or on the interpolated stake positions. Despite increasing flow speed, flow direction of all vectors have little change (Figs 5.10b and 5.11b). The flow speeds do not differ in the terminal area, while flow speed is increased in the upper area (Fig. 5.11b).

5.4.2 Test 2

The finite-element mesh was consisted by 1500 elements as described in section 5.2. The smallest surface elements are situated near the terminus, having approximate dimensions of 20×20 m surface area and about 10 m thickness. The thickness of the elements decreases gradually towards the bottom (Eq. 5.12) because the vertical velocity profile is more accurate at the bed, where most ice deformation occurs. The constructed mesh is rather coarse compared to the dimensions of the glacier. To investigate the effect of numerical errors due to discretization, a second mesh consisting of 10-ice element layers (+ 1 sediment layer) was generated. The vertical node spacing was determined by Equation (5.12), where $a_i \in [0, 0.01, 0.04, 0.09, 0.16, 0.25, 0.36, 0.49, 0.64, 0.81, 1]$. The element dimensions for the surface nodes distribution were kept the same, only vertical resolution was increased, resulting in 2750 elements and 3432 nodes, respectively. Models with coarse and fine mesh were computed for the uniform sliding case, and the results were compared in Figure 5.13. The vectors for fine mesh case have same length and point the same direction as those for coarse mesh in the entire area. The results suggest that the model with the fine mesh has no significant influence on the flow field. Therefore, the first (coarse) mesh has sufficient resolution to reproduce the general flow regime.

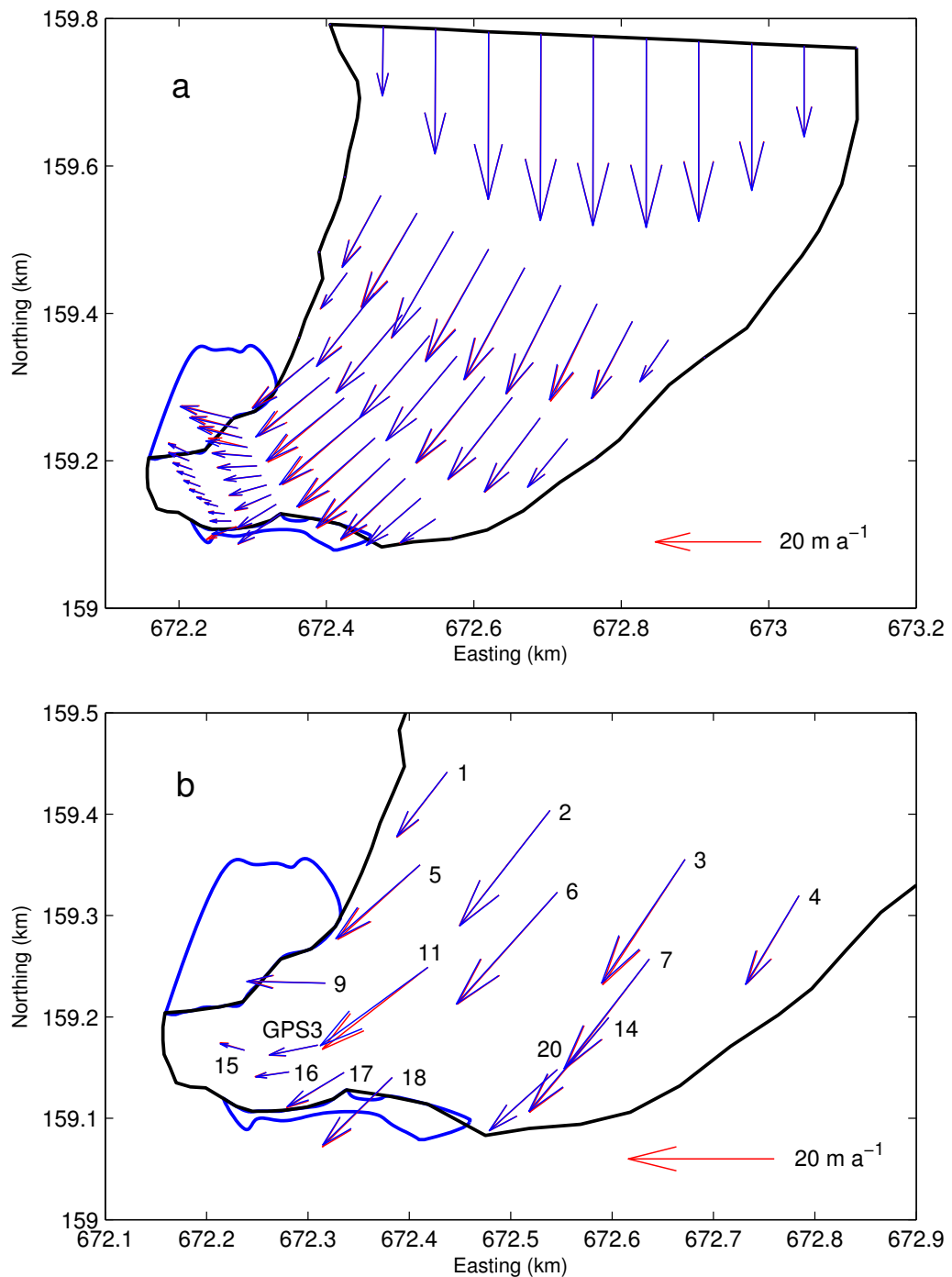


Figure 5.13: Computed surface flow vectors with basal sliding in Test 2. (a) Red vectors indicate computed velocities with the coarse mesh (1500 elements). Blue vectors indicate computed velocities with the fine mesh (2750 elements). (b) Interpolated surface velocities at the locations of GPS measurement in 2009.

5.5 Modeling experiments

In this section, two modeling experiments were carried out to investigate the observed flow field in Rhonegletscher tongue. The first modeling experiments with the applied initial condition are listed in Table 5.2. The lake water pressure load described in Section 5.3.3 was applied with 2211 m a.s.l. of lake level.

5.5.1 Experiment A: Non or uniform sliding

Surface flow velocities were computed with non-sliding condition were computed (Experiment A1). Different values for the sliding coefficient C have been set spatially uniformly over the glacier bed in model runs to find a value of C which best reproduces the observed summer velocities. At first, the model applied for 100 and 200 $\text{m a}^{-1} \text{ MPa}^{-1}$ of C was calculated to compare the flow field under the different basal condition (Experiment A2). The model was then adjusted to the observed summer flow speeds of Stakes 2–4 by tuning C (Experiment A3).

Figure 5.14 shows the results of the experiment without basal sliding ($C = 0 \text{ m a}^{-1} \text{ MPa}^{-1}$), compared to summer flow velocities from 27 June to 6 September in 2009. Despite no-sliding condition is not a realistic condition, the compared flow directions agree well with the observations. General flow direction is reproduced best in the western area of the glacier. The computed flow speeds are less than those observed. In Figure 5.15 the results for different coefficients are compared to the observed summer velocities in 2009.

At the stakes located in the central part of the glacier, there is almost no difference in the direction of surface velocity computed with $C = 100$ and $200 \text{ m a}^{-1} \text{ MPa}^{-1}$. The computed velocities underestimated the observation in the western margin (e.g. Stakes 1 and 5) whereas those at the eastern margin (e.g. Stake 7). In the terminal area, at Stakes 15, 16 and GPS3, computed flow directions are more to the west than the observation.

For our model we prescribed flow velocities as a boundary condition at the upper boundary cross-section (Section 5.3.2). In the work of Gudmundsson (1994), stresses instead of velocities where prescribed as boundary conditions. The adjustment of the calculated velocities to the

Table 5.2: Summary of conducted modeling experiment A.

Experiment	Subject	C ($\text{m a}^{-1} \text{ MPa}^{-1}$)
Experiment A1	Non-basal sliding	0
Experiment A2	Spatially-uniform basal sliding	100 and 200
Experiment A3	Spatially-uniform basal sliding	166

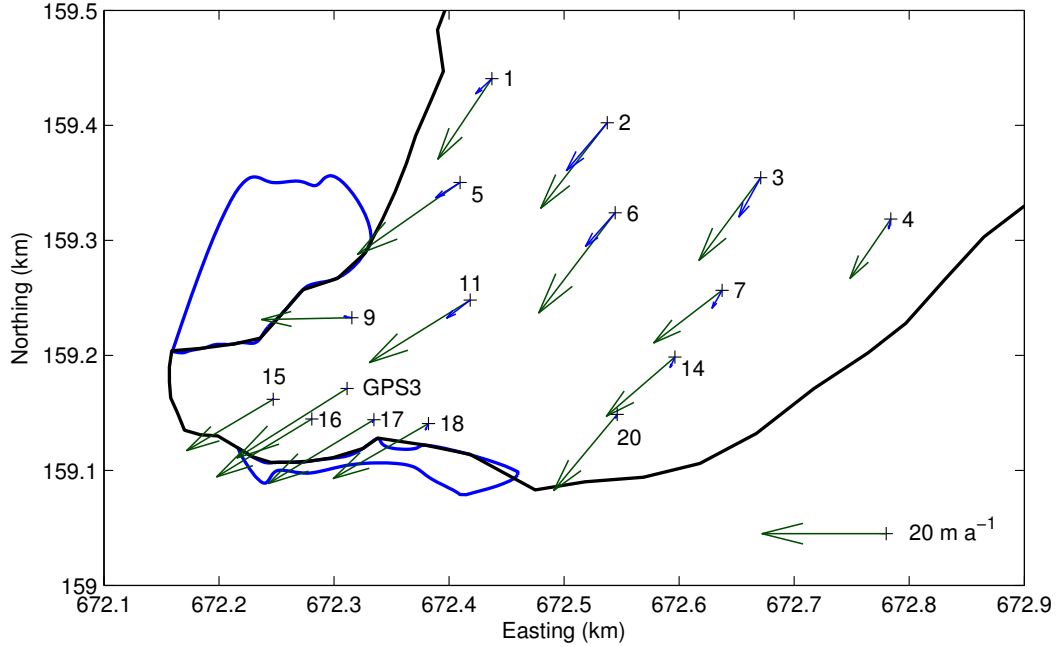


Figure 5.14: Computed flow velocities for $C = 0$ (no-sliding, blue). Green vectors indicate observed summer flow velocities in 2009 (27 June to 6 September).

measured surface velocities was done by adjusting the sliding coefficient C , which defines the viscosity of bottom of the elements in the implemented basal sliding law (Section 5.3.1), uniformly for the entire glacier. In this study, we present a small error analysis in order to quantify the differences between observed and calculated velocities.

The coefficient of determination R^2 is calculated as

$$R^2 \equiv 1 - \frac{\sum_i (u_i^m - u_i^c)^2}{(u_i^m - \bar{u})^2} \quad (5.16)$$

where u_i^m and u_i^c are measured and calculated horizontal flow vectors at Stake i , and \bar{u} is the mean value of measured flow vectors. The error values of R^2 is given for the computed velocity for $C = 166 \text{ m a}^{-1} \text{ MPa}^{-1}$ (Fig. 5.15). According to the error estimate, the best fit of modeled velocity to the observations was achieved with $C = 166 \text{ m a}^{-1} \text{ MPa}^{-1}$, in which $R^2 = 0.965$.

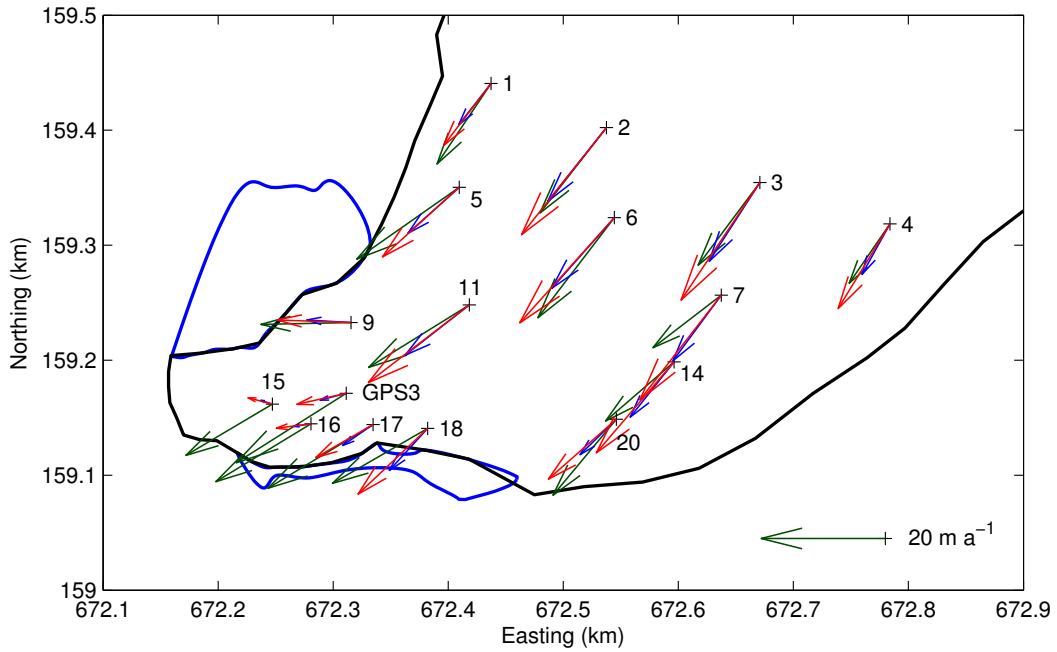


Figure 5.15: Computed flow velocities for different spatially uniform basal sliding coefficients C . Blue and red vectors indicate computed velocities with $C = 100$ and $200 \text{ m a}^{-1} \text{ MPa}^{-1}$, respectively. Green vectors indicate observed summer flow velocities in 2009.

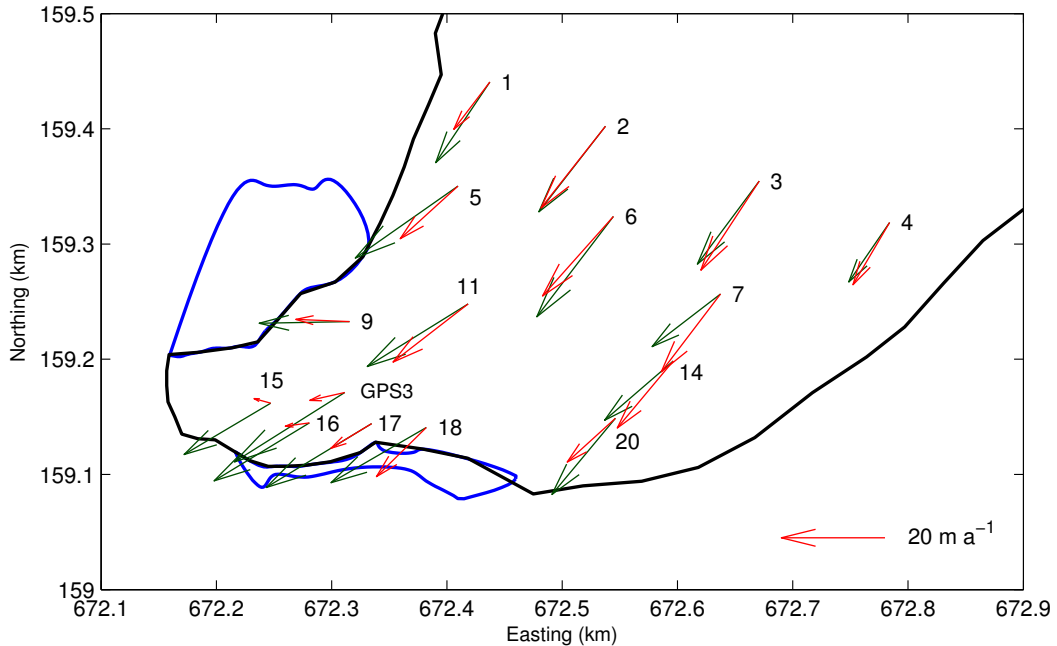


Figure 5.16: Computed flow velocities for uniform sliding ($C = 166 \text{ m a}^{-1} \text{ MPa}^{-1}$). Measured (green) and computed surface velocity (red) are depicted.

5.5.2 Experiment B: Locally enhanced sliding

In experiment B, experiments were repeated with non-uniformly distributed C . Experiment A2 was divided into multiple sub-experiments in which the impact of local changes in C on the surface flow field was investigated at the shore of proglacial lakes.

The glacier bed in the lake shore was introduced larger sliding coefficients C (Fig. 5.16). The initial value of C for entire of the glacier was set to $C = 166 \text{ m a}^{-1} \text{ MPa}^{-1}$. To set the locally enhanced sliding coefficient, we introduced the distribution of effective pressure depicted in Figure 4.5. The sliding coefficient C was increased in two stages. First stage is the area of $P_e < 0$ (red colored area: $C = 18000 \text{ m a}^{-1} \text{ MPa}^{-1}$) and $0 < P_e < 0.05$ (green colored area: $C = 25000 \text{ m a}^{-1} \text{ MPa}^{-1}$), respectively. The resulting model velocities are depicted in Figure 5.17.

The horizontal flow field in the lake area is strongly affected by sliding coefficients (Fig. 5.18a).

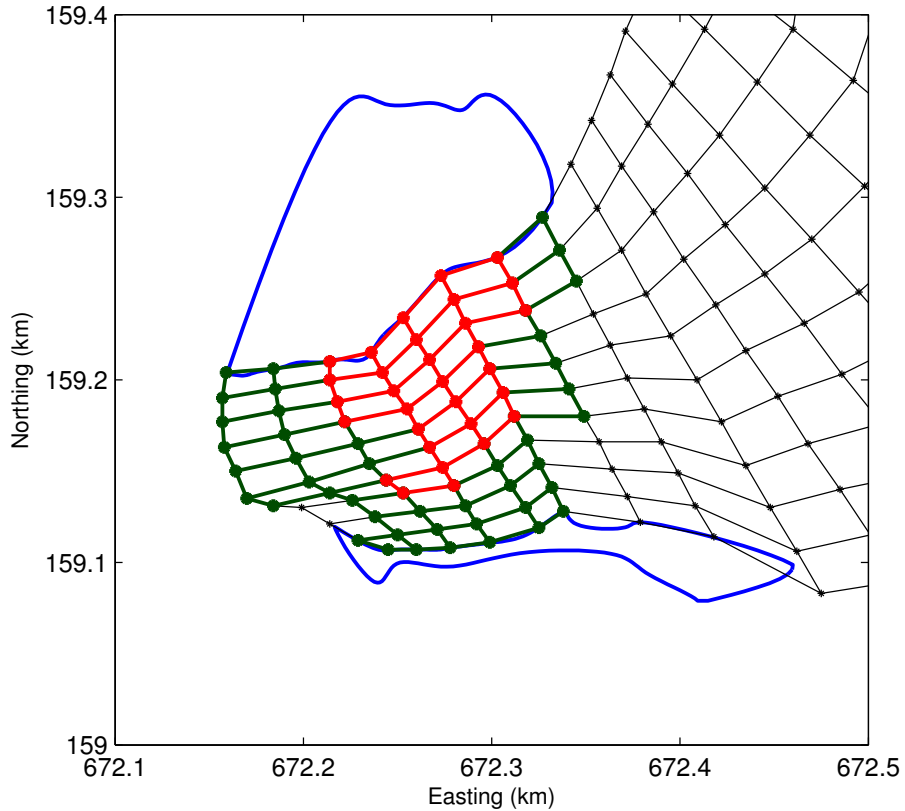


Figure 5.17: Defined sliding area in the shore of lake. Red colored area indicates $P_e < 0$ ($C = 18000 \text{ m a}^{-1} \text{ MPa}^{-1}$). Green colored area indicates $0 < P_e < 0.05$ ($C = 25000 \text{ m a}^{-1} \text{ MPa}^{-1}$).

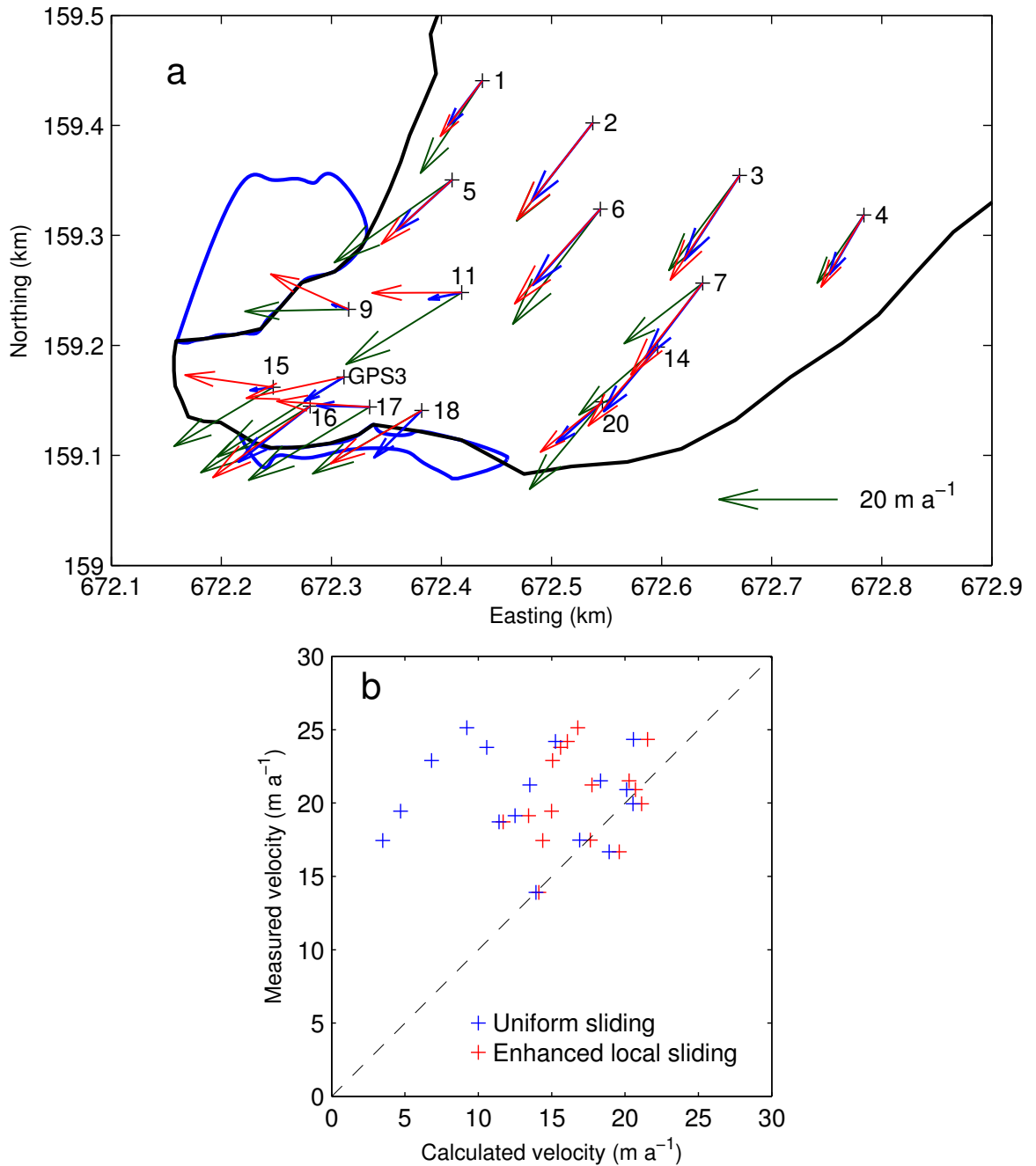


Figure 5.18: The computed flow vectors with locally enhanced basal sliding. (a) Green vectors indicate measured summer flow vectors in 2009. Red is the best fit model flow velocities with spatially uniform constant $C = 166$. Blue is the computed vectors with spatially uniform basal sliding. (b) Scatter plot of measured towards computed velocities with locally enhanced sliding.

In the shore of proglacial lake, the computed flow vectors rotate toward the west with increasing C (e.g. Stakes 9, 11, 15, 18 and GPS3). The effect of glacier acceleration is minor at upper reaches (e.g. Stakes 1–7). The magnitude of computed flow velocities correspond well with measured velocities (Fig. 5.18b). The coefficient of determination R^2 is -1.69 for the computed velocity with locally enhanced sliding and -8.04 for the velocity with uniform sliding.

5.6 Summary

A three-dimensional numerical finite-element model for the tongue of Rhonegletscher has been constructed. The model solves Stokes equations, using Glen’s flow law as constitutive equation. Basal sliding speed was introduced as a linear function of the basal shear stress. Lake water pressure was applied to the elements along the ice-lake boundaries. Boundary conditions on the open transverse section of up-glacier were defined using a two-dimensional cross-section flow model. Velocity distributions on cross-section were derived using surface slope α (9.94°), rate factor A ($75 \text{ MPa}^{-3} \text{ a}^{-1}$) and the basal sliding coefficient C ($97 \text{ m a}^{-1} \text{ MPa}^{-1}$).

Despite no-sliding condition is not a realistic condition, the compared flow directions agree well with the observations. General flow direction is reproduced best in the western area of the glacier. By tuning the linear coefficient of the basal flow law, the model reproduced the observed flow speed at Stakes 2, 3 and 4 with the coefficient of determination of 0.965. However, the computed flow speeds are less than those observed in the lake shore. The horizontal flow field in the lake area is strongly affected by sliding coefficients. In the shore of proglacial lake, the computed flow vectors rotate toward the west with increasing C . The magnitude of computed flow velocities correspond well with measured velocities when C applied the area where $P_e < 0 \text{ MPa}$ ($25000 \text{ m a}^{-1} \text{ MPa}^{-1}$) and $0 < P_e < 0.05 \text{ MPa}$ ($18000 \text{ m a}^{-1} \text{ MPa}^{-1}$). The coefficient of determination R^2 is -1.69 for the computed velocity with locally enhanced sliding.

Chapter 6

Conclusion

6.1 Field observation

Field measurements were carried out in Rhonegletscher, Switzerland during the ablation season of 2007–2009 to investigate the impact of proglacial lake formation on glacier flow. The measurements were conducted with high spatial resolution focusing on temporal and spatial change in horizontal flow velocity, surface vertical displacement (uplift), subglacial water pressure. To conduct subglacial and englacial measurements, the hot water drilling system was developed and used on the glacier.

Annual surface velocities observed at the glacier terminus increased as much as 200% from 2005–06 to 2007–08, though those decreased by 33% at the upglacier (Fig. 4.1). The surface flow velocity of more than 20 m a^{-1} was observed near the terminus, and its magnitude was similar to the velocity in the upper reaches. After the proglacial lake formation, subglacial water pressure exceeded ice overburden pressure in the range of approximately 200 m from the terminus. Thus, most of the flow at the terminus was due to basal ice motion. Decrease in flow velocity observed at upper reaches is due to thinning of ice thickness.

Longitudinal strain at the terminus changed from compression to tensile after the lake formation. In 2009, horizontal strain regime was tensile toward the ice flow direction. Observed extending flow corresponded to thinning rate by $1.2\text{--}2.3 \text{ cm d}^{-1}$, which were 21–41% of the total amount of glacier surface lowering. Accordingly, increase in ice thinning observed in last decade has been caused by both the extending flow regime and negative mass balance.

The huge uplift at the terminus was observed in the shore of both Lake A and Lake B in the late ablation season of 2009. Analysis of the effective pressure confirms that water pressure exceeded the ice overburden pressure in 2008 along the shore of Lake A. The region of excess water pressure extends even farther in the terminal area in 2009 as a result of ice thinning. Associate with the uplift event, a crevasse formed from the shore of lake A toward Lake B. Before the crevasse formed, surface uplift in the shore of Lake A was occurred as a result of a wedge of water would penetrate beneath the ice dam and incrementally jack the ice off its

bed, which is the so-called cantilever effect by Nye (1976). The crevasse has formed due to movement along steeply dipping faults that dip towards the lake and cut through the entire ice thickness. Similar crevasse formation due to this mechanism was observed in previous study in which the crevasse formed in front of the ice-dammed lake during the occurrence of outburst flood.

Significant calving was observed in the late ablation season of 2010. This integrated area corresponded to the calculated effective pressure reach to zero. At the elevation range of 2250–2350 m, the glacier is thinning at a progressively increasing rate. Assuming that the thinning rate of -3.4 m a^{-1} observed in 2008–2009 is sustained, the glacier will retreat approximately 600 m and the lake will expand to its maximum size by 2034. This result is earlier than that reported in previous studies. The possibility of GLOF in Rhonegletscher is not likely as it is dammed by the bedrock bump. However, ice avalanches generate large waves and pose outburst floods after the glacier terminus will retreat up to steep part located upglacier from the western side of lake A.

6.2 Numerical modeling

A three-dimensional numerical finite-element model for the tongue of Rhonegletscher has been constructed. The model solves Stokes equations, using Glen's flow law as constitutive equation. Basal sliding speed was introduced as a linear function of the basal shear stress and lake water pressure was applied to the elements along the ice-lake boundaries. Despite no-sliding condition is not a realistic condition, the compared flow directions agree well with the observations. General flow direction is reproduced best in the western area of the glacier. By tuning the linear coefficient of the basal flow law, the model reproduced the observed flow speed at Stakes 2, 3 and 4 with the coefficient of determination of 0.965. However, the computed flow speeds are less than those observed in the lake shore.

The locally enhanced basal sliding in the lake shore had a great impact on the ice flow regime. The computed flow vectors rotate toward the west with increasing C . The coefficient of determination R^2 is -1.69 for the computed velocity with locally enhanced sliding.

6.3 Future prospects of the study

The glacier flow and subglacial water pressure measurements with high spatial resolution revealed the rapid ice acceleration and surface uplift in the lake area takes place after the proglacial lake formation in 2005. This was the first intensive field measurements to investigate the acceleration in glacier retreat influenced by lake formation. As the next step of the study, it is beneficial to continue similar measurements at the eastern side of the terminus in Rhonegletscher because the glacier evolution is significantly changing due to the acceleration of ice thinning from year to year. Another way in the next step of this study is to carry

6.3. FUTURE PROSPECTS OF THE STUDY

out similar measurements on the other glaciers with similar situation. The comparison of assessment of many glacier evolution with the case in Rhonegletscher can be achieved further comprehension to the interaction of proglacial lake formation and caused dramatic glacier retreat.

According to the results of the presented numerical investigation, the calculated general flow distribution in front of both Lake A and Lake B was relatively to the observed flow field than that at the upper reaches. To achieve more accurate results, it is required to accurate boundary conditions at that area. In particular, it is need to survey a bed topography beneath both Lake A and Lake B and to incorporate these information to the model. The implementation of basal sliding is also crucial to reproduce the general ice flow field of Rhonegletscher by numerical modeling. The process of basal sliding plays a major role in the overall summer flow regime of Rhonegletscher, thus it would be useful to investigate different approaches of describing basal sliding, such as non-linear sliding law (e.g. Raymond and Gudmundsson, 2009) and inverse modeling (e.g. Kaufmann and lambeck, 2002), and their applicability on Rhonegletscher to find a solution which best reproduces the surface flow field of Rhonegletscher.

Bibliography

- Bauder, A., M. Funk and M. Huss. 2007. Ice-volume changes of selected glaciers in the Swiss Alps since the end of the 19th century. *Ann. Glaciol.*, **46**, 145–149.
- Benn, D.I., C.R. Warren and R.H. Mottram. 2007. Calving processes and the dynamics of calving glaciers. *Earth-Science Reviews*, **82**, 143–179.
- Bindschadler, R. 1983. The importance of pressurised subglacial water in separation and sliding at the glacier bed. *J. Glaciol.*, **29**(101), 3–19.
- Bolch, T., M.F. Buchroithner, J. Peters, M. Baessler and S. Bajracharya. 2008. Identification of glacier motion and potentially dangerous glacial lakes in the Mt. Everest region/Nepal using spaceborne imagery. *Nat. Hazard Earth Sys.*, **8**, 1329–1340.
- Boyce, E.S., R.J. Motyka and M. Truffer. 2007. Flotation and retreat of a lake-calving terminus, Mendenhall Glacier, southeast Alaska, USA. *J. Glaciol.*, **53**(181), 211–224.
- Brunner, F.K., R. Coleman and B. Hirsch. 1981. A comparison of computation methods for crustal strains from geodetic measurements. *Tectonophysics*, **71**, 281–298.
- Carlen, W.M. 2005. *The Rhone-Glacier and its ice grotto. Second edition.* Furkapass Switzerland, Touristische betriebe am Rhonegletscher.
- Chen, J. and M. Funk. 1990. Mass balance of Rhonegletscher during 1882/83–1986/87. *J. Glaciol.*, **36**(123), 199–209.
- Clague, J.J. and S.G. Evans. 2000. A review of catastrophic drainage of moraine-dammed lakes in British Columbia. *Quaternary Sci. Rev.*, **36**, 1763–1783.
- Craven, M., I. Allison, R. Brand, A. Elcheikh, J. Hunter, M. Hemer and S. Donoghue. 2004. Initial borehole results from the Amery Ice Shelf hot-water drilling project. *Ann. Glaciol.*, **39**, 531–539.
- Engelhardt, H. and B. Kamb. 1997. Basal hydraulic system of a West Antarctic ice stream: constraints from borehole observations. *J. Glaciol.*, **43**(144), 207–230.

BIBLIOGRAPHY

- Engelhardt, H. and B. Kamb. 1998. Basal sliding of Ice Stream B, West Antarctica. *J. Glaciol.*, **44**(147), 223–230.
- Engelhardt, H., N. Humphrey, B. Kamb and M. Fahnestock. 1990. Physical conditions at the base of a fast moving Antarctic ice stream. *Science*, **248**(4951), 57–59.
- Fischer, U.H. and G.K.C. Clarke. 1994. Ploughing of subglacial sediment. *J. Glaciol.*, **40**(134), 97–106.
- Fischer, U.H. and G.K.C. Clarke. 1997. Clast collision frequency as an indicator of glacier sliding rate. *J. Glaciol.*, **43**(145), 460–466.
- Fountain, A.G. 1994. Borehole water-level variations and implications for the subglacial hydraulics of South Cascade Glacier, Washington State, U.S.A. *J. Glaciol.*, **40**(135), 293–304.
- Fudge, T.J., N.F. Humphrey, J.T. Harper and W.T. Pfeffer. 2008. Diurnal fluctuations in borehole water levels: configuration of the drainage system beneath Bench Glacier, Alaska, USA. *J. Glaciol.*, **54**(185), 297–306.
- Fujii, Y., Y. Ageta, R. Naruse, Y. Ono, H. Hushimi and T. Shiraiwa. 1997. *Hyoga*, Kokon Shoin, Japan, 312pp. (in Japanese)
- Fujita, K., A. Sakai, T. Nuimura, S. Yamaguchi and R.R. Sharma. 2009. Recent changes in Imja Glacial Lake and its damming moraine in the Nepal Himalaya revealed by *in situ* surveys and multi-temporal ASTER imagery. *Environ. Res. Lett.*, **4**, 7pp.
- Funk, M. 1985. Räumliche Verteilung der Massenbilanz auf dem Rhonegletscher und ihre Beziehung zu klimaelementen. Zürcher Geographische Schriften, **24**, ETH Zürich. (in German)
- Funk, M. and H. Röthlisberger. 1989. Forecasting the effects of a planned reservoir which will partially flood the tongue of Unteraargletscher in Switzerland. *Ann. Glaciol.*, **13**, 76–81.
- Gagnon, R.E. and P.H. Gammon. 1995. Characterization and flexural strength of iceberg and glacier ice. *J. Glaciol.*, **41**(137), 103–111.
- Glen, J.W. 1952. Experiments on the deformation of ice. *J. Glaciol.*, **2**, 111–114.
- Glen, J.W. 1955. The creep of polycrystalline ice. *Proc. R. Soc. London Ser. A*, **228**(1175), 519–538.
- Gudmundsson, G.H. 1997. Ice deformation at the confluence of two glaciers investigated with conceptual map-plane and flowline models. *J. Glaciol.*, **43**(145), 537–547.

-
- Gudmundsson, G.H. 1999. A three-dimensional numerical model of the confluence area of Unteraargletscher, Bernese Alps, Switzerland. *J. Glaciol.*, **45**(150), 219–230.
- Gudmundsson, G.H. 2003. Transmission of basal variability to a glacier surface. *J. Geophys. Res.*, **108**(B5).
- Gudmundsson, G.H., A. Iken and M. Funk. 1997. Measurements of ice deformation at the confluence area of Unteraargletscher, Bernese Alps, Switzerland. *J. Glaciol.*, **43**(145), 548–556.
- Haeberli, W. 1983. Frequency and characteristics of glacier floods in the Swiss Alps. *Ann. Glaciol.*, **4**, 85–90.
- Hanson, B., R.L. Hooke and E.M. Grace. 1998. Short-term velocity and water-pressure variations down-glacier from a riegel, Storglaciären, Sweden. *J. Glaciol.*, **44**(147), 359–367.
- Harper, J.T., N.F. Humphrey, W.T. Pfeffer, S.V. Huzurbazar, D.B. Bahr and B.C. Welch. 2001. Spatial variability in the flow of a valley glacier: Deformation of a large array of boreholes. *J. Geophys. Res.*, **106**(B5), 8547–8562.
- Helbing, J. 2006. *Glacier dynamics of Unteraargletscher: verifying theoretical concepts through flow modeling*. Mitteilungen 196, Versuchsanstalt für Wasserbau, Hydrologie und Glaziologie der ETH Zürich, Switzerland, 214pp.
- Hooke, R.L. 2005. *Principles of Glacier Mechanics. Second edition*. Cambridge University Press, 429pp.
- Hooke, R.L., V.A. Pohjola, P. Jansson and J. Kohler. 1992. Intra-seasonal changes in deformation profiles revealed by borehole studies, Storglaciären, Sweden. *J. Glaciol.*, **38**(130), 348–358.
- Hooke, R.L., P. Calla, P. Holmlund, M. Nilsson and A. Steroeven. 1989. A 3 year record of seasonal variations in surface velocity, storglaciären, Sweden. *J. Glaciol.*, **35**(120), 235–247.
- Hubbard, B. and N. Glasser. 2005. *Field Techniques in Glaciology and Glacial Geomorphology*. John Wiley & Sons, Ltd, England, 400pp.
- Huggel, C., A. Kääb, W. Haeberli and B. Krummenacher. 2003. Regional-scale GIS-models for assessment of hazards from glacier outbursts: evaluation and application in the Swiss Alps. *Nat. Hazard Earth. Sys.*, **3**, 647–662.
- Huggel, C., W. Haeberli, A. Kääb, D. Bieri and S. Richardson. 2004. An assessment procedure for glacial hazards in the Swiss Alps. *Can. Geotech. J.*, **41**, 1068–1083.

BIBLIOGRAPHY

- Humphrey, N. and K. Echelmeyer. 1990. Hot-water drilling and bore-hole closure in cold ice. *J. Glaciol.*, **36**(124), 287–298.
- Huss, M., A. Bauder, M. Funk and R. Hock. 2008. Determination of the seasonal mass balance of four Alpine glaciers since 1865. *J. Geophys. Res.*, **113**(F1), F01015.
- Hutter, K. 1983. *Theoretical glaciology; material science of ice and the mechanics of glaciers and ice sheets*. D. Reidel Publishing Company/Tokyo, Terra Scientific Publishing Company.
- Iken, A. 1981. The effect of the subglacial water pressure on the sliding velocity of a glacier in an idealized numerical model. *J. Glaciol.*, **27**(97), 407–421.
- Iken, A. and R. Bindschadler. 1986. Combined measurements of subglacial water pressure and surface velocity of Findelengletscher, Switzerland: conclusions about drainage system and sliding mechanism. *J. Glaciol.*, **32**(110), 101–119.
- Iken, A. and M. Truffer. 1997. The relationship between subglacial water pressure and velocity of Findelengletscher, Switzerland, during its advance and retreat. *J. Glaciol.*, **43**(144), 328–338.
- Iken, A., K. Echelmeyer, W. Harrison and M. Funk. 1993. Mechanisms of fast flow in Jakobshavn Isbræ, West Greenland: Part I. Measurements of temperature and water level in deep boreholes. *J. Glaciol.*, **39**(131), 15–25.
- Jansson, P. 1995. Water pressure and basal sliding on Storglaciären, northern Sweden. *J. Glaciol.*, **41**(138), 415–426.
- Jost, W. 1936. Die seismischen Eisdickenmessungen am Rhonegletscher 1931. *Denkschr. Schweiz. Naturforsch. Ges.*, **71**, 26–42. (in German)
- Jouvet, G., M. Huss, H. Blatter, M. Picasso and J. Rappaz. 2009. Numerical simulation of Rhonegletscher from 1874 to 2100. *J. Comput. Phys.*, **228**, 6426–6439.
- Kamb, B. and H. Engelhardt. 1987. Waves of accelerated motion in a glacier approaching surge: the mini-surges of Varigated Glacier, Alaska, U.S.A. *J. Glaciol.*, **33**(113), 27–46.
- Kaufmann, G. and K. Lambeck. 2002. Glacial isostatic adjustment and the radial viscosity profile from inverse modeling. *J. Geophys. Res.*, **107**(B11), 2280.
- Kirkbride, M.P. and C.R. Warren. 1999. Tasman Glacier, New Zealand: 20th-century thinning and predicted calving retreat. *Global Planet. Change*, **22**, 11–28.
- Koci, B.R. 1984. Hot water drilling in Antarctic firn, and freezing rates in water-filled boreholes. CRREL Spec. Rep. 84, 34, 101–103.

-
- Luckman, A., D. Quincey and S. Bevan. 2007. The potential of satellite radar interferometry and feature tracking for monitoring flow rates of Himalayan glaciers. *Remote Sens. Environ.* **111**, 172–181.
- Lüthi, M., M. Funk, A. Iken, S. Gogineni and M. Truffer, 2002. Mechanisms of fast flow in Jakobshavn Isbræ, West Greenland: Part III. Measurements of ice deformation, temperature and cross-borehole conductivity in boreholes to the bedrock. *J. Glaciol.*, **48**(162), 369–385.
- Meier, M.F. and A. Post. 1987. Fast tidewater glaciers. *J. Geophys. Res.*, **92**(B9), 9051–9058.
- Mercanton, P.L. 1916. Vermessungen am Rhonegletscher, Mensurations au Glacier du Rhône, 1874–1915. *Neue Denkschr. Schweiz. Naturforsch.*, **52**. (in German and French)
- Motyka, R.J., S. O’Neel, C.L. Connor and K.A. Echelmeyer. 2002. Twentieth century thinning of Mendenhall Glacier, Alaska, and its relationship to climate, lake calving, and glacier run-off. *Global Planet. Change*, **35**(1–2), 93–112.
- Müller, B. 2004. Veränderung des Triftgletschers seit 1861: Untersuchung der Stabilitätsveränderung in der Steilstufe. Diplomarbeit, Abteilung für Glaziologie, VAW, ETH Zürich. (in German)
- Naruse, R. and P. Skvarca. 2000. Dynamic features of thinning and retreating Glaciar Upsala, a lacustrine calving glacier in southern Patagonia. *Arct. Antarct. Alp. Res.*, **32**(4), 485–491.
- Nishimura, D. 2008. Changes in surface flow speed over the past 100 years, Rhonegletscher, Swiss Alps. Master thesis, Hokkaido University.
- Nye, J.F. 1952. The mechanics of glacier flow. *J. Glaciol.*, **2**(12), 82–93.
- Nye, J.F. 1953. The flow law of ice from measurements in glacier tunnels, laboratory experiments and the Jungfraufirn borehole experiment. *Proc. R. Soc. London Ser. A*, **219**, 477–489.
- Nye, J.F. 1976. Water flow in glaciers: jökulhlaups, tunnels and veins. *J. Glaciol.*, **17**(76), 181–207.
- Pattyn, F. 2003. A new three-dimensional higher-order thermomechanical ice sheet model: Basic sensitivity, ice stream development, and ice flow across subglacial lakes. *J. Geophys. Res.*, **108**(B8).

BIBLIOGRAPHY

- Purdie, J. and B. Fitzharris. 1999. Processes and rates of ice loss at the terminus of Tasman Glacier, New Zealand. *Global Planet. Change*, **22**, 79–91.
- Quincey, D.J. and N.F. Glasser. 2009. Morphological and ice-dynamical changes on the Tasman Glacier, New Zealand, 1990–2007. *Global Planet. Change*, **68**, 185–197.
- Raymond, C., T.A. Neumann, E. Rignot, K. Echelmeyer, A. Rivera and G. Casassa. 2005. Retreat of Glaciar Tyndall, Patagonia, over the last half-century. *J. Glaciol.*, **51**(173), 239–247.
- Raymond, M.J. and G.H. Gudmundsson. 2005. On the relationship between surface and basal properties on glaciers, ice sheets, and ice streams. *J. Geophys. Res.*, **110**, B08411. (10.1029/2005JB003681.)
- Raymond, M.J. and G.H. Gudmundsson. 2009. Estimating basal properties of glaciers from surface measurements: a non-linear Bayesian inversion approach. *The cryosphere discuss.*, **3**, 181–222.
- Reid, I.A. and W.S.B. Paterson. 1973. Simple method of measuring the average amount of water produced annually by melting of ice on a glacier. *International Association of Scientific Hydrology Publication*, **95**, 215–218.
- Riesen, P. 2007. Investigation of glacier flow during two ice-dammed lake outburst events on Gornergletscher, Valais, Switzerland, by using a three-dimensional numerical model. Diplomarbeit, Abteilung für Glaziologie, VAW, ETH Zürich.
- Riesen, P., S. Sugiyama and M. Funk. 2010. The influence of the presence and drainage of an ice-marginal lake on the flow of Gornergletscher, Switzerland. *J. Glaciol.*, **56**(196), 278–286.
- Riesen, P., T. Strozzi, A. Bauder, A. Wiesmann and M. Funk. 2011. Short-term surface ice motion variations measured with a ground-based portable real aperture radar interferometer. *J. Glaciol.*, **57**(201), 53–60.
- Roberts, M., F. Pálsson, M.T. Gudmundsson, H. Björnsson and F.S. Tweed. 2005. Ice-water interactions during floods from Grænalón glacier-dammed lake, Iceland. *Ann. Glaciol.*, **40**, 133–138.
- Röthlisberger, H. and A. Iken. 1981. Plucking as an effect of water-pressure variations at the glacier bed. *Ann. Glaciol.*, **2**, 57–61.
- Rott, H., M. Stuefer and A. Siegel. 1998. Mass fluxes and dynamics of Moreno Glacier, Southern Patagonia Icefield. *Geophys. Res. Lett.*, **25**(9), 1407–1410.

-
- Salzmann, N., A. Kääb, C. Huggel, B. Allgöwer and W. Haeberli. 2004. Assessment of the hazard potential of ice avalanches using remote sensing and GIS-modelling. *Norsk Geografisk Tidsskrift–Norwegian J. Geography*, **58**, 74–84.
- Skvarca, P., H. De Angelis, R. Naruse, C.R. Warren and M. Aniya. 2002. Calving rates in fresh water: new data from southern Patagonia. *Ann. Glaciol.*, **34**, 379–384.
- Skvarca, P., B. Raup and H. De Angelis. 2003. Recent behaviour of Glaciar Upsala, a fast-flowing calving glacier in Lago Argentino, southern Patagonia. *Ann. Glaciol.*, **36**, 184–188.
- Stroeven, A., R. van de Wal and J. Oerlemans. 1989. Historic front variations of the Rhône Glacier: simulation with an ice flow model. In Oerlemans, J., ed. *Glacier fluctuations and climatic change*. Dordrecht, etc, Kluwer Academic Publishers, 391–405.
- Sugiyama, S. and G.H. Gudmundsson. 2004. Short-term variations in glacier flow controlled by subglacial water pressure at Lauteraargletscher, Bernese Alps, Switzerland. *J. Glaciol.*, **50**(170), 353–362.
- Sugiyama, S., A. Bauder, C. Zahno and M. Funk. 2007. Evolution of Rhonegletscher, Switzerland, over the past 125 years and in the future: application of an improved flowline model. *Ann. Glaciol.*, **46**, 268–274.
- Sugiyama, S., A. Bauder, M. Huss, P. Riesen and M. Funk. 2008b. Triggering and drainage mechanisms of the 2004 glacier-dammed lake outburst in Gornergletscher, Switzerland. *J. Geophys. Res.*, **113**(F4), F04019. (10.1029/2007JF000920)
- Sugiyama, S., T. Yoshizawa, M. Huss, S. Tsutaki and D. Nishimura. 2011. Spatial distribution of surface ablation in the terminus of Rhonegletscher, Switzerland. *Ann. Glaciol.*, **52**(58), 1–8.
- Sugiyama, S., S. Tsutaki, D. Nishimura, H. Blatter, A. Bauder and M. Funk. 2008a. Hot water drilling and glaciological observations at the terminal part of Rhonegletscher, Switzerland in 2007. *Bull. Glaciol. Res.*, **26**, 41–47.
- Taylor, P.L. 1984. A hot water drill for temperate ice. *CRREL Spec. Rep.* **84**, 34, 105–117.
- Tsutaki, S. and S. Sugiyama. 2009. Development of a hot water drilling system for subglacial and englacial measurements. *Bull. Glaciol. Res.*, **27**, 7–14.
- Tsutaki, S., D. Nishimura, T. Yoshizawa and S. Sugiyama. 2011. Changes in glacier dynamics under the influence of proglacial lake formation in Rhonegletscher, Switzerland. *Ann. Glaciol.*, **52**(58), 31–36.

BIBLIOGRAPHY

- Tulaczyk, S., B. Kamb and H.F. Engelhardt. 2001. Estimates of effective stress beneath a modern West Antarctic ice stream from till preconsolidation and void ratio. *Boreas*, **30**, 101–114.
- Turi, G. 2009. The short-term dynamics of the Rhonegletscher tongue. Diplomarbeit, Abteilung für Glaziologie, VAW, ETH Zürich.
- Vaughan, D.G. 1993. Relating the occurrence of crevasses to surface strain rates. *J. Glaciol.*, **39**(132), 255–266.
- Venteris, E.R., I.M. Whillans and C.J. van der Veen. 1997. Effect of extension rate on terminus position, Columbia Glacier, Alaska, U.S.A. *Ann. Glaciol.*, **24**, 49–53.
- Walder, J.S., D.C. Trabant, M. Cunico, S.P. Anderson, R.S. Anderson, A.G. Fountain and A. Malm. 2005. Fault-dominated deformation in an ice dome during annual filling and drainage of a marginal lake. *Ann. Glaciol.*, **40**, 174–178.
- Walder, J.S., D.C. Trabant, M. Cunico, A.G. Fountain, S.P. Anderson, R.S. Anderson and A. Malm. 2006. Local response of a glacier to annual filling and drainage of an ice-marginal lake. *J. Glaciol.*, **52**(178), 440–450.
- Wallinga, J. and R.S.W. van de Wal. 1998. Sensitivity of Rhonegletscher, Switzerland, to climate change: experiments with a one-dimensional flowline model. *J. Glaciol.*, **44**(147), 383–393.
- Warren, C. and M. Aniya. 1999. The caving glaciers of southern South America. *Global Planet. Change*, **22**, 59–77.
- Warren, C.R., D.R. Greene and N.F. Glasser. 1995. Glaciar Upsala, Patagonia: rapid calving retreat in fresh water. *Ann. Glaciol.*, **21**, 311–316.
- Warren, C., D. Benn, V. Winchester and S. Harrison. 2001. Buoyancy-driven lacustrine calving, Glaciar Nef, Chilean Patagonia. *J. Glaciol.*, **47**(156), 135–146.
- Weertman, J. 1957. On the sliding of glaciers. *J. Glaciol.*, **3**, 33–38.
- Yoshizawa, T. 2010. Spatial distribution of surface ablation in the terminus of Rhonegletscher, Switzerland. Master thesis, Hokkaido University. (in Japanese)
- Zahno, C. 2004. Der Rhonegletscher in Raum und Zeit: neue geometrische und klimatische Einsichten. Diplomarbeit, Abteilung für Glaziologie, VAW, ETH Zürich. (in German)

Appendix A

Performance test of the hot water drilling system

To test the performance of the drilling system, its water temperature and flow rate were measured in the Institute of Low Temperature Science from March to April 2007. The drilling performance on Rhonegletscher in 2007 is also indicated.

A.1 Test setting

The test was conducted using hoses with lengths of 1, 50, 100 and 150 m, straight jet nozzles with diameters of 1.6, 2.0, 2.5 and 3.0 mm, and a conic spray nozzle with a diameter of 2.0 mm. The cleaning nozzle provided by the manufacturer was also used to change the flow rate. Because the water jet was very narrow, an accurate measurement of water temperature in the vicinity of the nozzle was difficult (see Fig. 2.4e). The jet was trapped in a 10 l plastic bottle, and the water temperature in the bottle was measured every 15 seconds as it filled using a temperature logger (HIOKI 3633). During the measurement, the temperature setting of the heater was gradually raised from 50 to 135–150 °C. The water flow rate was calculated from the time required to fill a box of 0.02 m³. The consumption rates of petrol and diesel during the experiments were measured as well. The drilling performance of the system was tested by drilling ice blocks of $0.5 \times 0.25 \times 1$ m³ with the 50 m hose, the 2.0 mm straight jet nozzle, and water supplied from the basin.

A.2 Performance test results

Using the 2.0 mm straight nozzle, we measured the water temperature as a function of time for various hose lengths (Fig. A.1a). The maximum temperatures ranged from 64 to 76 °C. The temperature is generally higher for shorter hoses, although the maximum temperature at 150 m length hose exceeds that at 100 m. As the water pressure from a tap is expected to be unstable, the flow rate may have fluctuated in these experiments and influenced the

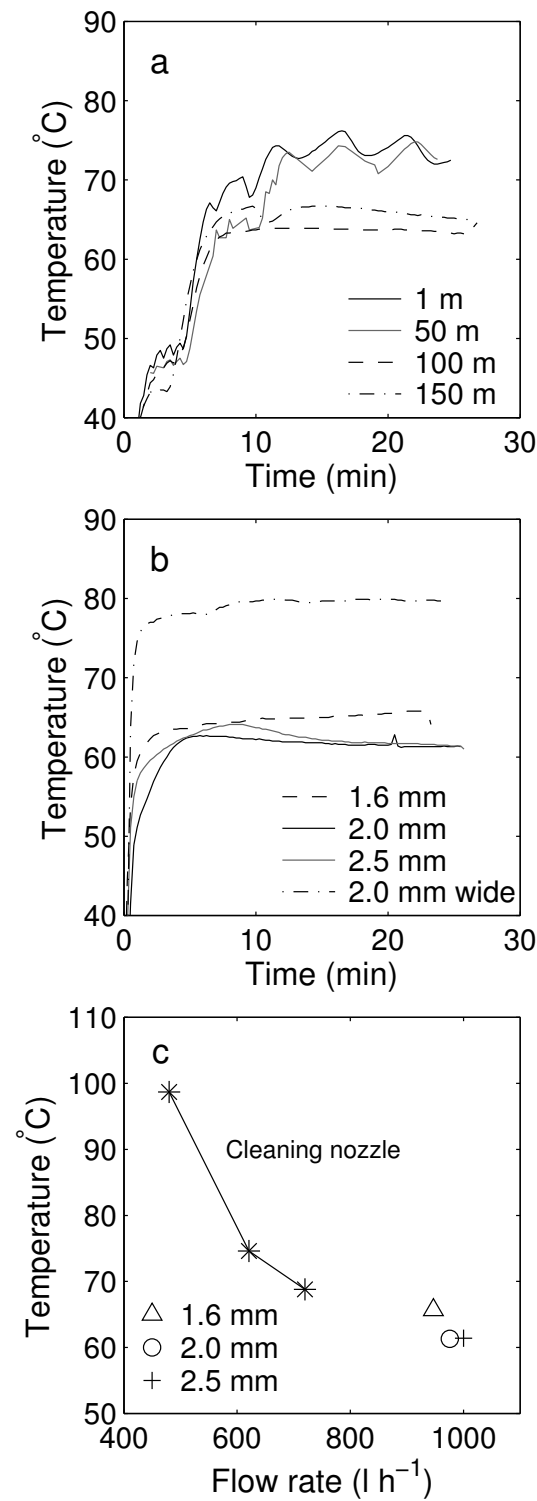


Figure A.1: Water jet temperature vs. time with (a) various hose lengths and (b) various jet nozzle diameters. (c) Flow rates and water jet temperatures obtained with the three jet nozzles and the cleaning nozzle.

water temperature. When we fixed the hose length at 50 m, the maximum temperature for 1.6–2.5 mm nozzles ranged from 60 to 65 °C (Fig. A.1b). The temperature reached 80 °C for the conic spray nozzle, as its flow rate was much lower. These results indicate that the temperature of the water jet is higher than 60 °C and it is slightly influenced by hose length and nozzle diameter. The jet temperature is saturated when the heater setting is above 70 °C because the heater is designed for a flow rate lower than our use.

The relationship between flow rate and temperature was obtained using a 50 m long hose by and the cleaning nozzle (Fig. A.1c). The temperature is very close to the boiling point when the system is operated at 450 l h^{-1} , and decreases as the flow rate increases. For the jet nozzles with diameters of 1.6–2.5 mm, the temperature is about 60 °C and the flow rates are $950\text{--}1000 \text{ l h}^{-1}$. This rate is the upper limit of the pump capacity. With the 3000 l water basin, drilling can be continued for 3 hours at this rate.

The 3.0 mm diameter straight nozzle was not suitable for the system because the pressure dropped below operating range and the heater was automatically shut down by the safety device. In laboratory tests the diesel consumption rate of the heater was 4.7 l h^{-1} , and the petrol consumption rate of the pump was 1.9 l h^{-1} .

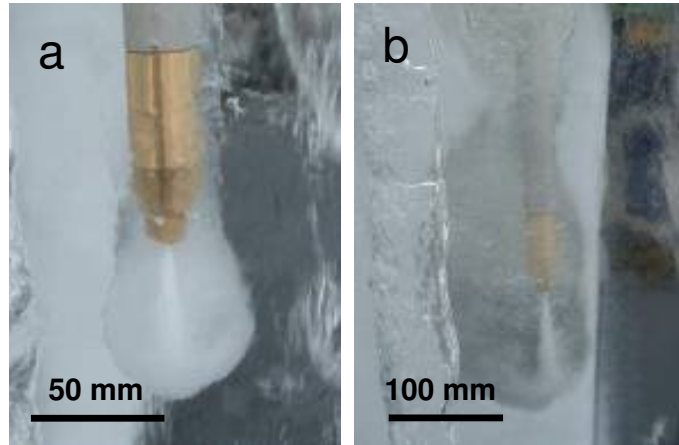


Figure A.2: Drilling nozzle and water jet in the ice block used for the test. The nozzle was lowered quickly in (a), while it was lowered slowly to enlarge the borehole diameter in (b).

A.3 Ice block drilling

Testing the system on an ice block confirmed that the drilling process is very fast. It took about 30 seconds to drill through a 1 m thick ice block, excavating a hole of 50 mm diameter (Fig. A.2a). A wider hole can be drilled by lowering the nozzle more slowly (Fig. A.2b). The times required to drill through 1 m of ice were measured at various temperature settings of the heater (Table A.1). As expected from the abovementioned results (Fig. A.1a, b), the drilling speed is nearly constant when the heater setting temperature is higher than 70 °C.

Table A.1: Time required for drilling through 1 m thick ice blocks and drilling speed. Water temperature was 7.4 °C in the case of no heating.

Heater setting °C	Time sec	Speed m h ⁻¹
no heating	124	29
30	53	68
50	43	84
70	27	133
90	39	92
110	28	129
135	31	116
150	31	116

Drilling is even possible with cold water (7.4°C).

A.4 Borehole drilling in Rhonegletscher

From 13 to 29 July 2007, eight boreholes (BH701–708) were drilled to the glacier bed at positions 300–800 m from the terminus (Fig. A.3). The depths of BH701–708 range from 87–138 m (Table A.2). Figure A.4 plots borehole depth vs. drilling time. The mean drilling rates ranged from $27\text{--}70 \text{ m h}^{-1}$. Hubbard and Glasser (2005) used the same hot water machine at an altitude of 2800 m a.s.l in Haut Glacier d’Arolla, Switzerland. The pump drew water from a 4000 l basin which was filled by melting snow. They obtained drilling rates of 120 m h^{-1} near the ice surface and 30 m h^{-1} at depths greater than 120 m. They reported the water temperature as 80°C . In order to detect the bedrock from a change in hose tension, the drilling rate was deliberately decreased during the last 10–20 minutes. This effect can be observed in the plots for BH701, BH702, BH703, BH706 and BH708. In BH704, BH706 and BH707, the drilling rate decreased when water drained from the borehole. Drilling in an empty borehole is more difficult. This was because the loss of buoyancy force makes the operation of the hose hanging in the borehole more difficult. Other factors may have influenced the drilling rate in some cases, such as the experience of the operator and interruptions due to refuelling or filter cleaning.

Two other relatively important factors are the distance and elevation difference between the hot water machine and the drilling site. Table A.2 shows that BH701 and BH702, located closest to the machine (0 and 95 m), had relatively high drilling rates (50 and 70 m h^{-1}).

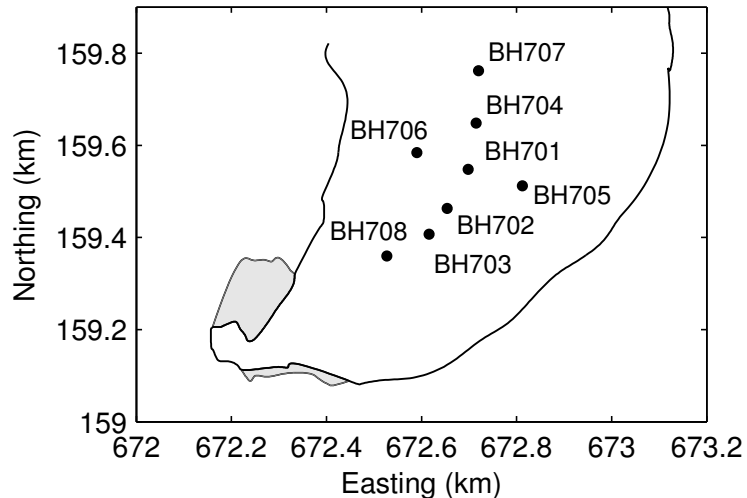


Figure A.3: Map of the borehole locations from 2007 marked (●).

APPENDIX. A

Table A.2: Depth and mean drilling rate of the boreholes in 2007. Horizontal distance and elevation difference between the drilling sites and the hot water machine are also indicated.

Borehole	Borehole depth m	Drilling rate m h^{-1}	Distance m	Elevation m
BH701	138	50	0	0
BH702	120	70	95	-10
BH703	119	49	163	-17
BH704	124	32	103	15
BH705	99	66	121	4
BH706	87	40	113	-2
BH707	135	27	216	35
BH708	103	40	254	-29

BH707 and BH708, situated farther from the machine (216 and 254 m), had rather small drilling rates (27 and 40 m h^{-1}). This relationship is expected because the temperature of the water decreases with distance from the heater. BH704 and BH707, situated at elevations 15 and 35 m higher than the machine, also had smaller drilling rates (32 and 27 m h^{-1}). This effect is probably due to the fact that the flow rate decreases when the pump sends water to higher elevation. During drilling at BH707, the machine often turned itself off because the water pressure dropped below the threshold.

The mean petrol consumption rate was 1.8 l h^{-1} in both 2007 and 2008, which corresponds approximately to the result of our laboratory tests (1.9 l h^{-1}). However, there is a significant difference between the mean diesel consumption rates on the glacier (6.9 l h^{-1}) and in the laboratory (4.7 l h^{-1}). The former rate is also 1.7 times greater than that obtained at Haut Glacier d’Arolla (Hubbard and Glasser, 2005), even though our petrol consumption rate agrees with that experiment within 90%. It is not clear why drilling at Rhonegletscher consumed more diesel than drilling in the laboratory or at Haut Glacier d’Arolla, although both pumps drew cold water from supraglacial stream or melted snow and the drillings conducted at a high altitude. If we take the mean drilling rate observed in BH701–708 (47 m h^{-1}) and the consumption rates measured at Rhonegletscher as benchmarks, our system is able to drill 100 m of ice in a little more than two hours with 14.7 l of diesel and 3.9 l of petrol.

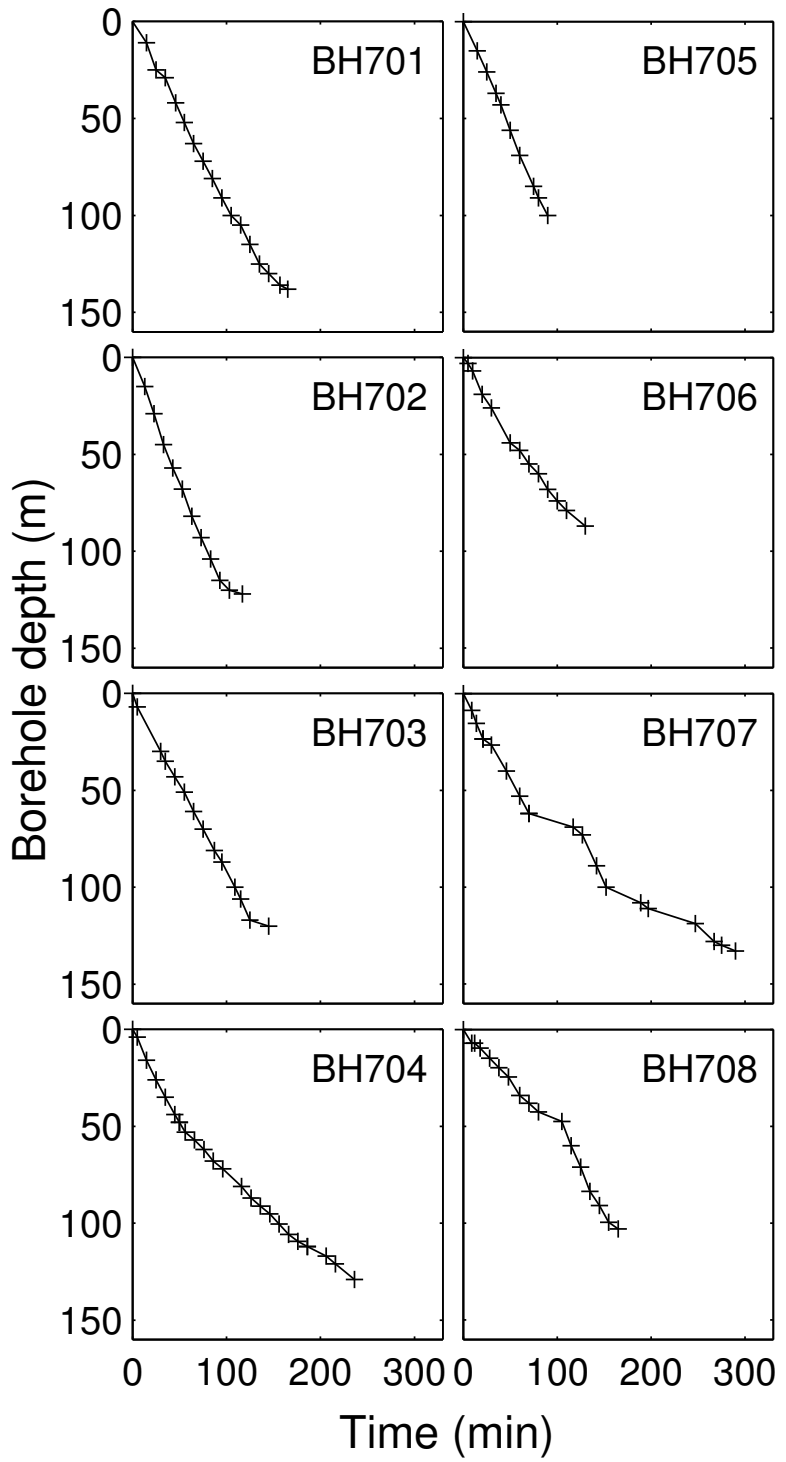


Figure A.4: Drilling depth as a function of drilling time for the boreholes from 2007. The borehole locations are indicated in Figure A.3.

Acknowledgements

The author would like to express his gratitude to Prof. Ralf Greve, Chair of the doctoral degree supervisory committee, for the encouragement he provided to this study. Appreciation goes to Dr. Shin Sugiyama, who supervised the author throughout the doctoral program, supported this research with frequent discussions, and guided the author in the right direction. Prof. Kazuomi Hirakawa, Dr. Takayuki Shiraiwa and Prof. Hiroyuki Enomoto, member of the doctoral degree supervisory committee, encouraged the study and made important comments on the thesis.

Daisuke Nishimura and Takeshi Yoshizawa, member of Glacier and Ice Sheet Research Group in the Institute of Low Temperature Science, Hokkaido University, helped all activities in Zurich and on the glacier. Thanks are also due to Arne Keller, Giuliana Turi and Flavio Lehner. They supported the field work and provided pleasant atmosphere during the field campaign on the glacier.

Prof. Martin Funk, Dr. Andreas Bauder and Thomas Wyder, the Section of Glaciology, Laboratory of Hydraulics, Hydrology and Glaciology (VAW), at the Swiss Federal Institute of Technology (ETH), helped with measurements on the glacier and research work in Zurich. Prof. Heinz Blatter, Institute for Atmospheric and Climate Science, ETH Zurich and Patrick Riesen, member of the Section of Glaciology, VAW, ETH Zurich, supported my life in Zurich and this study with valuable suggestions. Materials for the field campaign were loaned by Section of Glaciology, VAW, ETH Zurich. Glacier Research Group in the Institute of Low Temperature Science, Hokkaido University, was a supportive base for this study: research plans were developed, many ideas acquired, and theories refined through discussions with group members.

We would like to thank Kenta Chubachi of the Institute of Low Temperature Science at Hokkaido University for designing and constructing the drilling stem. Kota Nakamura of Nakamura Service Inc., Kenichi Hirayama of Kärcher Japan Inc. and Satoshi Asai of Martech Inc. provided useful information on the high-pressure hot water machine.

Finally, the author wishes to dedicate this thesis to his most enthusiastic supporters, his parents, sister, brother, Maiko and Ryo for their constant support.

This research was funded by the Japanese Ministry of Education, Science, Sports and Culture

ACKNOWLEDGEMENTS

through a Grant-in-Aid for Young Scientists (Start-up), 18840002, 2006–2007; and by a Grant-in-Aid for Scientific Research C (Capital), 20540418, 2008–2010. Additional funding was provided by an internal program of the Institute of Low Temperature Science, Hokkaido University, by the Inoue Scientific Field Study Foundation, and by the Global COE Program (Establishment of Centre for Integrated Field Environmental Science), MEXT, Japan.